THE UNIVERSITY OF CHICAGO

SEARCH FOR HEAVY METASTABLE PARTICLES DECAYING TO QUARK PAIRS AT CDF

A DISSERTATION SUBMITTED TO
THE FACULTY OF THE DIVISION OF THE PHYSICAL SCIENCES
IN CANDIDACY FOR THE DEGREE OF
DOCTOR OF PHILOSOPHY

DEPARTMENT OF PHYSICS

BY
SHAWN ANDREW KWANG

CHICAGO, ILLINOIS
MARCH 2011

To my family and friends, and to those who supported me through this PhD

TABLE OF CONTENTS

APPENDIX

LIST OF FIGURES

LIST OF TABLES

ABSTRACT

We report on the search for heavy metastable particles that decay into quark pairs with a macroscopic lifetime ($c\tau \sim 1\ cm$) using data taken with the CDF II detector at Fermilab. We use a data driven background approach, where we build probability density functions to model Standard Model secondary vertices from known processes in order to estimate the background contribution from the Standard Model. No statistically significant excess is observed above the background. Limits on the production cross section in a Hidden Valley benchmark phenomenology are set for various Higgs boson masses as well as metastable particle masses and lifetimes.

ACKNOWLEDGMENTS

For a degree as complicated as this one, with a very long time-scale, there are an innumerable people to acknowledge. In addition, the experimental collaboration, CDF, contains hundreds of people, many of whom played a small part in making this possible.

I must start with my advisor, Mel Shochet, who has guided me through this progress for many years, Mel's knowledge of all aspects of high-energy physics is tremendous. I cannot count the number of times I faced an seemingly intractable problem, only to ask Mel about it and receive the solution. With decades of knowledge and experience, Mel can analyze the problem and synthesize a solution, while making it sound so very simple. His guidance made this physics research possible.

I would like to thank Florencia Canelli, who aided in this physics analysis as well.

I would like to thank two of the post-doctoral researchers that helped me when I had all manner of questions: Eric Brubakker and Dan Krop.

CDF is a collaborative effort. Hundreds of people have designed, built, tested, and maintained a multi-story particle detector. Others have written software to reconstruct the detector's signals. The foundation for this research was laid by the work of these individuals, many of whom I never met.

I do want to thank Ben Kilminster and Eric James, as the conveners of the Higgs Discovery Group at CDF, for helping to work out the final issues of this analysis for blessing. And Tom Junk for helping me understand the statistics of experimental discovery.

Many people at CDF have helped me along the way: Chris Neu, Tom Wright, John Freeman and Ray Culbertson, to name a few.

The other members of my dissertation committee, Ed Blucher, Woowon Kang, and Jon Rosner, deserve mention as they, along with Mel, have the final say on whether or not to confer upon me the degree to which this dissertation is being submitted.

The staff members at both the Univ. of Chicago and at CDF both deserve to be acknowledged. Staff members can sometimes be overlooked, but their efforts make sure everything runs smoothly. I am grateful for their contributions.

Finally, I would like to acknowledge my family: my mother and step-father, for supporting me throughout this entire process.

In addition, if I have omitted someone who deserves thanks, it was not because of a lack of gratitude, but simply because there are too many names to list.

CHAPTER 1

INTRODUCTION

Particle physics is the study of the building blocks of the universe. The atomic theory of matter was formalized in 1805 by John Dalton who proposed that matter is formed from identical units called atoms [1], from the Greek for indestructible.

But almost as soon as his theory was widely accepted, physicists began to try to find even more fundamental particles. The discovery by Thomson of the electron in 1897 began this century-long process [2]. Thomson placed electrodes in a vacuum, specifically a Crookes tube. By applying a voltage across the electrodes (which were situated on one end of the tube), cathode rays would be emitted and travel down the tube toward the other end. These rays could be bent by an electric field, so Thomson theorized they were very small negatively charged particles, which were later named electrons [3]. Thus the atom itself is not indestructible or indivisible but made up of constituent components. These electrons were thought to be evenly distributed through the atom, although they were not stationary.

In 1909 Rutherford, Geiger, and Marsden bombarded a gold foil with alpha particles. Expecting the alpha particles to pass through the foil, as the charge in the atoms was expected to be uniformly distributed, some alpha particles scattered with significant deflection [4]. Now the atom was theorized to consist of a small heavy nucleus surrounded by the electrons.

Rutherford's experiment led to the Bohr model of the atom: a heavy nucleus surrounded by electrons where the electrons are in discrete angular momentum orbits around the nucleus [5]. Bohr's model took into account the new developments in quantum mechanics to explain the fixed wavelengths of light which atoms either emitted or absorbed. The electron can only move between fixed energy levels. But the Bohr model for the

structure of the atom was incomplete. It could only explain some, but not all, of the transition lines of Hydrogen. Into this mix, new particles were discovered.

The discovery of the positron had propped open the door that the universe was more complex than originally thought. In 1932 Anderson observed particle tracks in a cloud chamber that had the same mass as the electron, but whose charge was opposite [6]. Four years later, Anderson and Neddermeyer observed a particle with the same charge as the electron, but approximately 207 times heavier [7] [8]. Named the muon, at the time this surprised most physicists, as the muon was not part of the atom at all.

Discoveries of new particles were not the only development in particle physics. In the early half of the twentieth century, physicists developed the formalism of special relativity and quantum mechanics. Special relativity correctly describes highly energetic initial and final states of interactions. In quantum mechanics, energy and momentum conservation can be violated for a short period of time (or space) [9]. This time is inversely proportional to the amount of extra energy appearing in the interaction. These theories helped physicists understand the new phenomena they were observing.

The Standard Model (SM) of particle physics brings together the different theoretical work and observations in particle physics. It has been able to describe known phenomena and also predict the existence and characteristics of new phenomena, e.g., particles whose properties were later measured with great precision. The success of the SM is shown in various experiments. Yet the Standard Model is incomplete in explaining all of the observed phenomenon in particle physics. Firstly the SM does not include gravity, a serious omission since it is one of the four fundamental forces of the universe. Secondly, neutrino oscillation experiments such as Refs. [10] and [11] were not possible in the original version of the SM.

We present an analysis searching for a phenomenon outside of the SM, specifically the decay of heavy metastable particles. Why search for such phenomenon? One answer is

that science is advanced by pushing into the unknown. The Standard Model provides relatively light metastable particles such as B hadrons, Kaons, and Λs. However, there are no high mass particles with long lifetime. Our search is for a particle that originates from the primary interaction vertex, travels for a macroscopic distance ($\sim$ 1 cm) and then decays into quarks. The SM does not provide a description of such a phenomenon. If one does find such decays, it would reinforce that the SM is an incomplete description of the universe and provide clues to the more complete theory. A second answer is because our experimental apparatus, the CDF II detector, has dedicated electronics to trigger on tracks from particles which don't originate from the primary interaction vertex. The Silicon Vertex Tracker (SVT), which is described in more detail in Chapter 3, triggers on displacted tracks produced in $p\overline{p}$ collisions and allows us to search for the signature of our phenomenon more easily.

This study is a signature based search in which we identify the objects and characteristics the event is required to contain, and then compare observations to expectations. The signature for this search is a displaced vertex. The primary proton-antiproton collision results in the annihilation of particles into energy which in turn produces new particles at the expense of this energy. If the product is a heavy metastable particle with a long lifetime, it will decay with some secondary (or displaced) vertex. Its subsequent daughter particles will have originated from this displaced vertex. When these daughters are reconstructed by a particle physics detector, this displaced vertex may be reconstructed as well. Since the SM does not predict such an event, i.e., we expect few such events as background, our expectations are for little or no observation. Any excess observation above the background will indicate the possibility of new phenomenology not described by the SM.

CHAPTER 2

THEORY

2.1 The Standard Model

2.1.1 Introduction

The Standard Model is a theory that describes elementary particles and their interactions through mediating particles. The SM explains three of the fundamental forces of the universe, from weakest to strongest: weak interaction, electromagnetism, and strong interaction. The SM currently does not explain the fourth force, gravity. According to the standard model there exist two categories of particles: fermions which are the elementary particles of matter, and bosons which act as the force carriers between fermions. The type of interactions fermions can participate in are determined by the various charges the particles have. For example electrons carry no color charge so they cannot interact via the strong force, but they do carry electric charge and thus do interact electromagnetically through its force carrier, the photon. Bosons can also hold various charge(s) and thus may interact with other bosons.

Additionally, fermions are half integer spin particles that follow the Pauli principle: in a unique quantum state there can be only one fermion present [9]. They are described statistically by the Fermi-Dirac distribution. Bosons have integer spin and follow the Bose-Einstein statistics. The Pauli principle does not apply to bosons, therefore there is no limit to the number of bosons in a certain quantum state.

Particles also have corresponding anti-particles which share identical properties to their counterpart, while having opposite charges. The fundamental fermions and bosons described by the standard model are shown in Table 2.1. There are 12 fermions which consists of six quarks (up, down, strange, charm, top, and bottom) as well as three charged

leptons (electron, muon, and tau) and three neutrinos (electron neutrino, muon neutrino, and tau neutrino).

Other particles are composites of these elementary fermions. Doublets of quarks (a quark, anti-quark pair) are called mesons and have integer spin, making them bosons. Triplets of quarks compose baryons. The protons and neutrons that make up the ordinary matter of the macroscopic world are baryons.

Fundamental bosons are force carriers. The gluon (g) carries the strong force, the photon (γ) the electromagnetic force, and the W^+, W^- and Z^0 bosons the weak force. These too have various charges; see Table 2.1. One final boson, the Higgs boson, has been postulated but not observed experimentally. This is discussed further in Section 2.1.5.

Both fermions and bosons are represented by quantized fields which are functions of space-time. The charges particles hold and the subsequent interactions they are subject to are the result of the symmetry represented by these fields [13].

In the classical field theory of particle physics, the variation principle is applied on the space-time volume integral of the Lagrange density. The Lagrange density of a free, half-spin, massive particle is

$$L = \bar{\psi}(i\gamma_\mu \partial^\mu - m)\psi, \tag{2.1}$$

where γ^μ are the Dirac-matrices. The variation of the action integral assuming that the field is fixed on the boundaries of the space-time volume in which the action integral is evaluated provides the equation of motion of the field, called the Dirac equation

$$(i\gamma^\mu \partial_\mu - m)\psi = 0. \tag{2.2}$$

If a physical system exhibits symmetry to a local transformation, one which is only dependent on the space-time coordinate, then such a system is defined as gauge invariant.

Noether's theorem states that for each symmetric transformation there exists a conserved quantity. Noether's theorem was first applied in Quantum Electrodynamics (QED), where the photon was derived from a $U(1)$ local gauge transformation. In order to make the Lagrangian symmetric with respect to this local transformation, one must redefine the derivative of the particle field by adding a gauge field in such a way that the derivative preserves the symmetry, defined as the covariant derivative. This covariant derivative defines how the particle field interacts with the gauge field, i.e., the electromagnetic field. A coupling constant, the electric charge, determines the interaction strength between the gauge field and the particles. Thus, according to Noether's theorem, the electric charge is a conserved quantity.

Additional forces in the SM can also be derived in similar fashion. The three forces described in the SM are based on a $SU(3) \times SU(2) \times U(1)$ symmetric group. And the couplings associated to each of these groups can be expressed in terms of:

1. α_S is the strong coupling constant associated with the strong force.
2. G_F is the Fermi constant associated with the weak force.
3. The electric charge, e, is associated with electromagnetic interactions.

2.1.2 Quantum Electrodynamics

Quantum Electrodynamics (QED) is the simplest construction of a quantum field theory. QED was developed by Tomonaga [14], Schwinger [15] [16] and Feynman [17] [18] [19]. It describes how electromagnetic interactions couple fermions to bosons in a relativistially invaraint form. Like QED, the weak and strong forces are also gauge theories. Thus they are more complex generalized forms of QED.

The Lagrangian of a free massive fermion (equation (2.1)) is not invariant under the U(1) local transformation

$$\psi \rightarrow e^{-i\alpha(x)}\psi, \tag{2.3}$$

where the parameter of the transformation $\alpha(x)$ is a function of space-time. When taking the derivative of the transformed field, the partial derivative of $\alpha(x)$ remains. The solution is to transform the derivative as well, i.e., define a covariant derivative

$$D_\mu \equiv \partial_\mu + iqA_\mu, \tag{2.4}$$

where $A_\mu(x)$ also transforms

$$A_\mu \rightarrow A_\mu + \frac{1}{q}\partial_\mu\alpha. \tag{2.5}$$

The vector field A_μ is the gauge field, and in the case of this $U(1)$ symmetry it is the electromagnetic (EM) field. The quantum of the EM field is the photon. It interacts with charged particles and it also has its own dynamics. The Lagrangian of the system of both the fermion and the EM field is completed with the kinetic term of the photon. This is derived from the gauge invariant field strength tensor

$$F_{\mu\nu} = \partial_\mu A_\nu - \partial_\nu A_\mu. \tag{2.6}$$

The Lagrangian is

$$L_{EM} = -\frac{1}{4}F_{\mu\nu}F^{\mu\nu}. \tag{2.7}$$

There is no quadratic term for the vector field in this Lagrangian (e.g., $m^2 A_\mu A^\mu$). This defines the photon as being a massless particle.

2.1.3 Electroweak Theory

The theory of the weak interactions is constructed similar to QED, but the transformations are given by an SU(2) group. The dimension of SU(2) is three, therefore the weak interactions are mediated by three vector bosons following from the constructions of the covariant derivatives. However, the transformations do not allow the vector bosons to have mass. This problem is solved by unifying QED and the weak interaction in the Electroweak theory. Electroweak theory was developed by Glashow [20], Salam, and Weinberg [21].

Fermions (electrons and neutrinos in this example) are governed by the Lagrangian in equation (2.1). The Lagrangian can be written in terms of right-handed and left-handed components of the spinors given by

$$\psi_L = \frac{1-\gamma_5}{2}\psi, \;\; \psi_R = \frac{1+\gamma_5}{2}\psi. \tag{2.8}$$

The left-handed components (an electron and a neutrino) form an isospin doublet $\psi_L = (e_L; \nu_L)$, and the right handed component (an electron) is an isospin singlet $\psi_R = (e_R)$.

The Lagrangian is required to be invariant under the $SU(2)_L$ symmetric transformation, thus the following covariant derivative is introduced

$$\partial_\mu \rightarrow D_\mu = \partial_\mu + ig\frac{\tau_a}{2}W_\mu^a + i\frac{g'}{2}YB_\mu. \tag{2.9}$$

The $W_\mu^a (a = 1, 2, 3)$ gauge fields correspond to the $SU(2)_L$, where the subscript L indicates that the transformation only applies to the left-handed spinors. And B_μ corresponds to the $U(1)_Y$ transformation. g and g' are the coupling constants and τ^a are the Pauli spin-matrices.

Y is the weak hypercharge and is equal to -1 for the left-handed fermion doublet and

-2 for the right-handed fermion singlet. The hypercharge and the weak isospin, T, can be combined to form the electric charge $Q = T_3 + \frac{1}{2}Y$. W_μ^3 interacts only with left-handed fermions ($T_3 = \pm\frac{1}{2}$) and B_μ interacts with both left and right-handed fermions ($T_3 = \pm\frac{1}{2}$ and $T_3 = 0$, respectively).

In these mass eigenstates, W_μ^3 is mixed with B_μ via a rotation which results in the observable EM vector boson A_μ and the neutral weak boson Z_μ. The angle of the rotation is the Weinberg angle, θ_W. The physical fields are

$$W_\mu^\pm = \frac{1}{\sqrt{2}}(W_\mu^1 \mp iW_\mu^2) \tag{2.10}$$

and

$$A_\mu = \cos\ \theta_W B_\mu + \sin\ \theta_W W_\mu^3 \tag{2.11}$$

$$A_\mu = -\sin\ \theta_W B_\mu + \cos\ \theta_W W_\mu^3, \tag{2.12}$$

where

$$\tan\ \theta_W = \frac{g'}{g}. \tag{2.13}$$

Finally, the field tensors are

$$B_{\mu\nu} = \partial_\mu B_\nu - \partial_\nu B_\mu \tag{2.14}$$

$$W_{\mu\nu} = \partial_\mu W_\nu - \partial_\nu W_\mu + gW_\mu \times W_\nu. \tag{2.15}$$

The Electroweak theory predicted the existence of the $W^\pm$ and Z^0 bosons before

their discovery at CERN [22] [23]. However, in the formulation given, these bosons are still massless as a mass term in the Lagrangian (equation (2.7)) would not be invariant under gauge transformations. The solution to this is provided by the mechanism developed by Higgs [24]. The Higgs boson is the last particle in the SM yet to be observed experimentally.

2.1.4 Quantum Chromodynamics

Quantum Chromodynamics (QCD) describes the interactions between quarks and gluons. Two fermions cannot occupy the same quantum-state via the Pauli principle. However, pairs and triplets of quarks form mesons and baryons. This contradiction is resolved by assigning a new charge to quarks, known as color charge [25]. QCD is an $SU(3)$ symmetry that predicts the existence of three color charges and eight bosons that mediate the strong force.

The Lagrangian in QCD is expressed in terms of the quark field $q_j = (q_1, q_2, q_3)$. Since $SU(3)$ operates on three-dimensional vectors, there must be three components to describe the three color states of a quark,

$$L = \bar{q_j}(i\gamma^\mu \partial_\mu - m)q_j. \tag{2.16}$$

The Lagrangian must also be invariant under the local transformation

$$q(x) \rightarrow e^{i\alpha_a(x)T_a}q(x), \tag{2.17}$$

where T_a are eight traceless Gell-Mann matrices that serve as the basis for a 3×3 unitary transformation. Since these matrices do not all commute with each other, this group is non-Abelian. Similarly to QCD, the Lagrangian is not initially invariant under this local transformation. It can be made invariant by introducing the following covariant

derivative.

$$D_\mu \equiv \partial_\mu + igT_a G^a_\mu. \tag{2.18}$$

The result is that eight gauge fields are needed to complete the symmetry which transform as

$$G^a_\mu \to G^a_\mu - \frac{1}{g}\partial_\mu \alpha^a - f^a_{bc}\alpha^b G^c_\mu, \tag{2.19}$$

where the terms in the form f^{abc} are structure constants of the group determining the commutation relations between the elements of the SU(3) transformation group. The eight gauge fields imply the existence of eight gluons. And the field strength tensor is defined as follows:

$$F^a_{\mu\nu} \equiv \partial_\mu G^a_\nu - \partial_\nu G^a_\mu + g f^{abc} G^b{}_\mu G^c_\nu. \tag{2.20}$$

The last term in the above equation did not appear in the formula of the EM field tensor. It is due to the non-zero commutation between the components of the field. However it is still possible to construct an invariant F^a that characterizes the field

$$L = -\frac{1}{4} F^a_{\mu\nu} F^{\mu\nu}_a. \tag{2.21}$$

As mentioned before, because there are three dimensions of the transformation group, there are three color charges associated with each component of the quark field. These are labeled red (R), green (G), and blue (B). Anti-quarks contain anti-color: $\bar{R}$, $\bar{G}$, and $\bar{B}$. When three quarks are bound in a baryon, they must be of different color to satisfy the Pauli principle, thus the "color" of the baryon is white. Similarly, mesons are combinations of a quark and an anti-quark, which must be of opposite color charge, and

thus mesons are also white. Because the transformation group is non-Abelian, there is an additional quadratic term in the vector field that allows gluons to self-interact. Thus gluons carry color charges. The eight gluons are the eight possible traceless combinations of the three color and three anti-color charges.

Because gluons can couple to themselves, one of the consequences of QCD is that gluon-gluon interactions produce an anti-screening effect. In QED, electron-positron pairs present in the vacuum create a screening effect to an electrically charged particle. In QCD a similar effect is called color confinement because the anti-screening effect results in the coupling constant increasing with distance. The result is that there are no stable single quarks and no free gluons.

Because the QCD coupling strength is very large, events observed at the Tevatron collider are mainly produced through QCD interactions. Specifically for this analysis, the heavy flavor quark (b quark) plays a large role. The SM can create b quarks via QCD interactions through a number of different processes: flavor creation, gluon splitting, flavor excitation, pair production, and initial state and final state radiation. For the energy ranges of this analysis, most of the b quarks are produced by either direct production or gluon splitting.

2.1.5 Higgs Mechanism

To understand the Higgs mechanism one must first discuss spontaneous symmetry breaking. Spontaneous symmetry breaking occurs in a system with several likely outcomes, where one specific outcome must occur. Thus while the overall system is symmetric, it is never encountered with this symmetry, instead only manifesting itself in one state.

Mathematically we start with a complex scalar field $\phi = (\phi_1, \phi_2)$ with the following Lagrangian:

$$L = \partial_\mu \phi^* \partial^\mu \phi - V(\phi^* \phi), \tag{2.22}$$

and the potential is

$$V(\phi^* \phi) = \mu^2 (\phi^* \phi) + \lambda (\phi^* \phi)^2, \tag{2.23}$$

and λ is positive so that the potential has a minimum. The Lagrangian (2.22) is invariant under the global U(1) transformation.

$$\phi \rightarrow e^{i\theta} \phi, \tag{2.24}$$

thus ϕ can be expressed with real and imaginary components

$$\phi = \frac{\phi_1 + i\phi_2}{\sqrt{2}}. \tag{2.25}$$

Using this expression for ϕ in the Lagrangian results in

$$L = \frac{1}{2}(\partial_\mu \phi_1 \partial^\mu \phi_1 + \partial_\mu \phi_2 \partial^\mu \phi_2) - V(\phi_1, \phi 2). \tag{2.26}$$

Here two possibilities emerge depending on μ^2. If μ^2 is positive then there is a minimum potential energy when $\phi = 0$. If μ^2 is negative then the minimum energy no longer corresponds to a unique value of ϕ but is instead degenerate with the minimum as a ring in the complex plane,

$$\phi_{V_{min}} = \pm \sqrt{\frac{-\mu^2}{2\lambda}}. \tag{2.27}$$

Now we choose a ground state where $\phi_1 = v$ and $\phi_2 = 0$ and

$$v^2 = \frac{-\mu^2}{\lambda}. \tag{2.28}$$

Define $\phi\prime_1$ and $\phi\prime_2$ as perturbations about this chosen configuration

$$\phi\prime_1 = \phi_1 - v \tag{2.29}$$

$$\phi\prime_2 = \phi_2 \tag{2.30}$$

Plugging these into the Lagrangian (2.26) results in a field $\phi\prime_1$ with mass $\mu = v\sqrt{2\lambda}$ and a Goldstone boson $\phi\prime_2$ with zero mass, plus interaction terms:

$$L = \frac{1}{2}\partial_\mu \phi_1\prime \partial^\mu \phi_1\prime + \lambda v^2 \phi_1\prime^2 + \frac{1}{2}\partial_\mu \phi_2\prime \partial^\mu \phi_2\prime + interact. \tag{2.31}$$

From the above it can be seen how the spontaneous symmetry breaking of the $U(1)$ symmetry caused by the degenerate energy minimum of the Lagrangian (2.26) creates a perturbative theory with a massive scalar boson ($\phi\prime_1$).

Now if we return to Lagrangian (2.26) and replace the derivative with the covariant derivative

$$D_\mu = \partial_\mu + iqA_\mu, \tag{2.32}$$

the Lagrangian now becomes

$$L = D^\mu \phi^* D_\mu \phi - V(\phi) - \frac{1}{4} F_{\mu\nu} F^{\mu\nu}. \tag{2.33}$$

This Lagrangian is invariant under the $U(1)$ gauge transformations

$$\phi(x) \rightarrow \phi\prime(x) = \phi(x)e^{iq\alpha(x)} \tag{2.34}$$

$$A_\mu(x) \rightarrow A_\mu\prime(x) = A_\mu(x)\partial_\mu\alpha(x), \tag{2.35}$$

where $\alpha(x)$ is any differentiable function. Proceeding as before the Lagrangian now becomes

$$L = \frac{1}{2}\partial_\mu\phi\prime_1\partial^\mu\phi\prime_1 + \lambda v^2\phi\prime_1^2 + \frac{1}{2}\partial_\mu\phi_2\prime\partial^\mu\phi^2\prime + interact. \tag{2.36}$$

$$+\frac{1}{4}F_{\mu\nu}F^{\mu\nu} + \frac{q^2v^2}{2}A_\mu A^\mu + qvA_\mu\partial^\mu\phi\prime_2. \tag{2.37}$$

In this Lagrangian the mass of the vector boson A_μ depends on the vacuum expectation value v of the field ϕ. Equation (2.36) still contains a massless scalar field ϕ_2 and an interaction term with A_μ. Fortunately there is one degree of freedom remaining which allows for the choice of a specific gauge

$$\alpha(x) = -\frac{1}{v}\phi_2\prime(x), \tag{2.38}$$

ϕ can be written in as

$$\phi = \frac{1}{\sqrt{2}}(\phi_1\prime + v), \tag{2.39}$$

and (2.36) rewritten as

$$L = \frac{1}{2}\partial_\mu \phi_1\prime \partial^\mu \phi^1\prime + \lambda v^2 \phi_1\prime^2 + \frac{1}{4}F_{\mu\nu}F^{\mu\nu} + \frac{q^2 v^2}{2}A_\mu A^\mu \tag{2.40}$$

$$+\frac{1}{2}q^2(\phi_1\prime + 2v)\phi_1\prime A_\mu A^\mu - \frac{\lambda}{4}\phi\prime_1^3(\phi\prime_1 + 4v). \tag{2.41}$$

Here, the massive scalar field $\phi\prime_1$ is called the Higgs boson with one degree of freedom and a vector boson A_μ with three degrees of freedom.

The Higgs mechanism described above is for a $U(1)$ gauge invariant Lagrangian. To extend it to the $SU(2) \times U(1)$ gauge invariant Lagrangian of the electroweak theory is relatively simple. The starting point is a Lagrangian with a complex scalar doublet

$$\Phi_0 = \frac{1}{\sqrt{2}}\begin{pmatrix} 0 \\ v \end{pmatrix}. \tag{2.42}$$

Here v is chosen as $\sqrt{\frac{-\mu^2}{\lambda}}$. The ground state of this field is chosen so that it breaks the $SU(2)$ and $U(1)_Y$ symmetries but not the $U(1)_{EM}$ symmetry. Thus it must have hypercharge $Y = 1$. The Higgs field is expressed as a perturbation about this vacuum-state. To eliminate the components with zero ground state, we must chose a unitary gauge. The remaining field is

$$\Phi_0 = \frac{1}{\sqrt{2}}\begin{pmatrix} 0 \\ v + h \end{pmatrix}. \tag{2.43}$$

Rewriting the first covariant derivative in (2.22) using the above Higgs field gives

$$(D_\mu \Phi)^\dagger (D_\mu \Phi) = \frac{1}{2}(\partial_\mu h)^2 + \frac{g^2 v^2}{4}\left[\frac{(W_\mu^1)^2 + (W_\mu^2)^2}{2}\right] \tag{2.44}$$

$$+\frac{v^2}{8}(gW_\mu^3 - g\prime B_\mu)^2 + interact. \tag{2.45}$$

Through the Higgs mechanism the Lagrangian is transformed into one real scalar, three massive vector and one massless vector boson. The massless vector boson is the photon. The first term describes the new massive scalar field h, the Higgs particle. Its mass is $v\sqrt{2\lambda}$. The second term gives mass to the $W^\pm$ bosons, the third to the Z^0 boson. There is no term with a quadratic form of A_μ thus the photon is massless.

In effect there are four components of Φ. By choosing proper gauge parameters, three are absorbed by the three weak bosons, giving mass to the $W^\pm$ and the Z^0. The fourth component is the Higgs boson, which has yet to be observed experimentally. Because λ in the above equations is a free parameter, the mass of the Higgs boson cannot be directly calculated from the theory. Searches for the Higgs particle is a currently ongoing field of research in experimental particle physics.

2.2 The Hidden Valley Model

2.2.1 Phenomenology

While the analysis presented here is a search for any heavy particles that decay at a displaced vertex, a phenomenological theory is useful for a benchmark. The Hidden Valley (HV) phenomenology provides a framework in which we can generate signal Monte Carlo (MC) simulation, search for discriminants, optimize our search, and compare results. Here a brief outline of the Hidden Valley phenomenology is presented.

In the Hidden Valley phenomenology, the Standard Model gauge group G_{SM} is ex-

tended by a non-abelian group G_v [26] [27]. SM particles are neutral under G_v, but this new G_v contains light particles that are charged under G_v but neutral under G_{SM}. Heavy SM particles may carry both G_{SM} and G_v charge, which allows for interactions between SM fields and the new light particles. These would appear at the TeV scale at hadron colliders such as the Tevatron.

These v-particles would confine themselves inside v-hadrons, which in effect obey a v-QCD. Since the lightest v-hadrons are heavier than most SM particles, these v-hadrons can decay to SM particles. Figure 2.1 schematically shows a Hidden Valley potential that is "hidden" by an energy barrier. Energetic collisions at the Tevatron create HV particles, some of which can tunnel through the barrier to SM particles. A wide range of masses, lifetimes, and final states exist within the HV framework. However, if the lightest available HV particle, a v-π, equivalent to the SM π, has mass less than that of the top-quark, the predominant decay would be to $b\overline{b}$ quark pairs.

The lifetimes and masses of these v-hadrons are not constrained by the model [28]. With a non-zero lifetime, some particles would travel a distance from the primary vertex before decaying, much like a B or D hadron. This displaced vertex would be a signature to search for.

Applying the HV phenomenology to astroparticle physics, Kaplan, Luty, and Zurek theorize that a HV dark matter candidate could have lifetime on the order of 1 cm [29]. This places the lifetime of the HV particle within the range of lifetimes that can be accessed at the CDF II detector.

A recent analysis from D0 searched for heavy particles decaying with a displaced vertex, in this case into two b quarks [30]. That analysis used the same phenomenological model as our analysis, the Hidden Valley model. However, their search is considerably more restrictive because they trigger on a muon and thus their sensitivity is almost exclusively to a heavy metastable particle that decays to b quarks. Due to the SVT, no such

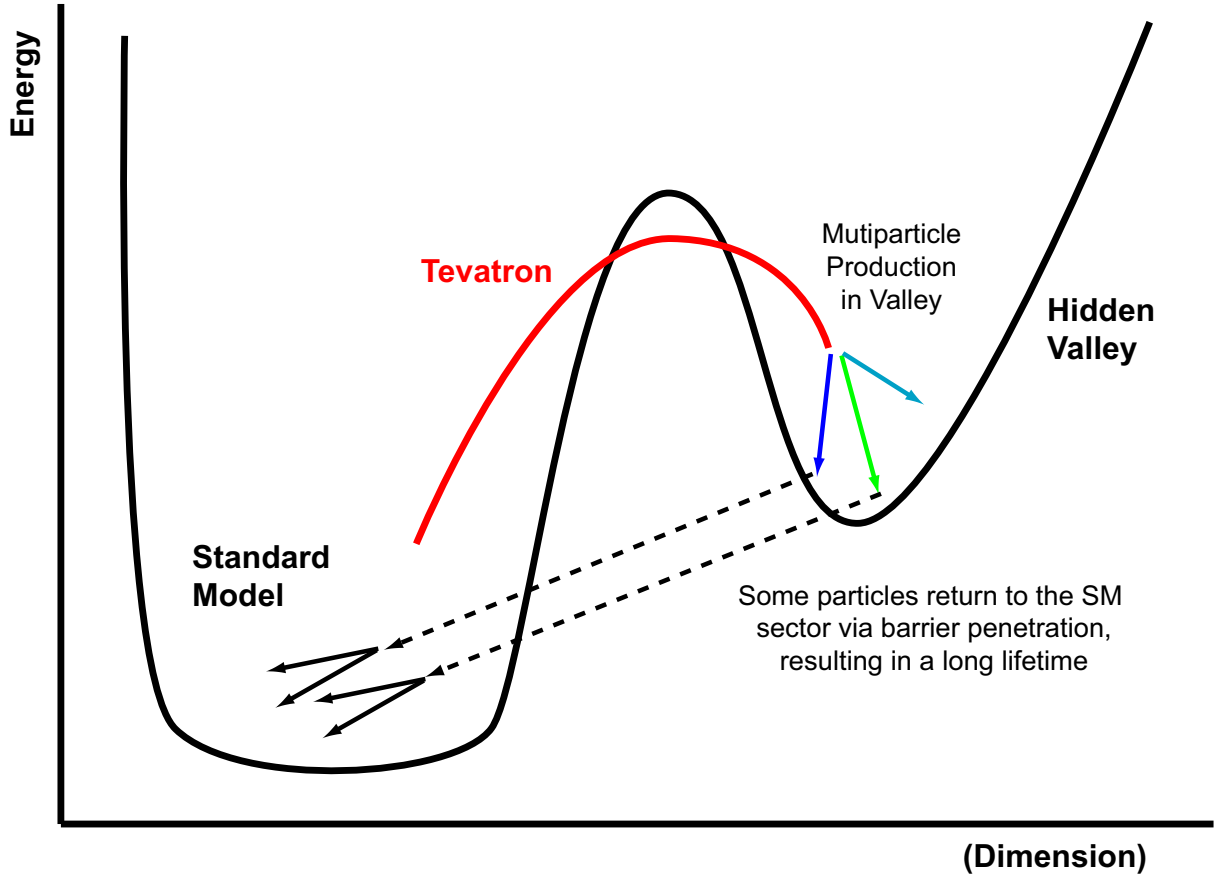

Figure 2.1: A cartoon of the Hidden Valley potential.

limitation is present at CDF.

The HV also provides a way to search for the Higgs boson. If the Higgs mixes with this G_v field then it may decay to two (or more) v-hadrons. These v-hadrons would in turn decay into two $b\overline{b}$ quark pairs. It would be feasible to search for the Higgs boson using this final state at CDF. A Feynman diagram of this decay is shown in Fig. 2.2.

Although we have associated a phenomenological model, the HV model, this search can be applied to any general process containing heavy particles with a long lifetime that decay with a displaced vertex away from the primary vertex. Results presented for this benchmark process can be used to constrain other models by accounting for the differences

in the kinematic properties of the final state.

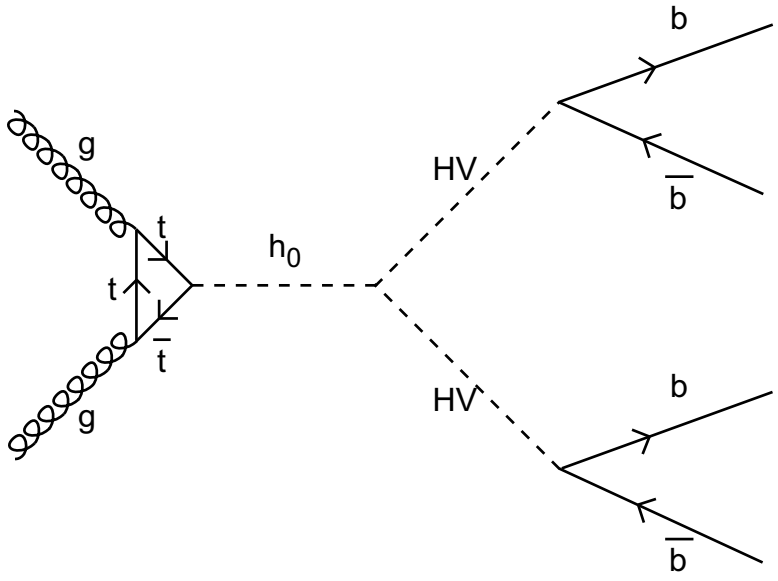

Figure 2.2: Feynman diagram of a basic Hidden Valley decay.

Section 4.2 details the modeling of this phenomenology using Monte Carlo (MC) simulation.

Quarks (spin = $\frac{1}{2}$)		
Particle	Mass ($\mathrm{MeV/c^2}$)	Electric charge (q)
d	$4.1 - 5.8$	$-\frac{1}{3}$
u	$1.7 - 3.3$	$+\frac{2}{3}$
s	$80 - 130$	$-\frac{1}{3}$
c	$1180 - 1340$	$+\frac{2}{3}$
b	$4130 - 4370$	$-\frac{1}{3}$
t	$170400 - 173600$	$+\frac{2}{3}$
Leptons (spin = $\frac{1}{2}$)		
Particle	Mass ($\mathrm{MeV/c^2}$)	Electric charge (q)
e	0.511	-1
ν_e	$< 5 \times 10^{-4}$	0
μ	105.66	-1
ν_μ	< 0.19	0
τ	$1,776.82$	-1
ν_τ	< 18.2	0
Bosons (spin = 1)		
Particle	Mass ($\mathrm{MeV/c^2}$)	Electric charge (q)
g	0	0
γ	0	0
W^+	$80376 - 80422$	$+1$
Z^0	$91166 - 91208$	0
H^0 §	> 114400	0

Table 2.1: Table of Standard Model particles [12]. Antiparticles are the charge conjugates of a particle with the same mass. However, it is not currently known whether or not neutrinos are their own antiparticles. In additional to electric charge, particles also have a hypercharge (Y). Quarks and gluons also have color charge.
§ The Higgs boson has yet to be observed experimentally.

CHAPTER 3

THE TEVATRON AND CDF

Fermi National Accelerator Laboratory (FNAL), or Fermilab, is the home to the Tevatron Accelerator. The Collider Detector at Fermilab (CDF) is used to collect data for this analysis. Both the accelerator and the detector are described below.

3.1 The Tevatron

3.1.1 Description of the Accelerator

The Tevatron is a proton (p) antiproton ($\overline{p}$) particle accelerator which collides these particles with a center of mass energy ($\sqrt{s}$) of 1.96 TeV [31]. In fact there are a series of accelerators that are used to raise the particles to such high energy. A schematic of the accelerator layout is shown in Fig. 3.1.

At the very beginning there is a proton source, namely a bottle of Hydrogen gas. An electron is added to each Hydrogen atom and these H^- ions are accelerated using a Cockcroft-Walton accelerator to 750 keV via an electrostatic potential. The next stage is a linear accelerator, the Linac, which accelerates these protons to 400 MeV through the use of 9 Radio Frequency (RF) cavities. The electrons are stripped off using a carbon foil. The resulting protons are then fed into a circular synchrotron with more RF cavities named the Booster which accelerates these protons to 8 GeV.

The 8 GeV protons are fed into the Main Injector, a second circular accelerator. These protons are accelerated to either 120 GeV or 150 GeV, depending on its final application. It is at this point that some of the 120 GeV protons are diverted to create antiprotons. (Other 120 GeV protons are diverted to NuMi or other experiments at Fermilab.)

Antiprotons are created at Fermilab by bombarding a Nickel target with 120 GeV

protons from the Main Injector. Lithium lenses focus the negative particles which are created in this interaction. The antiprotons are sorted out through the use of a magnetic field, sending the antiprotons to the Debuncher. The Debuncher cools the antiprotons reducing their transverse momentum spread, i.e., the momentum in the 2-dimensional plane orthogonal to the direction of movement. The antiprotons are first stored in a storage ring, named the Accumulator. Antiprotons are created with an efficiency of around 15 to 25×10^{-6} $\overline{p}$ per p. The stacking of antiprotons in the Accumulator however grows in difficulty as the number of antiprotons increase. In addition, the transverse momentum of the antiprotons increases with the size of the "stack." Thus the small antiprotons stacks are transfered to the Recycler every few hours.

The Recycler is an 8 GeV storage ring which shares the same tunnel as the Main Injector. The antiprotons are stored in the Recycler and electron cooling, where the antiproton beam exchanges energy with 4.3 MeV electrons, reduces the beam's transverse momentum. These antiprotons are also accelerated to 150 GeV before being injected into the Tevatron.

The 150 GeV protons and antiprotons are now injected into the Tevatron. This is a 6.3 km circular accelerator with superconducting dipole and quadrupole magnets. Liquid helium is used to cool the magnets to 4 K in order to reach a magnetic field strength of 4.2 T. 36 bunches of protons and antiprotons circulate in the same beampipe in helical orbits. There are 3 trains of 12 bunches, each with 396 ns of separation. When all the protons and antiprotons have been injected into the accelerator, the accelerator ramps the energy of each beam to 980 GeV, thus two colliding beams have center of mass energy of $\sqrt{s} = 1.96$ TeV [32]. Final focusing magnets are used to collide the beams at two interactions points along the accelerator: one at B0, which houses CDF, the other at D0 where the D0 detector resides.

Since the Tevatron stores 36 bunches of protons and antiprotons, a "store" is one

continuous series of collisions using the same set of bunches. As the accelerator loses particles, the luminosity of the beam decreases, until the store is ended (or dropped). Typical stores may last between 12 and 24 hours. While collisions are ongoing, the antiprotons are being accumulated for the next store. Routine turn-around time between stores is around 2.5 hours.

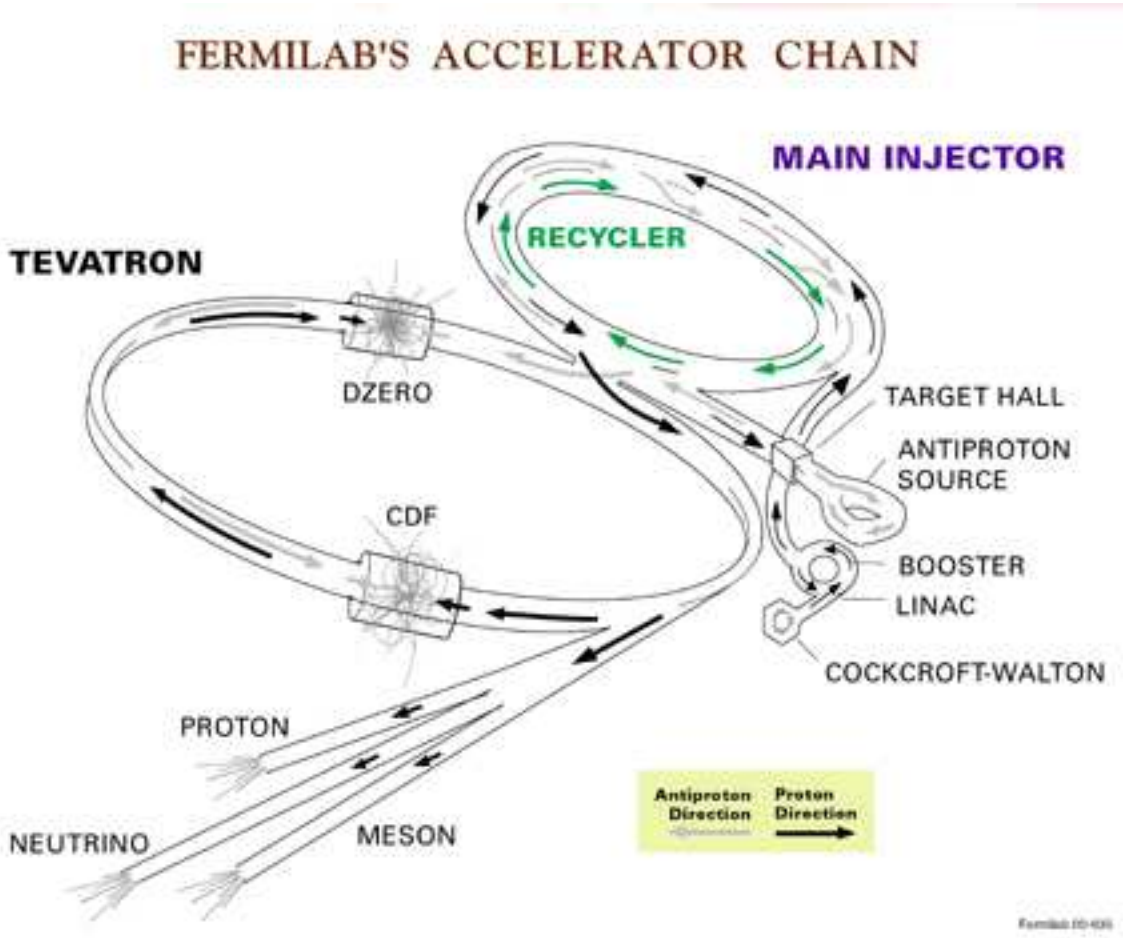

Figure 3.1: The accelerator chain, showing the various accelerators at Fermilab.

3.1.2 Luminosity

The rate of collisions at the Tevatron is quantized by the instantaneous luminosity. Luminosity is characterized by the following equation:

$$L = \frac{f_r N_B N_p N_{\bar{p}}}{2\pi(\sigma_p^2 + \sigma_{\bar{p}}^2)} * F\left(\frac{\sigma_l}{\beta^*}\right), \tag{3.1}$$

and is expressed in units of $\mathrm{cm}^{-2}\ \mathrm{s}^{-1}$.

The terms are defined as follows: f_r is the revolution frequency, N_B is the number of bunches in the machine, N_p and $N_{\bar{p}}$ is the number of protons and antiprotons per bunch. σ_p and $\sigma_{\bar{p}}$ are the width of the beams at the interaction point. F is a function which depends on two variables: σ_l is the ratio of the bunch length divided by the beta function, β^*, at the interaction point.

The luminosity is not a constant in time. The initial luminosity at the beginning of each store is the peak of the distribution. Afterwards it falls off with an exponential function. This is due to both the reduction of the number of particles in the beam, and the fact that the beam loses focus over time. Over the years of Tevatron operation, the initial luminosity has grown, to the point where the average initial luminosity is over $300 \times 10^{30}\ \mathrm{cm}^{-2}\ \mathrm{s}^{-1}$.

The integrated luminosity is the total amount of luminosity collected for a period of time. The integrated luminosity, $\int L\ dt$, is measured in units of inverse barns (b^{-1}) where an inverse barn is defined as $10^{24}\ \mathrm{cm}^{-2}$. The total integrated luminosity delivered by the accelerator for the data used in this analysis is shown in Fig. 3.2. The amount that is actually collected by CDF is shown as well. The efficiency of data-taking at CDF determines how much data delivered is collected. The actual luminosity measurement is detailed in 3.2.5.

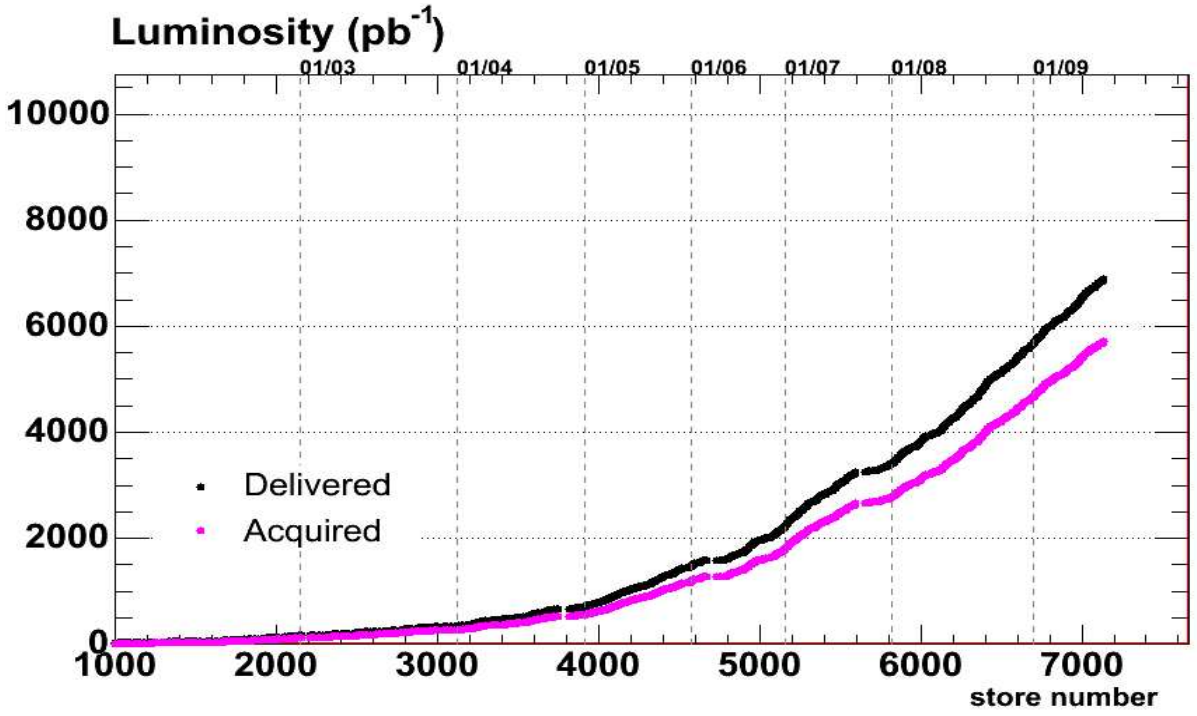

Figure 3.2: The integrated luminosity both delivered and stored to tape for the data used in this analysis.

3.2 Collider Detector at Fermilab

3.2.1 Introduction

The CDF II detector is a general-purpose particle detector with azimuthal and forward-backward symmetry [33] [34]. Positions and angles are expressed in a cylindrical coordinate system (r, ϕ, z), with the z axis along the proton beam, positive z is along the direction the protons travel. The azimuthal angle ϕ around the beam axis is defined with respect to a horizontal ray running outwards from the center of the Tevatron, and radii are measured with respect to the beam axis. The polar angle θ is defined with respect to the proton beam direction, and the pseudorapidity eta is defined to be $\eta = -ln[\tan(\theta/2)]$. The transverse energy and momentum of a particle are defined as $E_T = E \sin(\theta)$ and

$p_T = p \sin(\theta)$, respectively.

The CDF II detector consists of a series of sub-detectors and a multi-lever trigger system. The sub-detectors, from inside to out, consist of a silicon strip tracking system, a wire tracking chamber, both of which are embedded in a superconducting solenoid magnet. Next are an electromagnetic and hadronic calorimeter, and a series of wire chambers and scintillators for the identification of muons. A series of luminosity counters are present in the forward region of the detector. Figure 3.3 shows a cutaway isometric view of the CDF II detector. The detector components and the electronic trigger system are described in detail below.

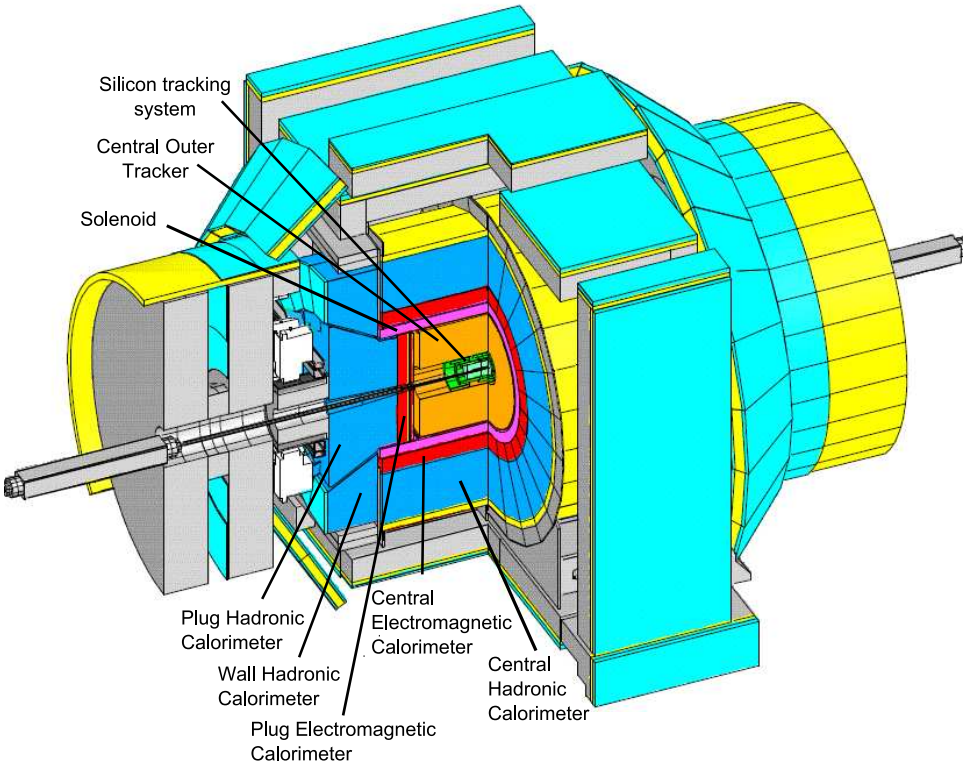

Figure 3.3: Isometric view of the CDF II detector

3.2.2 Tracking

The innermost component of the CDF II detector is the integrated tracking system, composed of three silicon detectors, an open-cell wire chamber, and a superconducting solenoid magnet. The tracking system is used to reconstruct the trajectories (or tracks) of charged particles and precisely measure their curvature in the magnetic field. The curvature coveys the particle's three-momentum. These tracks are instrumental in reconstructing both the primary vertex, where the $p\overline{p}$ interaction occurs, as well as reconstructing secondary vertices, which will be discuss in detail in Section 4.4.

The CDF II silicon tracking system consists of three subdetectors: a single-sided layer of silicon microstrip detectors, immediately located outside the beam pipe (Layer 00), $r = 1.2$ cm. Layer 00's purpose is to improve the tracking resolution, especially the impact parameter of tracks [35]. Next are the five layers of the Silicon Vertex Detector (SVXII) system. These are double-sided silicon microstrips, covering the region from radius 2.45 cm to 10.6 cm [36]. Layers 1, 3, and 5 have one layer of microstrips rotated 90 degrees to provide z-axis information, while layers 2 and 4 have one layer of microstrips set at a small stereo angle. This configuration gives the detector the ability to measure the track's momentum in three dimensions. The silicon detectors are segmented into three barrels along the z-axis; the total length is 96 cm. From radius 19 cm to 29 cm the Intermediate Silicon Layers (ISL) provide coverage out to $|\eta| < 2.0$ in one or two layers depending on η [37]. The impact parameter resolution of the silicon tracking system is 40 μm and the z_0 resolution is 30 μm. One of primary purpose of the silicon detector system is to measure the tracks that arise from the displaced decay of b and c hadrons. Figure 3.4 shows all three silicon detector components.

The Central Outer Tracker (COT) is the main tracking chamber of the CDF II detector. It covers a radius of 40 cm to 137 cm and provides coverage out to $|\eta| \leq 1.0$. It is a

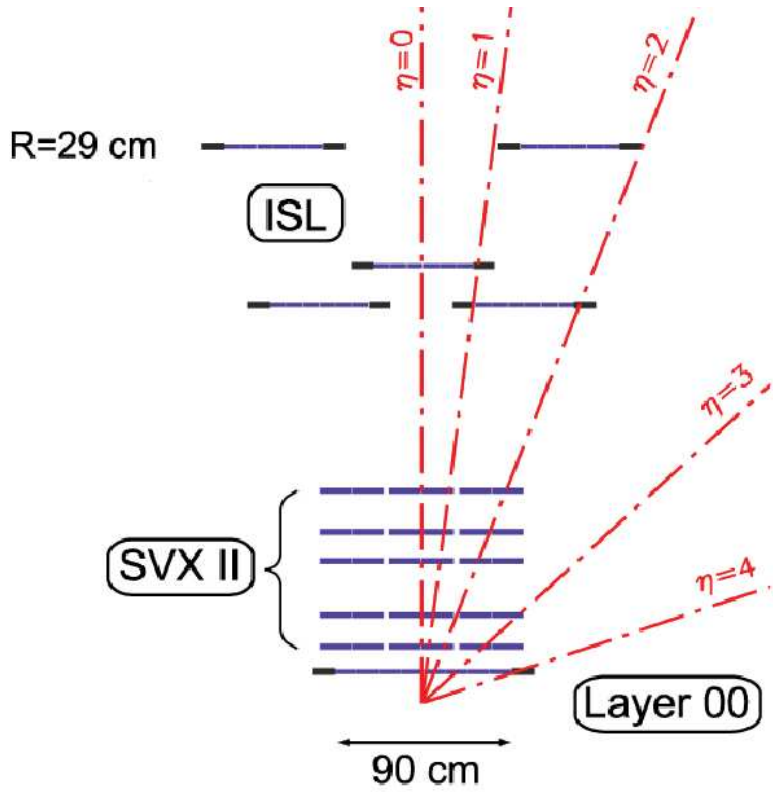

Figure 3.4: Components of the silicon detectors viewed longitudinally to the beamline.

3.1 m long open-cell drift chamber segmented into concentric super layers (SL) . The drift chamber is filled with a mixture of argon and ethane gas. The sense wires are arranged in eight alternating axial and $\pm 2^\circ$ stereo superlayers with twelve layers of wire in each. The momentum resolution of the COT is $\sigma(p_T)/p_T^2 = 0.0015(\mathrm{GeV}/c)^{-1}$ [38].

The tracking systems are located within a superconducting solenoid of diameter 3 m. The solenoid generates a 1.4 T magnetic field parallel to the beam axis. Charged particles bend through this field and leave tracks which are used to measure the particle momentum transverse to the beamline.

3.2.3 Calorimeters

Outside the solenoid, electromagnetic and hadron calorimeters measure the energy of interacting particles. Both calorimeters are sampling calorimeters with scintillators sandwiched between layers of high-Z material. The electromagnetic calorimeter uses lead as the absorber and the hadronic calorimeter uses steel. Both calorimeters are segmented into projective towers covering a range in both pseudorapidity (η) and azimuthal angle (ϕ). The light from the scintillator plates is read out through wavelength-shifting (WLS) light guides by photo-multiplier tubes (PMT). The total energy resolution of the measurement $(\frac{\sigma}{E})^2 = (\frac{\sigma_1}{\sqrt{E}})^2 + (\sigma_2)^2$ depends on statistical sampling fluctuations and the photostatistics of the PMTs which are inversely proportional to the square root of the incident energy, and a constant term due to non-uniform response of the calorimeter, calibration errors, and noise in the electronics.

The central region $|\eta| < 1.1$ is covered by the Central ElectroMagnetic calorimeter (CEM) and the Central HAdron Calorimeter (CHA) and endWall HAdronic Calorimeter (WHA). The forward region $1.1 < |\eta| < 3.6$ is covered by the end-Plug ElectroMagnetic calorimeter (PEM) and the end-Plug HAdron calorimeter (PHA). See Fig. 3.5 for an elevation view of the CDF detector, where the calorimeter components are labeled.

The CEM has a depth of 18 radiation lengths while the CHA has 4.7 interaction lengths. The central calorimeter towers are all segmented with $\Delta\phi \times \Delta\eta$ of $15^\circ \times 0.11$. The coverage of the CEM is $|\eta| < 1.1$ while the CHA and WHA cover $|\eta| < 0.9$ and $0.9 < |\eta| < 1.3$, respectively. It should be noted that the calorimeters are split into two halves (east and west) along the z-direction at $\eta = 0$. The CEM is made of alternating layers of 0.5 cm plastic scintillator and 0.32 cm thick lead absorbers. The relative energy resolution is $(13.5\%/\sqrt{E} \oplus 2\%)$ for a single electron or photon [39]. The CHA and WHA calorimeters use 1 cm thick scintillator layers sandwiched between 2.5 cm and 5 cm thick

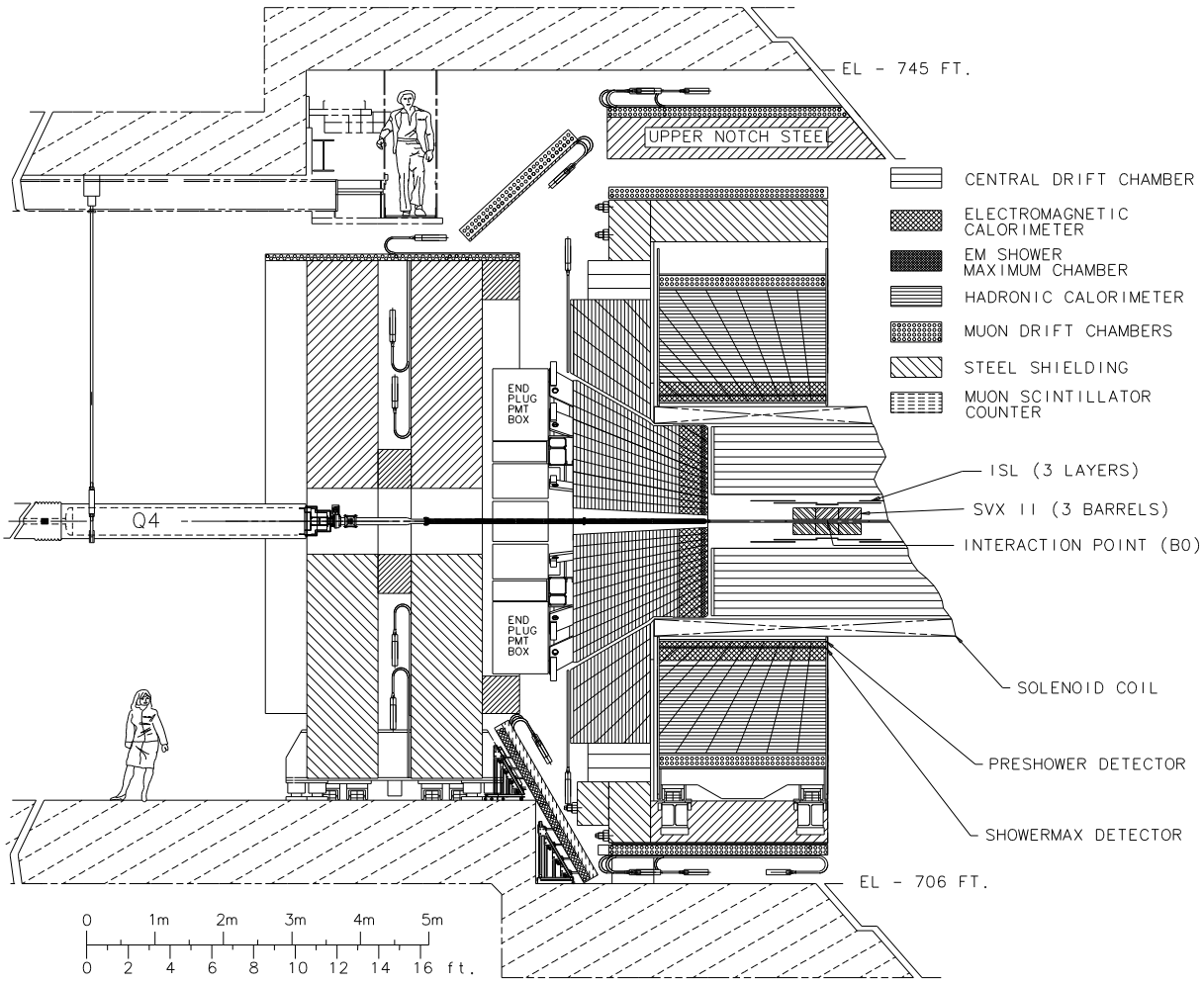

Figure 3.5: Elevation view of the CDF II detector.

steel layers [40]. Their energy resolution is $(75\%/\sqrt{E} \oplus 3\%)$.

The PEM and PHA detectors cover the range $1.1 < |\eta| < 3.6$. The tower segmentation is a factor of 2 finer in the ϕ direction ($7.5°$) for $|\eta| < 2.11$. The η segmentation is the same as the central calorimeters. The PEM has a depth of 21 radiation lengths while the PHA has 7 interaction lengths. The scintillator in the PEM is 0.4 cm thick and the lead tiles are 0.45 cm thick [41]. Their energy resolutions are $(16\%/\sqrt{E} \oplus 1\%)$ and $(80\%/\sqrt{E} \oplus 5\%)$, respectively.

Both the CEM and PEM contain a Shower Maximum detector (ShowerMax or CES),

a thin detector located approximately six radiation lengths into the electromagnetic calorimeter, near the peak of the average electromagnetic shower. The ShowerMax detector consists of wire chambers for additional axial position measurements and cathode strips for additional stereo measurement. The fine segmentation of the ShowerMax detector allows for precise measurement of the shape of electromagnetic showers [42].

The CDF calorimeters measure the energy deposited by both charged and neutral particles produced in the $p\overline{p}$ collision by absorbing their energy. This information along with the tracking information is used in particle identification. In addition, weakly interacting particles such as neutrinos can be reconstructed by computing the imbalance in the total energy transverse to the beamline, called the missing E_T or $\not\!\!E_T$. Different particles create different showers in the calorimeters (as well as interact differently in the tracking chambers and the muon systems) as shown in Fig. 3.6.

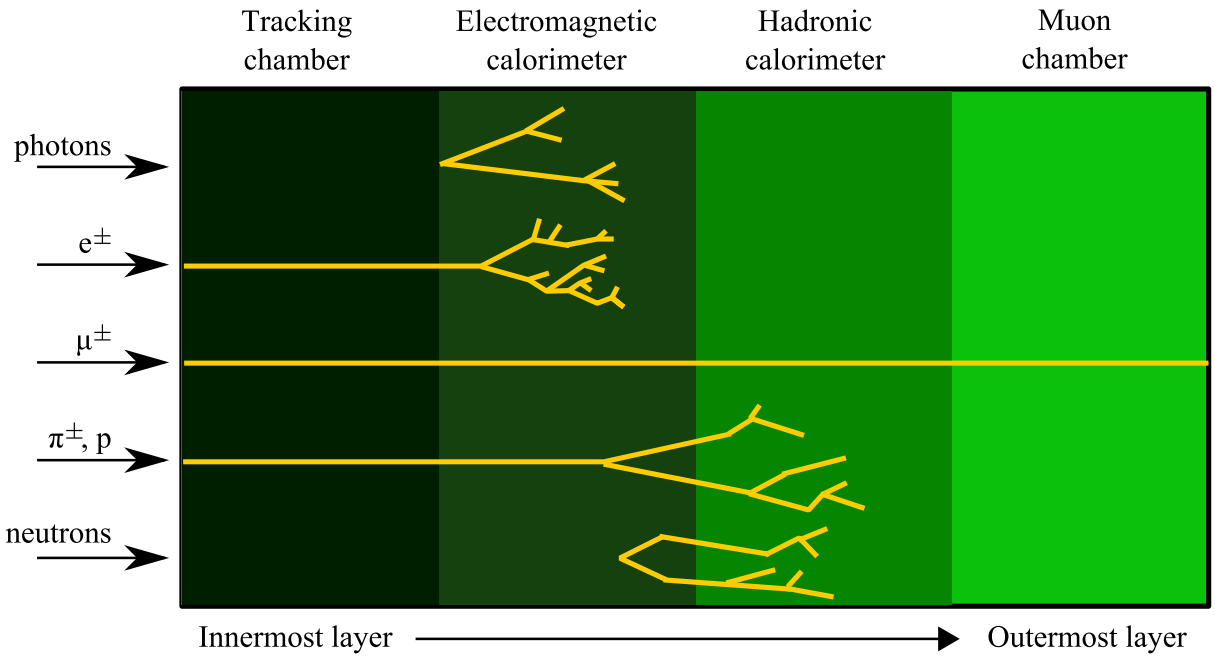

Figure 3.6: Different particles create different calorimeter showers.

3.2.4 Muon System

Beyond the calorimeters resides the muon system, which detects muons in the range $|\eta| < 1.5$. The muon system in the CDF II detector consists of multiple overlapping subdetectors. In general, the muon detectors consists of drift chambers with several layers to record hits, called muon stubs, paired with scintillator layers for further timing information and to help reject the cosmic ray background. The Central MUon detector (CMU) is attached to the hadronic calorimeter and contains four layers of multi-wire drift chambers. The CMU records muon stubs with $p_T > 1.4$ GeV/c [43], within the range $|\eta| < 0.6$. Behind an additional 60 cm of steel, a second set of four drift chambers, the Central Muon uPgrade (CMP) detects muons with $p_T > 2.2$ GeV/c. Behind the CMP lies a set of scintillators, the CSP. These three subdetectors provide coverage in a range of $|\eta| < 0.6$ [44].

Another series of drift chambers, the Central Muon eXtension (CMX) provides coverage from $0.6 < |\eta| < 1.0$ [45]. It too is paired with a set of scintillators, the CSX. In the forward region the Barrel MUon detector (CMU) covers the range $1.0 < |\eta| < 1.5$, with its scintillator counterpart the BSU. The momenta of muons are generally measured in the tracking chambers. Reconstructing a muon consists of matching the muon stub in one of the subdetectors with a corresponding track within the tracking chambers.

3.2.5 Luminosity Counter

The beam luminosity is determined with gas Cherenkov counters located in the region $3.7 < |\eta| < 4.7$ which measure the average number of inelastic $p\overline{p}$ collisions per bunch crossing. The Cherenkov Luminosity Counters (CLC) consist of 3×16 conical shaped gas-filled Cherenkov counters arranged in three concentric cones, all pointing at an angle toward the interaction point; see Fig. 3.7 [46]. These are housed in an aluminum vessel

filled with isobutane gas under pressure. When a particle travels through a material faster than the speed of light (in said material) it emits Cherenkov radiation. The angle of the radiation, or the Cherenkov angle, is $\theta_C = \cos^{-1}(\frac{1}{n\beta})$ where n is the index of refraction of the material. Isobutane gas has an index of refraction of 1.00215, which results in a $\theta_C = 3°$. The momentum thresholds for this radiation is 9.3 MeV/c for electrons and 2.5 GeV/c for pions. PMTs at the end of the Cherenkov cones read the light from this radiation.

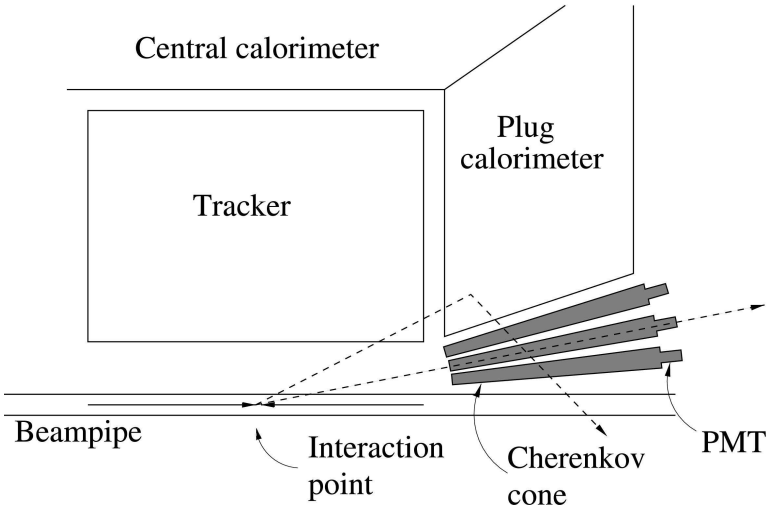

Figure 3.7: Longitudinal view of the CDF detector with CLC detectors highlighted.

The luminosity is recorded by the CLC detectors after counting the number of interactions per bunch crossing. The total uncertainty on the luminosity is ±6.0%, of which 4.4% comes from the acceptance and operation of the luminosity monitor and 4.0% from the calculation of the inelastic $p\overline{p}$ cross section.

3.2.6 Trigger

The Tevatron collides proton-antiproton bunches once every 396 ns or at a rate of approximately 2.5 MHz. It is not possible to collect data at this rate, nor possible to store the

immense amounts of data that would be generated. The majority of events that occur at CDF are "minimum bias" events which are inelastic scatterings with little momentum transfer between the constituent quarks in the proton anti-proton interaction. The cross-section of interesting physics events are orders of magnitude smaller than these events. Thus the trigger system at CDF is responsible for selecting events which have interesting characteristics.

CDF employs a three level trigger system to select interesting interactions, where each subsequent level reduces the amount of data being collected. Figure 3.8 diagrams the data flow of the trigger system. The first level trigger, level-1 or L1, is a hardware trigger, meaning it consists of electronic boards which make decisions on simple objects read out from the detector. For example a calorimeter cluster that has high energy may fire one of many L1 triggers. L1 reduces the interaction rate to about 25 to 30 kHz. This reduces the amount of data by over 99%. The level-2 (L2) trigger system employs both hardware electronics to form more complex objects, such as displaced tracks, as well as software processors to make event decisions. The maximum L2 output rate is approximately 700 Hz. Finally the level-3 trigger (L3), which consists of a farm of processors, performs event reconstruction and reduces the event rate to about 100 Hz. If an event passes through all three levels of the trigger system, it is written to a mass storage system.

Figure 3.9 shows a block diagram of the L1 and L2 trigger subcomponents. The L1 trigger receives detector information from the CDF II detector. L1 modules include the L1 CALorimeter crates, L1 Muon electronics, as well as the eXtremely Fast Tracker (XFT), which consists of the 2D Finder, 2D Linker, and Stereo Linker Association Module (SLAM) components in the block diagram. L1 tests a limited group of selection requirements called primitives. L1 triggers consist of logical ANDs and ORs of the primitives and are evaluated in the Global L1 decision maker. There are a maximum of 64 L1 triggers. The L2 Trigger consists of separate components which collect data from both the detec-

tor and the L1 system. These are read into 4 L2 buffers. Data from the L2Cal trigger subcomponent, CES (ShowerMax) detectors, Silicon Vertex Tracker and Global L1 are fed into a dedicated PC. This computer evaluates the L2 trigger tests on the event and passes successful events onto L3. Finally, the software event builder processes the event and sends it to a farm of computers, the L3 trigger, which reconstructs and evaluates the whole event [47].

One subsystem of the L2 trigger is the Silicon Vertex Trigger (SVT). The SVT is an important part of this analysis. The SVT uses hardware electronics to analyze the silicon hits left by charged particle tracks in the Silicon subdetectors. These hits are quickly mapped into tracks, each with a momentum, a ϕ, an impact parameter (d_0) of the track relative to the beamline, and limited stereo information about the track [48] [49]. Thus it is possible to design a trigger which fires on a track which is displaced from the interaction vertex with a large impact parameter. Since this analysis is a search for particles which decay at a distance from the primary interaction, their daughter particles will originate from a secondary or displaced vertex. The trigger used for this analysis takes advantage of the SVT in order to enrich the signal sample with displaced tracks arising from a displaced vertex while reducing the QCD background present at a hadron collider.

A Trigger path is a set of L1, L2, and L3 triggers that make a sequential series of decisions in order to select specific events. Trigger paths at CDF are designed and tested to collect events that are deemed interesting for further study. A trigger path may be created to select a certain signature in a subdetector, e.g., jet triggers at CDF select events with high energy calorimeter clusters which can be reconstructed as a jet, or high p_T lepton triggers select events which can be used to study top quark decays and $W^{\pm}$ or Z^0 boson properties. Some trigger paths are more specialized, such as the ZBB trigger path used in this analysis, which is detailed in Section 3.2.7.

3.2.7 ZBB Trigger Path

$Z \to b\bar{b}$ events are collected at CDF for the purposes of studying the Jet Energy Scale (JES) of b-quark jets [50]. A dedicated trigger has been designed to collect such events [51]. The ZBB trigger path collects events where there are tracks with a large impact parameter with respect to the primary vertex (d_0), i.e., displaced tracks. Because the Hidden Valley particle will decay at a displaced vertex, tracks from this decay have large d_0. Thus we use this trigger path in our analysis for our signal search.

Table 3.1 summarizes the ZBB trigger for what is termed trigger chunk 17. The ZBB trigger path has been modified multiple times throughout its history in order to optimize it for progressively higher luminosities. However, trigger chunk 17 has been in use since the Fall of 2005. This trigger configuration represents approximately 75% of the data collected with this trigger. At level-1, the trigger has two parts. It selects events with one central calorimeter tower with $E_T > 5$ GeV, and two XFT tracks, one track with $p_T > 5.48$ GeV, the other one with $p_T > 2.46$ GeV.

Level-1	one central calorimeter tower with $E_T > 5$ GeV; two tracks: one track with $p_T > 5.48$ GeV, one with $p_T > 2.46$ GeV
Level-2	veto events with a calorimeter cluster with $E_T > 5$ GeV, $1.1 < \|\eta\| < 3.6$; requires two clusters $E_T > 5$ GeV, $\|\eta\| < 1.1$, which have $9 < \Delta Wedge < 12$; two SVT tracks with $p_T > 2$ GeV, 160 μm $< \|d_0\| < 1000$ μm, $\chi^2 < 12$
(OS)	$150^\circ < \Delta\phi < 180^\circ$
(SS)	$2^\circ < \Delta\phi < 30^\circ$
Level-3	two $\Delta R = 0.7$ jets with $E_T > 10$ GeV, $\|\eta\| < 1.1$; two SVT tracks with $p_T > 2$ GeV, $\|\eta\| < 1.2$, 160 μm $< \|d_0\| < 1000$ μm; two COT tracks with $p_T > 1.5$ GeV $\|\eta\| < 1.2$, 130 μm $< \|d_0\| < 1000$ μm; impact parameter significance $S(d_0) > 3$, $\Delta z < 5$ cm

Table 3.1: ZBB trigger path for trigger chunk 16 and 17. One of the two Level-2 paths (OS or SS) must be satisfied.

At level-2, there are two different subpaths which the trigger can take, named opposite side (OS) and same side (SS), which refer to the topological configuration of the displaced

tracks in the event. The OS path consists of three parts: a plug jet veto, a central calorimeter requirement, and displaced track requirement. The plug jet veto requires that there are no calorimeter clusters with $E_T > 5$ GeV in $|\eta| > 1.1$. The plug jet veto is designed to reduce the rate at which this trigger collects data at high luminosity. The trigger requires two central calorimeter clusters, $E_T > 5$ GeV and $|\eta| < 1.1$, which are on opposite sides of the calorimeter. Finally, the track requirements at level-2 are two SVT tracks which must point to one of the aforementioned clusters, with track $p_T > 2$ GeV, 160 μm $< |d_0| <$ 1000 μm, $\chi^2 < 12$. The two tracks must have $150° < \Delta\phi < 180°$. The $|d_0|$ requirement selects displaced tracks. The SS path is similar to the OS path in that both have a plug jet veto and central calorimeter requirements. However, the SS path requires that the two displaced tracks point to a single cluster, and that $2° < \Delta\phi < 30°$.

At level-3, the trigger requires two cone $\Delta R = 0.7$ jets with $E_T > 10$ GeV and $|\eta| < 1.1$. (ΔR is defined as $\Delta R = \sqrt{(\Delta\phi)^2 + (\Delta\eta)^2}$.) It then also requires two tracks with 160 μm $< |d_0| <$ 1000 μm, simply verifying what was required at level-2. As a cross-check, this requirement is performed with both SVT tracks and COT tracks.

Approximately 85% of the data collected by the ZBB trigger was done so by trigger chunks 16 and 17; see Table 3.2. Of the remaining 15%, most of it was collected using a slightly different level-2 requirement. There was no OS or SS path, instead there was only a $\Delta\phi > 2$ cut on both tracks. The OS and SS paths were introduced in order to reduce the trigger rate for high luminosity running. level-1 and level-3 were not different.

For some earlier runs, a "test" trigger path (TEST_ZBB) was introduced in addition to the production trigger path (ZBB). This test path was designed to test a trigger configuration before it replaced the ZBB trigger. Whenever possible, we use the test trigger as it collected data using the SVT, i.e., it had the level-2 displaced track requirement. There are 17 different trigger chunks in the ZBB trigger. We use data from trigger chunks 6 through 17, with the exception of chunk 7. The run number ranges and trigger path

names used in this analysis are listed in Table 3.2.

Chunk number	Trigger path name	Starting run number	Ending run number
6	TEST_Z_BB_v-1	168,086	179,869
8	TEST_Z_BB_v-4	179,871	181,235
9	TEST_Z_BB_v-4	181,236	181,801
10	Z_BB_v-12	181,839	183,701
11	Z_BB_v-13	183,702	184,310
12	Z_BB_v-13	184,311	184,424
13	Z_BB_L2_DPS_v-1	184,439	184,802
14	Z_BB_L2_DPS_v-2	184,826	191,205
15	Z_BB_L2_DPS_v-2	191,208	200,899
16	TEST_Z_BB_L2_BJET_OS		
	TEST_Z_BB_L2_BJET_SS	200,900	209,770
17	Z_BB_L2_BJET_OS_L1_LUMI_110		
	Z_BB_L2_BJET_SS_L1_LUMI_110	209,771	209,907
17	Z_BB_L2_BJET_OS_L1_LUMI_150		
	Z_BB_L2_BJET_SS_L1_LUMI_150	209,910	265,140
17	Z_BB_L2_BJET_OS_L1_DPS		
	Z_BB_L2_BJET_SS_L1_DPS	265,142	(ongoing)

Table 3.2: Run number ranges and ZBB trigger path names for different chunks used in this analysis. There are multiple versions of trigger chunk 17, but they only deal with luminosity.

The ZBB trigger luminosity is summarized in Table 3.3. Unless otherwise specified, we use data from periods 0 through 25 in this analysis. (Data collected at CDF is split into time periods for bookkeeping purposes. Periods 0 through 25 corresponds to data from February 2002 through June of 2009.) The total luminosity collected during this period is 5.8 fb^{-1}, but because the ZBB trigger is prescaled, it collected ~ 3.2 fb^{-1}.

3.2.8 Event reconstruction

Once events pass through the trigger system, they are reconstructed into objects that can be used in a physics analysis. This analysis mainly uses reconstructed tracks and reconstructed jets, although reconstructed muons are also used. In addition, primary vertex

Trigger path name	**Luminosity (pb^{-1})**
TEST_Z_BB	15.64
Z_BB	87.14
Z_BB_L2_DPS	373.78
TEST_Z_BB_L2_BJET (OS & SS)	44.90
Z_BB_L2_BJET_OS_L1_LUMI_110 (OS & SS)	12.09
Z_BB_L2_BJET_OS_L1_LUMI_150 (OS & SS)	1751.17
Z_BB_L2_BJET_SS_L1_DPS	963.13
Total Luminosity	3247.85

Table 3.3: Luminosity collected with the ZBB trigger.

and secondary vertex reconstruction is very important for searching for the signature of displaced vertices.

The tracking chambers at CDF are described above in Sections 3.2.2. Charged particles leave trajectories of hits in the tracking chambers. Because the tracking system is enclosed in a uniform magnetic field, with field lines parallel to the z-axis, the charged particle experience a Lorentz force proportional to their momentum in a direction perpendicular to the field lines. This results in the trajectory of the tracks being a helix. There are six helix parameters which define a track at CDF [52] [53].

1. C - the curvature of a track, which is inversely proportional to its momentum

2. cot θ_0 - cotangent of the polar angle at the trajectory point closest to the beamline, often abbreviated as λ .

3. ϕ_0 - the azimuthal angle of the trajectory at the point closest to the beamline.

4. d_0 - the impact parameter, the minimal distance between the trajectory and the beamline in the plane transverse to the beamline

5. z_0 - the distance between the trajectory point closest to the beamline and the origin along the z-axis.

Tracks in CDF are generally reconstructed in two ways, Outside-In tracks (OI tracks) or Silicon Standalone tracks. In the central region ($|\eta| < 1$) where coverage is provided by the COT, the Outside-In algorithm is preferred. This algorithm starts by reconstructing hits in the COT. These hits are then fit to a helix. If the fit succeeds, the algorithm attempts to match Silicon hits to this predefined helix. The hits are attached to the helix from the outermost layer to the innermost layer

Silicon Standalone tracks are constructed using hits in the Silicon detectors only. Generally, these tracks are not used in this analysis.

Clusters of energy collected in the calorimeter are reconstructed as jets. Hard scattering of the quarks in the proton with antiquarks in the antiprotons creates multiple products, including other quarks and gluons (partons) via QCD processes. These partons undergo a complex decay process leaving the interaction region. First they fragment creating multiple partons in a cascade of gluon emissions. These partons then form colorless hadrons (hadronization). Some of these hadrons are non-stable and decay to stable particles. These particles reach the CDF calorimeter and deposit their energy within.

In this analysis the jets are reconstructed with the JetClu algorithm [54] which only requires information from the calorimeters. This algorithm is a seeded cone algorithm. The opening angle of the cone is taken to be $\Delta R = 0.4$. (ΔR is defined as $\Delta R = \sqrt{(\Delta\phi)^2 + (\Delta\eta)^2}$.) The algorithm searches for seed calorimeter towers with $\mathrm{E_T} > 1$ GeV. The $\mathrm{E_T}$ is defined as

$$E_T = E^{EM} \sin\theta^{EM} + E^{HAD} \sin\theta^{HAD}, \tag{3.2}$$

where θ is the polar angle. Towers within a cone of $\Delta R = 0.4$ around the seed are added to the jet, and a new $\mathrm{E_T}$-weighted jet centroid is calculated. The process is repeated until the list of towers assigned to a jet is stable. If two jets overlap and share more than 50%

of their energy, they are merged, and if a tower is part of two different jets, it is assigned uniquely to the closer jet.

Reconstruction of muons is performed by matching hits in the muon detector(s) (stubs) with tracks in the tracking chambers, with quality cuts to ensure both purity and efficient reconstruction. Muons used in this analysis are known as CMUP muons because stubs are left in both the CMU and CMP systems. (Other muon systems are unused for the purposes of this analysis.) Specific muon selection criteria are described in more detail later.

Vertices are found in the intersection of multiple tracks. Reconstruction of the primary vertex is important because, for this analysis, the definition of a displaced vertex is one that is some distance away from the primary vertex. Primary vertex reconstruction at CDF is done with two algorithms, both of which are used in this analysis. The `ZVertex` finder attempts to find the primary vertex z-position by taking the weighted average of all the z_0s of tracks in the event, weighted by the resolution of the z_0, σ_{z_0}. A second algorithm, known as PrimeVtx attempts to fit the tracks using CTVMFT, a vertex minimization utility [55]. This algorithm begins with a seed position, typically the average beam spot position. Then tracks in decreasing order of their p_T are fit onto the vertex using CTVMFT. Tracks are then pruned from the vertex for contributing too large of a χ^2 to the vertex, until some set of quality cuts have been satisfied. The PrimeVtx gives the x, y, and z information of a primary vertex.

Generally, for this analysis, vertices are selected using the both algorithms. A seed vertex is found in the ZVertex block. A vertex in the ZVertex block is considered the "best" vertex for a seed candidate when it has the highest Σp_T of the tracks attached to the vertex. Then the closest PrimeVtx in the z-direction is selected as the primary vertex in the event. The vertex must also satisfy the condition $z_0 < 60$ cm.

3.2.9 Introduction to Secondary Vertices

In order to find particles that decay with a displaced vertex, the CDF reconstruction software employs a number of secondary vertex tagging algorithms. We adopt one such secondary vertex tagging algorithm, SecVtx, for our own needs for this analysis. A detailed explanation of the tagging algorithm is given in Section 4.4. The following paragraphs describe an overview of the algorithm.

When a long-lived particle, such as a B hadron, is created at the primary interaction vertex of a $p\overline{p}$ collision the particle may live for a few picoseconds before decaying into its daughter particles. This decay results in tracks that originate away from the primary vertex. Vertexing these displaced tracks into a secondary vertex is the job of the b-tagging algorithm SecVtx. SecVtx makes a series of cuts to select tracks that are displaced from the primary vertex and attempts to vertex them together into a secondary vertex. If a vertex is made, another series of cuts is used to only select secondary vertices of high quality. The intent of this b tagger is to identify B hadron jets originating from a top quark decay, which has a branching ratio of over 95% into a W boson and a b quark.

Mistags are light-flavor (up, down, strange, and gluon) jets that have been erroneously tagged as having a secondary vertex. Mistags arise from multiple sources, which include long lived Λs and K_Ss as well as nuclear interactions and other material effects within the detector. Tracking errors and other mis-reconstructions also produce errant tracks that can be vertexed as a mistag. While effort has been made to eliminate these mistags, some do occur.

B hadrons originating from the primary vertex produce tracks that are displaced. This displacement is measured in terms of the d_0 of the track. Because the SecVtx algorithm was designed mostly for top quark physics, the maximum allowed $|d_0|$ of a displaced track is set to a small value: $|d_0|_{max} < 0.15$ cm. It is necessary to alter the algorithm to search

for our signal, because tracks that originate from a Hidden Valley displaced vertex can have impact parameters larger than this value. However, this adjustment may increase the number of mistags.

Section 4.4 discusses in more detail the custom b-tagging algorithm that we implemented, named TStnSVF, which is used to increase the efficiency of b tagging the jets arising from displaced vertices.

3.2.10 Software

For the purposes of this document, some basic CDF software terminology is defined here. The program PRODUCTION reconstructs the events as described in Section 3.2.8. Such events are said to be Production-level events. After events are processed through PRODUCTION they are typically "Ntupled" into another data format, for faster processing. This analysis uses the STNTUPLE, an abbreviation for STandard NTUPLE. Data which are processed by the STNTUPLE are said to have been "Stntupled".

Different trigger paths processed by PRODUCTION are given six letter identifiers, e.g., `ezbb0j`. These data are typically Stntupled into different datasets, which also use six letter identifiers, e.g., `ezbbbj` is the STNTUPLE dataset which corresponds to the `ezbb0j` PRODUCTION dataset. Unless otherwise specified, the datasets listed in this document are Stntuple datasets.

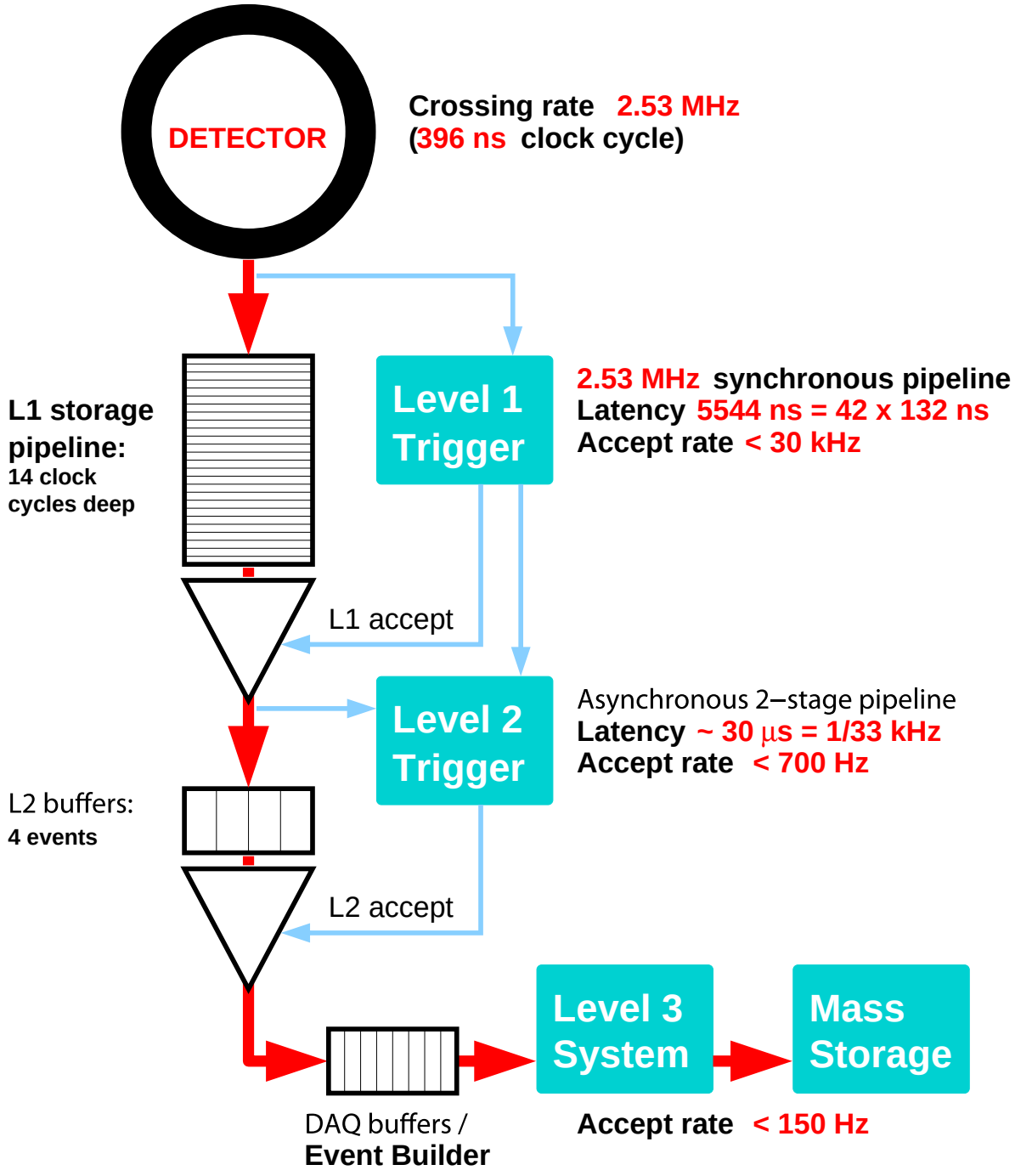

Figure 3.8: Diagram of the CDF Trigger system

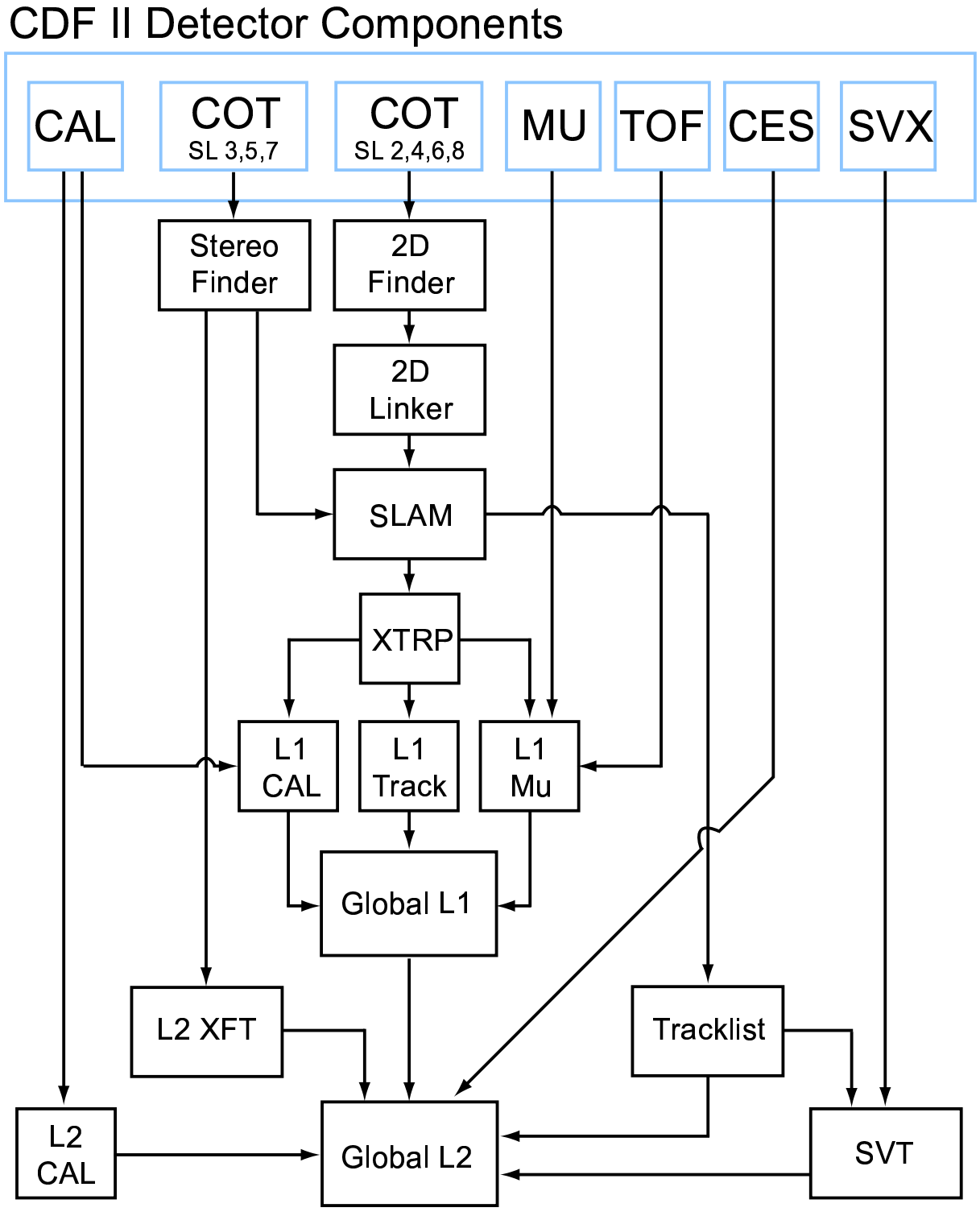

Figure 3.9: Components of the CDF Trigger System for Levels 1 and 2.

CHAPTER 4

ANALYSIS STRATEGY AND BACKGROUND ESTIMATION

4.1 Analysis Overview

In this section the main outline of the analysis is presented. Many topics have an entire section devoted to explaining that topic in greater detail. Here, a short introduction or overview of the topic is meant to provide an overview of the analysis as a whole.

4.1.1 MC Studies

MC studies are discussed in detail in Section 4.2. We produced signal MC samples to understand how the decay of the HV particle is seen in the CDF detector. These signal MC samples allow us to identify discriminants as well as provide a benchmark for the displaced vertex analysis.

4.1.2 Event Selection

The signal we are searching for involves particles (quarks) that originate from a displaced vertex. The Z to $b\overline{b}$ trigger at CDF selects events with displaced tracks. Thus this trigger, called the ZBB Trigger, is the source for our signal data. The trigger is described in detail in Section 3.2.7.

After the trigger selection, there is an additional event selection. First all the jets in this analysis must satisfy some basic requirements. Jets used in this analysis are reconstructed with a $\Delta R = 0.4$ cone using the JetClu algorithm. The E_T of the jet after Level-5 Jet Energy Scale (JES) [56] corrections must be greater than 20 GeV, $E_T^{L5} > 20$ GeV. The jets must be in the central region of the detector, $|\eta| < 1.0$. This

requirement overlaps with the ZBB trigger requirement. These jets will be referred to in this document as tight-central jets.

The JES is a series of corrections made to jets in order to properly account for their energy. The energy deposited in the calorimeter at CDF is adjusted for multiple effects.

1. Relative Energy : corrects for the non-uniform η response in the calorimeter.

2. Multiple Interactions : subtracts effects from multiple collisions in the event.

3. Absolute Energy Scale : converts the calorimeter energy into particle energy.

4. Underlying Event : removes energy from the underlying event.

5. Out-of-cone Energy : adds radiation outside the jet's ΔR cone.

A Level-5 corrected jet includes all but the last two items in the above list. Unless otherwise specified, the jets in this analysis are corrected at Level-5.

Further selection cuts are used to define a signal region. This region has three or more central 20 GeV jets, with a jet pair considered if it has an opening angle $\Delta R < 2.5$. We also define a control region, in which events have exactly two jets with $E_T^{L5} > 20$ GeV, and a third jet with low transverse energy, $E_T^{uncorr} < 15$ GeV. There is no ΔR cut in this region. This control region is used to cross-check the algorithm for creating the background estimate.

4.1.3 Modeling Background with Data

We want to model the SM backgrounds to the signal signature using real data. The ability to find particles with displaced vertices relies on the reconstruction of secondary vertices. These secondary vertices can come from multiple SM sources, for example QCD

Background	**SM Production**
b-quarks	QCD $b\bar{b}$, $t\bar{t}$, WZ/ZZ
c-quarks	QCD $c\bar{c}$, WZ/ZZ
light-flavor (mistags)	QCD $q\bar{q}$ & gg, hadronic τs

Table 4.1: Standard Model processes that can produce particles that decay with a displaced vertex. This table is not complete, but represents the majority of expected background processes.

production of $b\bar{b}$ production. Table 4.1 shows a list of multiple SM sources that produce secondary vertices.

The Monte Carlo simulation that is normally used to model backgrounds is inadequate when it comes to modeling these secondary vertices. One major concern is the effect mistags have in this analysis. Mistags tend not to be modeled correctly in the MC simulation. One reason is that the detector material is not fully modeled in the CDF detector simulation. By using a data-driven background we hope to accurately model what background exists in the signal region. In addition, this data driven background encapsulates different SM background sources, such as those listed in Table 4.1. This eliminates the need to generate all SM background processes with MC.

4.1.4 Building p.d.f.s

The first step in modeling the background is to build standard model secondary vertex probability density functions (hereinafter just p.d.f.s) from b-tagged jets from background processes. These p.d.f.s involve multiple variables, described below, which characterize a secondary vertex within a jet. We split these p.d.f.s into three main categories, or quark flavors: b quark, c quark and light-flavor jets. The p.d.f.s are constructed from data events where the signal is not expected to be present, and in effect encapsulate standard model secondary vertex information.

We use these p.d.f.s by applying them to multi-jet data, in which we are searching for

the signal, to build a background estimate. While the kinematic information will come from the real event, the p.d.f.s are used to characterize secondary vertices in the real jets. These secondary vertices constructed from the p.d.f.s represent the background from the SM. When searching for our signal, we can use the kinematic information from the event, jet E_T η, etc. while constructing a secondary vertex that would represent processes from the SM, and not our signal. By comparing the events with these constructed secondary vertices (called "pseudo events") with real data events, we can search for the presence of new physics phenomena.

The jets that form these p.d.f.s are split in different bins of E_T and are also split into three different categories of "number of SVT tracks." The ZBB trigger requires that there be two tracks that satisfy the trigger's SVT requirement. This can be satisfied by two tracks in one jet, or one track in each of two jets. Thus we split the jets into bins of zero, one, and two or more SVT tracks, which would satisfy the ZBB trigger SVT requirements. As SVT tracks are displaced tracks, their presence is a likely indicator of heavy flavor decay. This binning in E_T and the number of SVT tracks is chosen because the secondary vertex probability for a jet changes with both E_T and the number of SVT tracks, and thus the p.d.f.s' shapes are different for each of the different bins.

The construction of these p.d.f.s is detailed in Section 4.5.

4.1.5 Creating a Background Estimate

The background estimate is created from the same data sample used to search for the signal. Events in the ZBB trigger are used for this construction. Only events in either the signal or control regions are selected, and separated such that there is a separate signal and control region background estimate. After events in the ZBB trigger are selected, they are sent through a pseudo event generation process. Details of this algorithm are described in Section 4.6.

A pseudo jet is constructed for each real jet in the event. The pseudo jets are first given pseudo b tags. This pseudo b tag is generated using the probability that a jet in this sample has a b tag. Thus not all pseudo jets will have pseudo b tags, but the proportion that do will be the same as the proportion of real jets with real b tags. Next the flavor of the pseudo jet is generated. The probability of a jet being a b quark, c quark, or light-flavor jet is used to generate the flavor. Finally, the secondary vertex information is sampled from the p.d.f.s. In this way a pseudo event contains all the kinematics of the real event it is generated from, but the secondary vertex information comes from the SM background via the p.d.f.s. As a result the background estimate is the number of events that we expect in the signal region due to SM processes.

4.1.6 Analysis: Counting Experiment

The analysis itself is a counting experiment as described in Section 5.1. A number of variables are used in order to try to separate signal events from background. A series of cuts is made in order to reduce the background while keeping signal efficiency high. The variables include the opening angle of the dijet pair (ΔR) as well as two new variables developed for this analysis, ψ and ζ. These latter two are described in much more detail in Section 4.2.2.

Section 5.1 also discusses the optimization analysis to determine the final cuts. It also discusses how we generate multiple "pseudo experiments" in order to build a background estimate that represents the SM. Systematic uncertainties are discussed in Section 5.2 and a limit is set on the Hidden Valley model in Chapter 6.

4.2 MC Studies

4.2.1 MC Generation

According to [28], the Hidden Valley model encompasses a wide range of Higgs masses, HV particle masses, and HV lifetimes. Thus the first step for this analysis is to generate signal Monte Carlo (MC) simulation for this model. We choose a HV lifetime of $c\tau_{HV} = 1.0$ cm as our main lifetime to study. As with any exponential process, the most likely decay is at the origin. However, at 1.0 cm the tail of the decay distribution is not excessively large. Most decays will occur within the beampipe of the detector, $r = 1.26$ cm, and before the first layer of the SVX II detector, $r = 2.5$ cm. The latter is important because the b-tagging algorithm we use in this analysis requires hits in the SVX II.

Two Higgs masses are generated, one at relatively low mass, 130 GeV, and one at high mass, 170 GeV. SM Higgs production is used, as per the Hidden Valley model, $gg \to h_0$. However, the Higgs is constrained to decay into the HV particle, $h_0 \to a^0 a^0$. Here the a^0s are not the MSSM Higgs partners, but simply represent the HV particle. This allows us to generate the signal MC using the Pythia MC generator without significant modification. The a^0 has its mass artificially set to a HV particle mass, and its lifetime set to a HV particle lifetime. Finally, the a^0 has its decay daughters constrained to $b\bar{b}$ quark pairs.

The Pythia MC program version 2.6 is used to generate the events for the signal MC [57]. In addition, CDF Tune A for the underlying event is included. GEANT is used for the detector simulation. The main process generated is $h_0 \to a^0, a^0 \to b\bar{b}, b\bar{b}$. The different Higgs and HV masses, along with the HV lifetimes are listed in Table 4.2.

These MCsets are then ntupled into STNTUPLE format. (To form the STNTUPLE MCset name, replace the '`p`' with an '`s`'.) Approximately 1 fb^{-1} of signal MC is generated for each sample. These MC events are used to determine discriminants and to calculate the expected number of signal events.

Higgs Mass (GeV)	HV Mass (GeV)	HV life-time (cm)	MCset name
130	20	1.0	ahhp2d
	40	1.0	ahhp2i
170	20	1.0	ahhp2s
	40	1.0	ahhs2x
	65	1.0	ahhs22
130	40	0.3	(reweighted ahhp2i)
		2.5	(reweighted ahhp2i)
		5.0	(reweighted ahhp2i)

Table 4.2: Hidden Valley model Higgs and HV mass points generated. Replace the 'p' with an 's' for the `Stntuple` MCset name.

While the signal MC is generated with a HV lifetime of $c\tau_{HV} = 1.0$ cm, we reweight the signal MC events to study other values of $c\tau_{HV}$. Events are weighted based on the generated lifetime (1.0 cm) and a new lifetime. The resulting event has been weighted to represent its contribution if the lifetime of the HV were 0.3, 2.5, or 5.0 cm. This is done at a single Higgs and HV particle mass of 130 GeV and 40 GeV respectively; see Table 4.2. In this manner, we can search for different lifetimes of the HV particle in the data.

Figure 4.1 shows the $c\tau_{HV} = 1.0$ cm (blue) sample reweighted to 0.3 cm (magenta) and 2.5 cm (cyan). The latter two samples can be used to set benchmarks on different HV particle lifetimes without generating more signal MC samples.

4.2.2 Search for Discriminants

With the signal MC generated, we proceed to perform simple MC vs. MC studies to understand the detector response to our signal. To that end, the Hidden Valley signal MC is compared to a QCD $b\bar{b}$ MC sample which dominates our background. (The signal MC is compared to the `iqcdtd` MC set.) Neither of these samples had their cross-section normalized. As a result, only the shapes of the two MC samples are compared. The

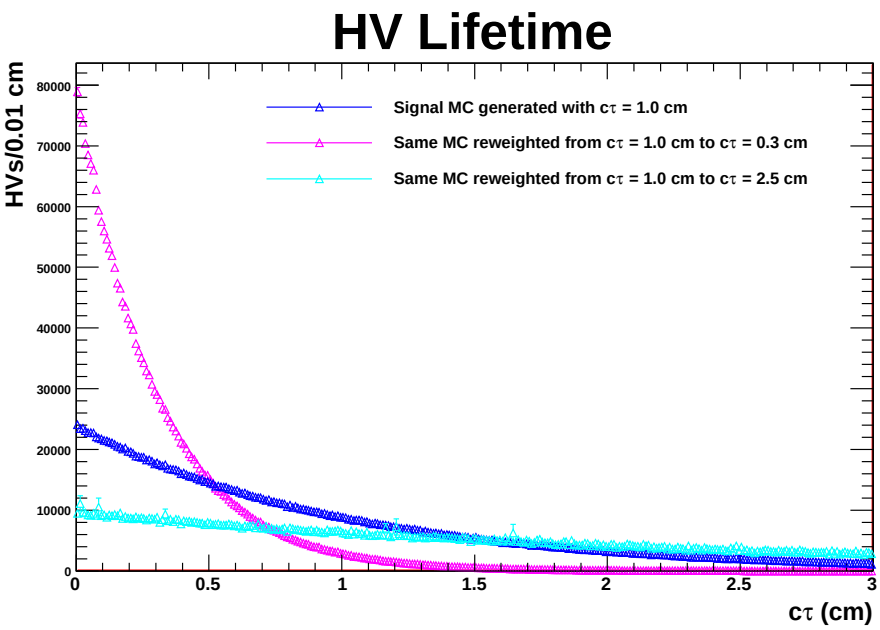

Figure 4.1: Lifetimes ($c\tau_{HV}$s) of different signal MC samples. The blue is the sample generated with $c\tau_{HV} = 1.0$ cm while the magenta and cyan have weighted the original lifetime to 0.3 cm and 2.5 cm respectively.

purpose of this study is to find discriminants in the Hidden Valley process that are different from QCD, which we expect to dominate the background.

Both MC samples are processed identically. Both are also subject to a trigger simulation, specifically the ZBB Trigger path; see Section 3.2.7. After simulating the trigger, we begin by looking at the properties of SecVtx b-tagged jets in each sample in order to try and find discriminants.

One effect was noticed fairly quickly, namely that the b-tagging efficiency is lower than expected. The diagram shown in Fig. 4.2 can help explain why. In the figure, the Higgs decays at the primary vertex into two HV particles. The diagram is drawn in a plane transverse to the beamline, and all variables are two-dimensional. The HV particles in turn decay into b quarks which hadronize into jets containing B hadrons (represented by pink cones). Particles that originate from the B hadron decay leave tracks in the SVX

II and COT, which are used to construct secondary vertices/b tags. However, as the diagram shows, the displaced vertex of the HV particle decay can create highly displaced tracks with respect to the primary vertex.

These displaced tracks will be cut out by a maximum $|d_0|$ ($|d_0|_{max}$) cut placed on tracks by SecVtx, which requires tracks with a $|d_0|_{max} < 0.15$ cm with respect to the primary vertex. For more detail on SecVtx see Section 4.4. The result of this cut is that the efficiency for b tags in the signal MC is lower than expected.

It is necessary to increase this cut on the maximum impact parameter of tracks in order to increase the detection efficiency for our signal. At first, this was done manually in SecVtx, but the necessity of having to adjust this and potentially other parameters of the b-tagging algorithm precipitated the need for a custom b tagger, which is discussed in Section 4.4. For the purposes of this section, we show a few different $|d_0|_{max}$ cuts in order to show how we discriminate between the signal and background.

In our search for discriminants we look at multiple variables that would give us power to isolate the signal. However, none of the standard variables used in CDF analyses seem to suffice. Thus, we developed our own variables for this analysis, which take advantage of the displaced vertices present in our events.

Figures 4.3 and 4.4 show diagrams for the two new variables that we develop for this analysis: ψ and ζ. Jets with secondary vertices have a secondary vertex (a position) and the sum of the four momenta of the tracks that make up that vertex (a direction). With a position and a direction we can draw a line in two-dimensional space. We define $\vec{\psi}$, as the orthogonal vector from the primary vertex to this line. The magnitude of this vector, $\psi = |\vec{\psi}|$, is the distance of closest approach of this line to the primary vertex.

ψ can be a signed variable. The dot product of the jet's momentum vector and the ψ vector is calculated, and if positive, ψ is positive; likewise ψ is negative if the dot product is negative. Although this variable is signed, the ψ distribution is symmetric about zero,

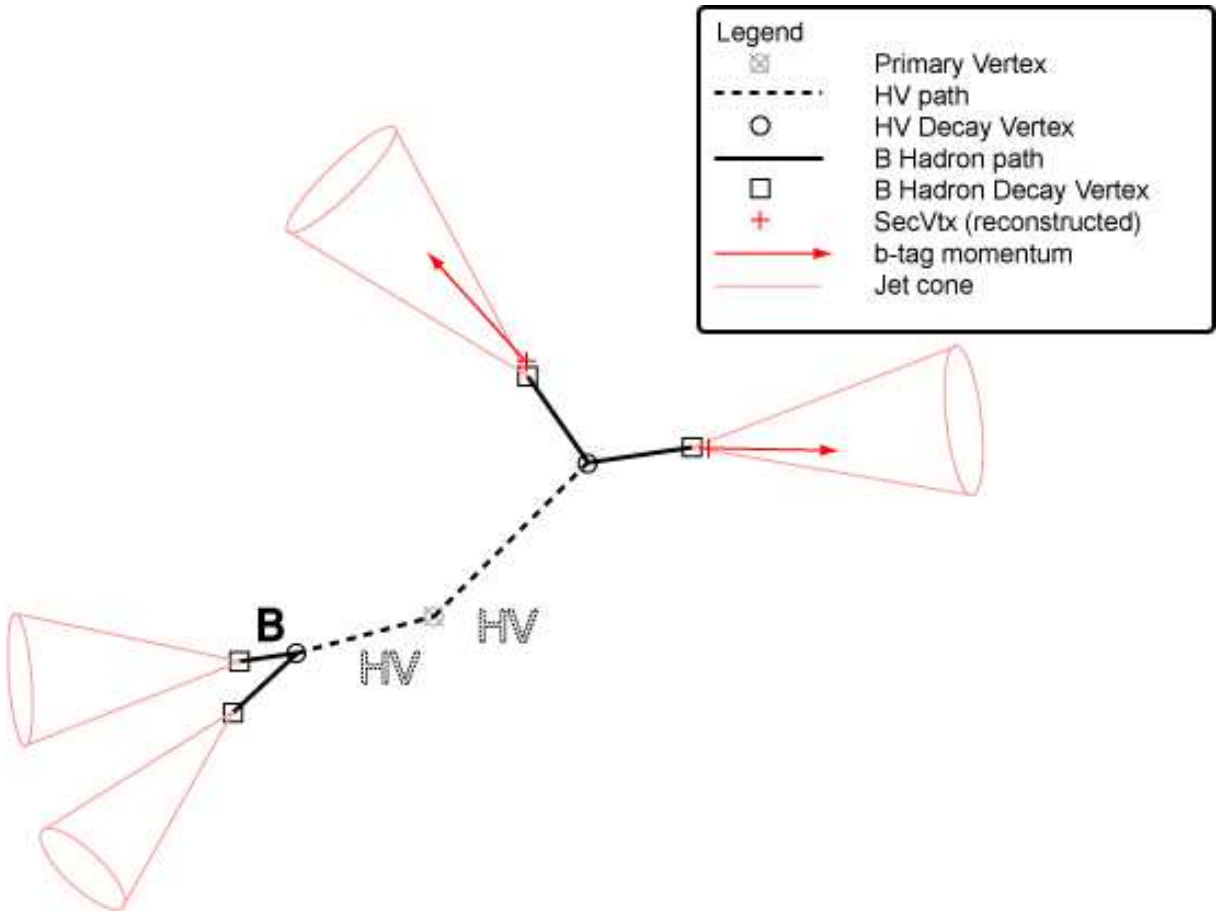

Figure 4.2: Schematic diagram of a Hidden Valley decay with displaced vertices.

and the sign does not add to its discriminating power.

Jets from displaced vertices have larger ψ than SM jets, as shown in Fig. 4.5. In addition, when we increase the $|d_0|_{max}$ cut on the tracks, the number of signal MC jets increases, as seen by larger ψ tails; both distributions are normalized to unit area to compare their shapes.

ζ is defined for events where there are two positive b-tagged jets. With two such jets, we have two vertex positions, and their corresponding directions; see Fig. 4.4. We can construct two lines in two dimensional space. These lines must either be parallel, coincident, or intersect, and in nearly every case they intersect. This intersection can be thought of as the reconstructed decay vertex of the HV particle. The vector from the primary vertex to this reconstructed decay vertex is $\vec{\zeta}$. And the magnitude $\zeta = |\vec{\zeta}|$ is the lifetime or decay distance of the HV particle.

ζ can be signed as well. The sum of the momenta of the two jets with b tags is calculated. The dot product of $\vec{\zeta}$ and this sum is then calculated. If the dot product is positive, then ζ is positive and likewise for a negative dot product. The sign effectively indicates whether or not the decay vertex is in the same hemisphere of the detector as the two jets. Signal MC events have more positive ζ than negative, while the background MC events have ζ uniformly distributed around zero.

Figure 4.6 shows diagrams of what we expect SM background events to look like. Here the two B hadrons are nearly back-to-back. The ψ is almost zero. And ζ is also very small since it is a reconstruction of the primary vertex, with some resolution smearing.

At this point it is necessary to discuss the combinatorics of these HV events, i.e., their topology. With MC we can use the true information from the generator (HEPG) to evaluate if the jets with secondary vertices originated from quarks whose mother is the HV particle. With this information we define four possible topologies in which signal MC events can be classified.

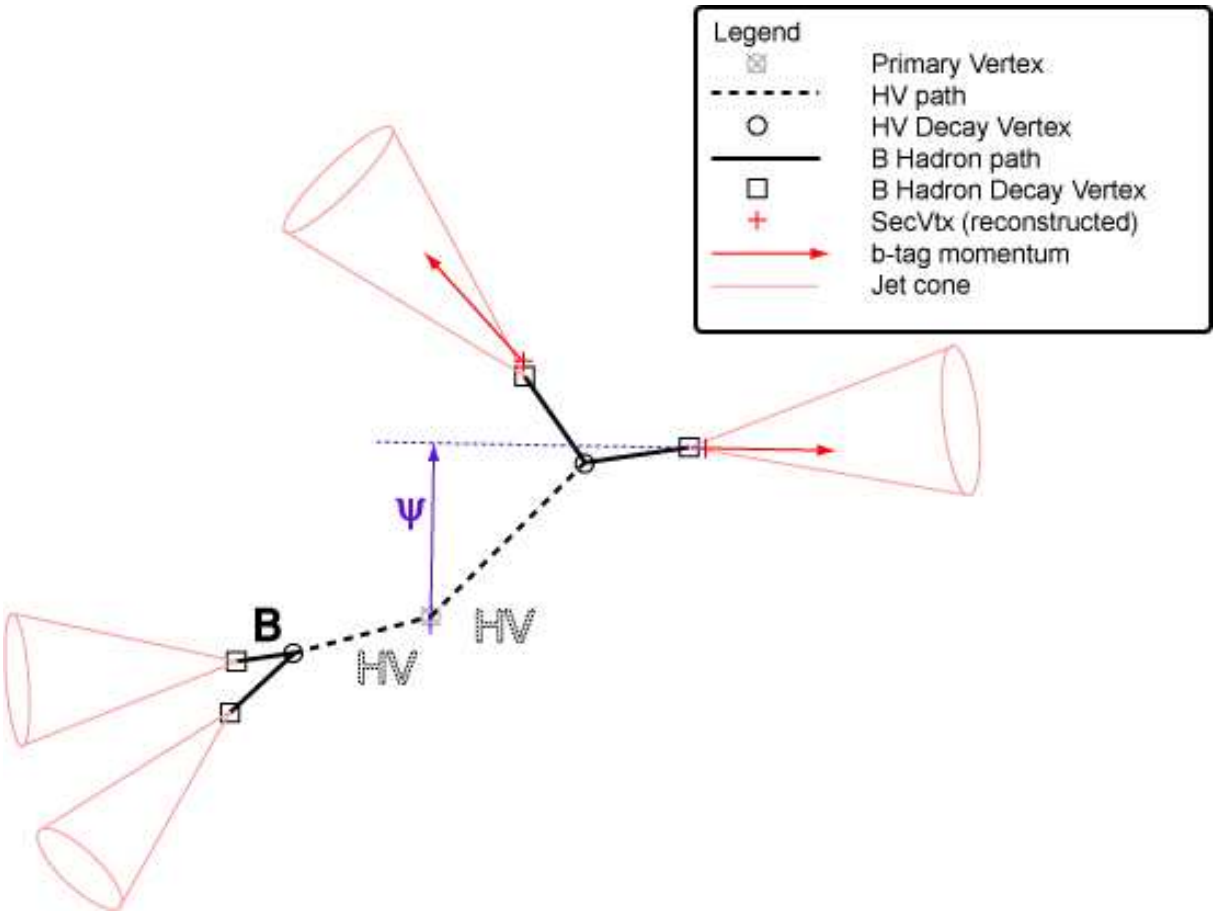

Figure 4.3: Schematic diagram of variable ψ, the impact parameter of a jet with a positive b tag/secondary vertex. This figure is not to scale. The figure is shown in a plane transverse to the beamline.

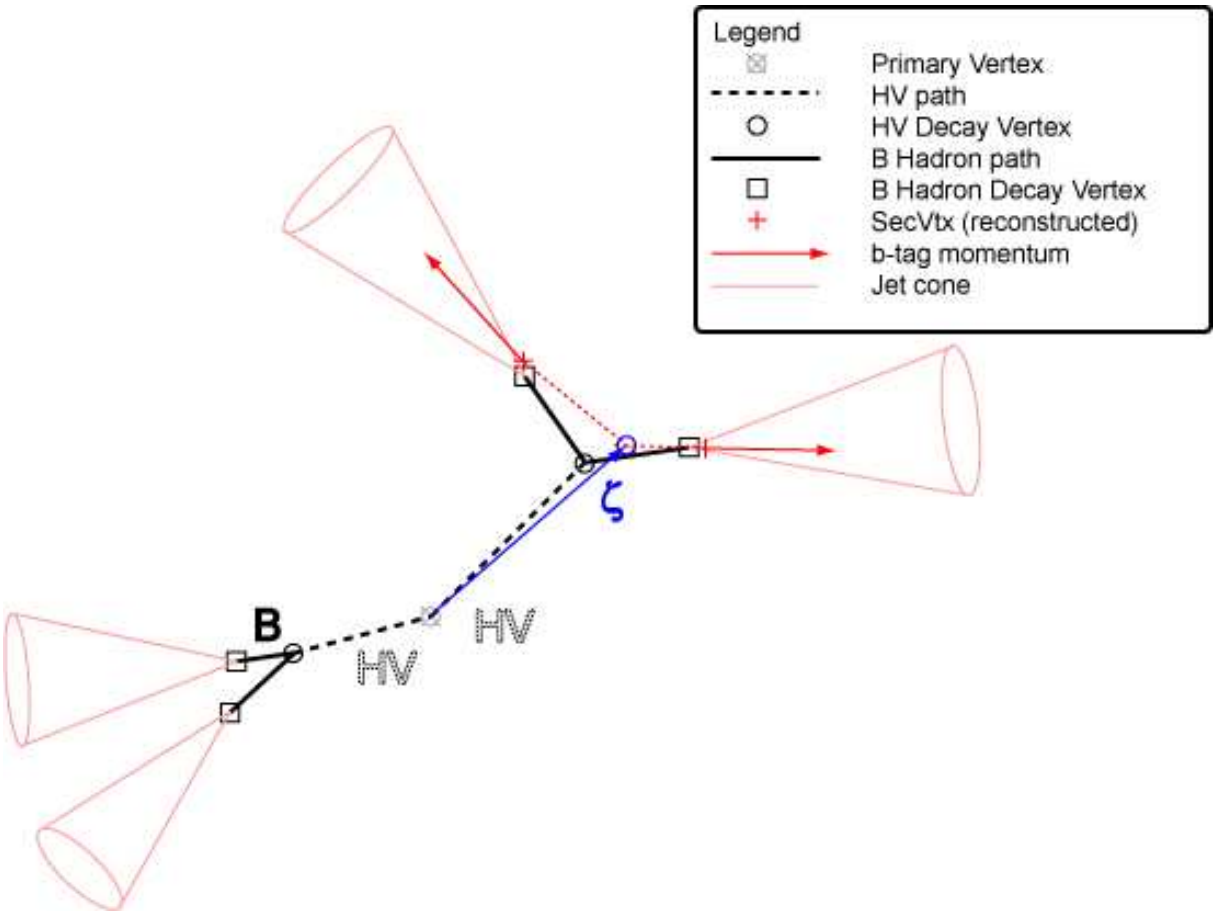

Figure 4.4: Schematic diagram of variable $\vec{\zeta}$ which represents the decay vertex of the HV particle.

1. TwoTag HV : The case where both jets originate from the **same** HV particle.

2. One Tag Each : The case where each jet originates from a different HV particle.

3. One HV Jet : One jet originates from a HV particle, the other does not.

4. No HV Jets : Neither jet originates from a HV particle.

The last two cases are very rare, but are listed for completeness. Of the first two cases, we concern ourselves with the first because it has more discriminating power. ζ has a very different shape for the signal MC TwoTag HV topology compared to the background MC, and even to the OneTagEach topology.

Figures 4.7, 4.8, and 4.9 show ψ and ζ for different signal MC topologies and background MC, each for a different $|d_0|_{max}$ cut. The signal MC topologies are stacked on top of one another. These events are from a single signal MC sample with $M_{h_0} = 130$ GeV, $M_{HV} = 40$ GeV, and $c\tau_{HV} = 1.0$ cm. The b tagger $|d_0|_{max}$ cut for these distributions are set at 0.15 cm, 0.30 cm, and 1.50 cm. These distributions have been normalized to unit area and show the discriminating power of both variables.

The ζ distributions show the reconstructed decay distance of the HV particle. The TwoTag HV in dark blue, which is nearly always positive, acts as a good discriminant against the background. The One Tag Each case in green shows a distribution that is both positive and negative, but mostly negative. In addition to these two variables, the separation of the dijet pairs (ΔR) is a useful discriminant; see Fig. 4.10. Because the ΔR is a kinematic variable and does not deal with the secondary vertex, it does not significantly change as the $|d_0|_{max}$ cut changes.

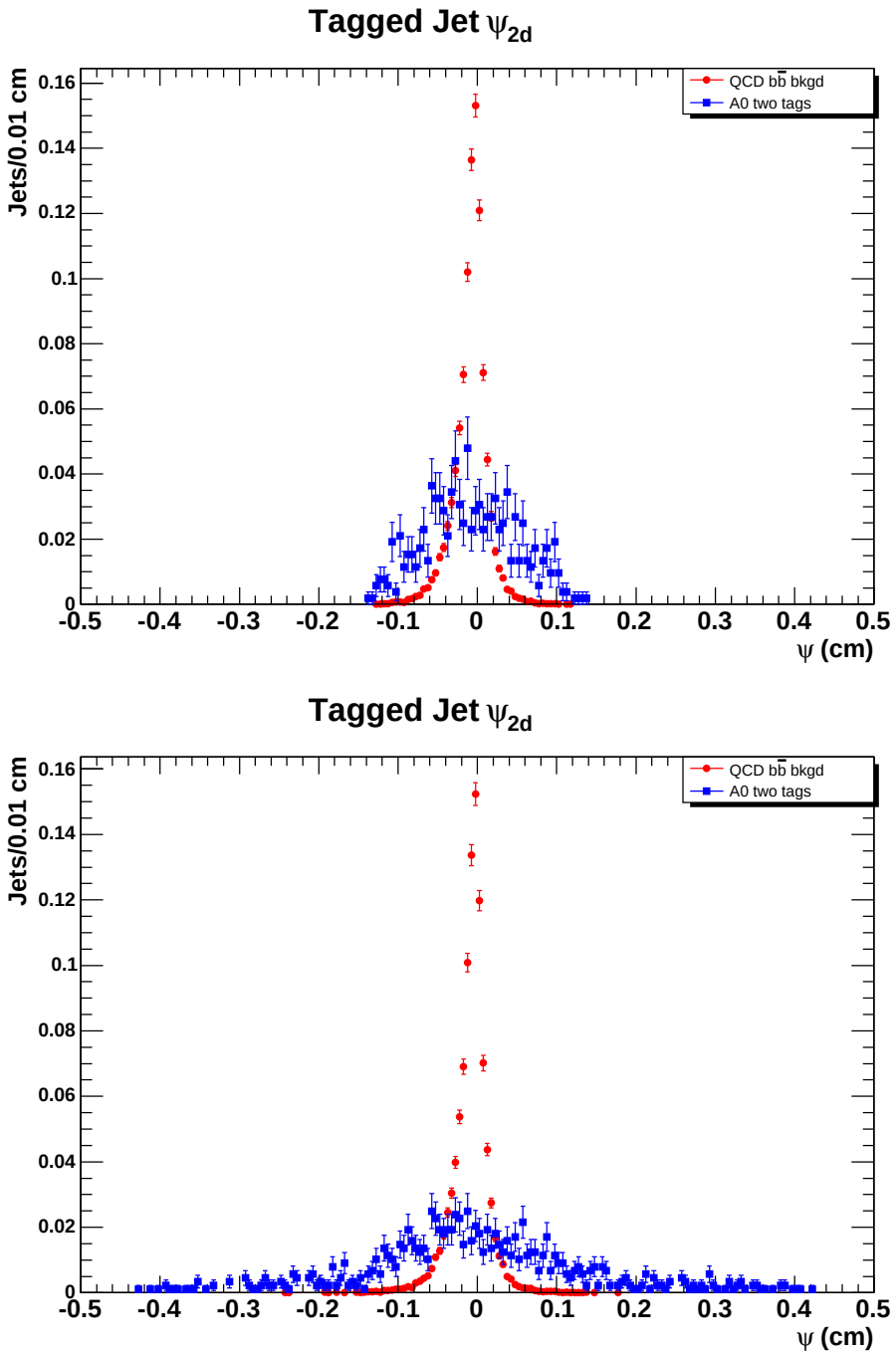

Figure 4.5: ψ for the different $|d_0|_{max}$ cuts, $|d_0|_{max} < 0.15$ cm (top) and $|d_0|_{max} < 0.45$ cm (bottom). Distributions are normalized to unit area.

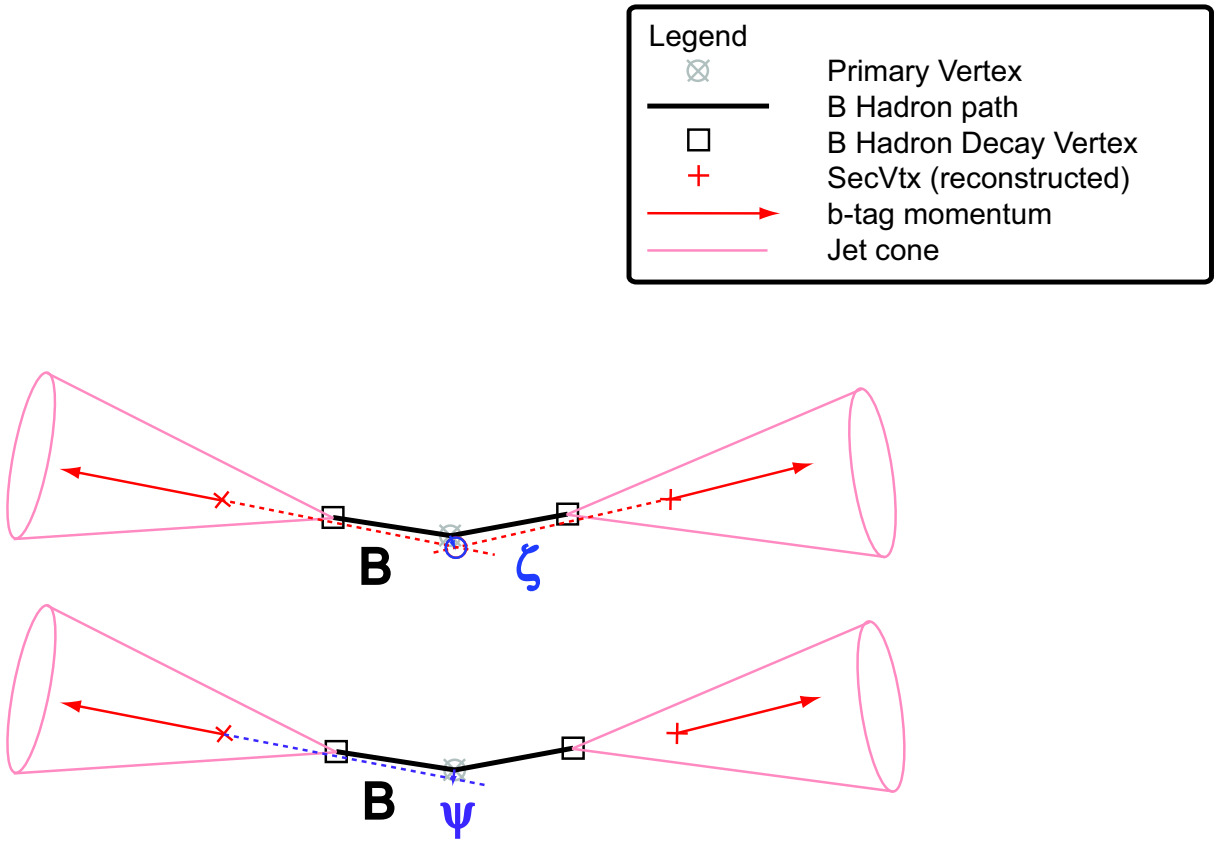

Figure 4.6: Schematic diagram of variables ζ (top) and ψ (bottom) for typical background events.

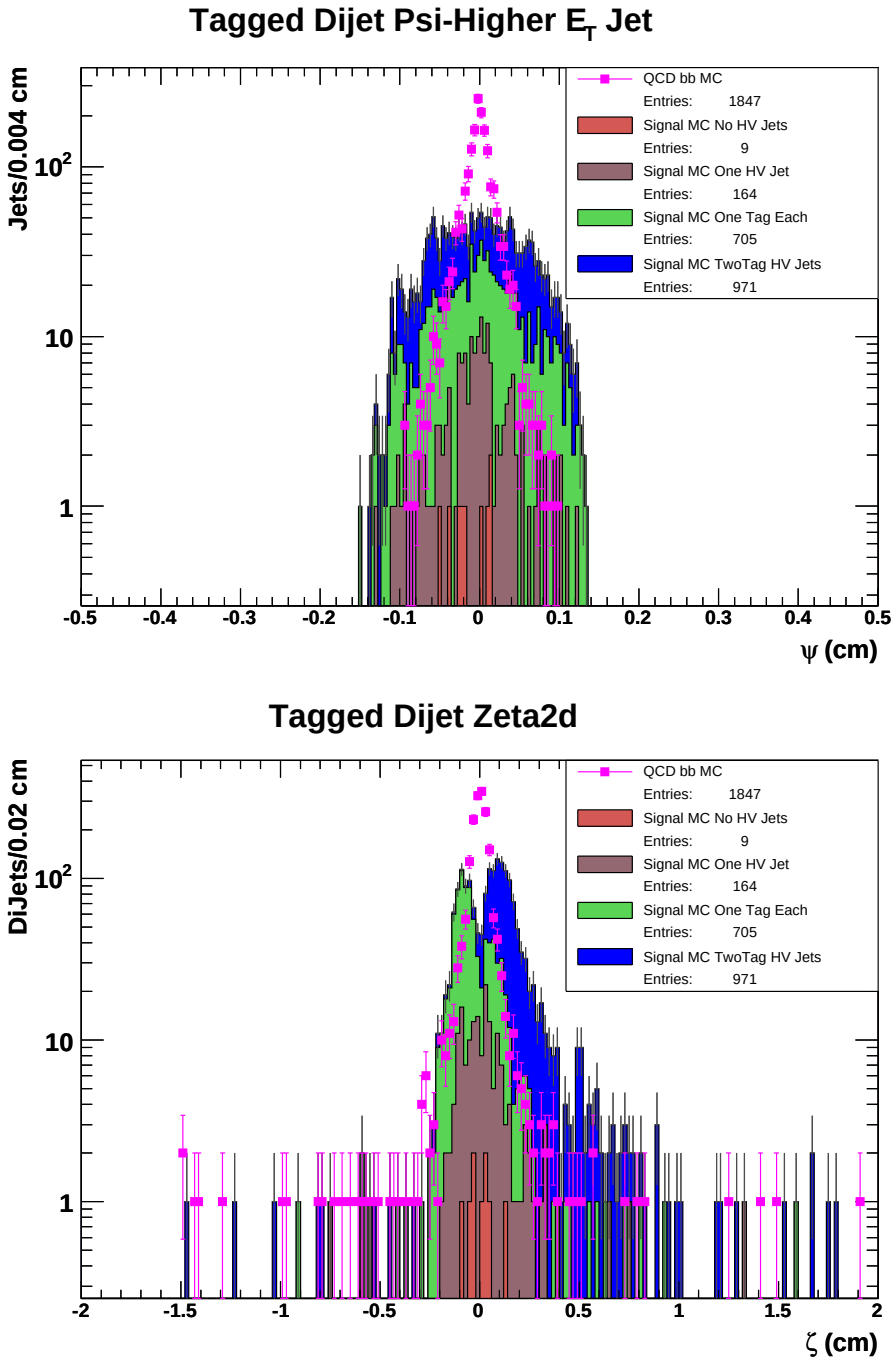

Figure 4.7: ψ (top) and ζ (bottom) distributions for the default $|d_0|_{max}$ cut of 0.15 cm. The signal MC histograms are stacked.

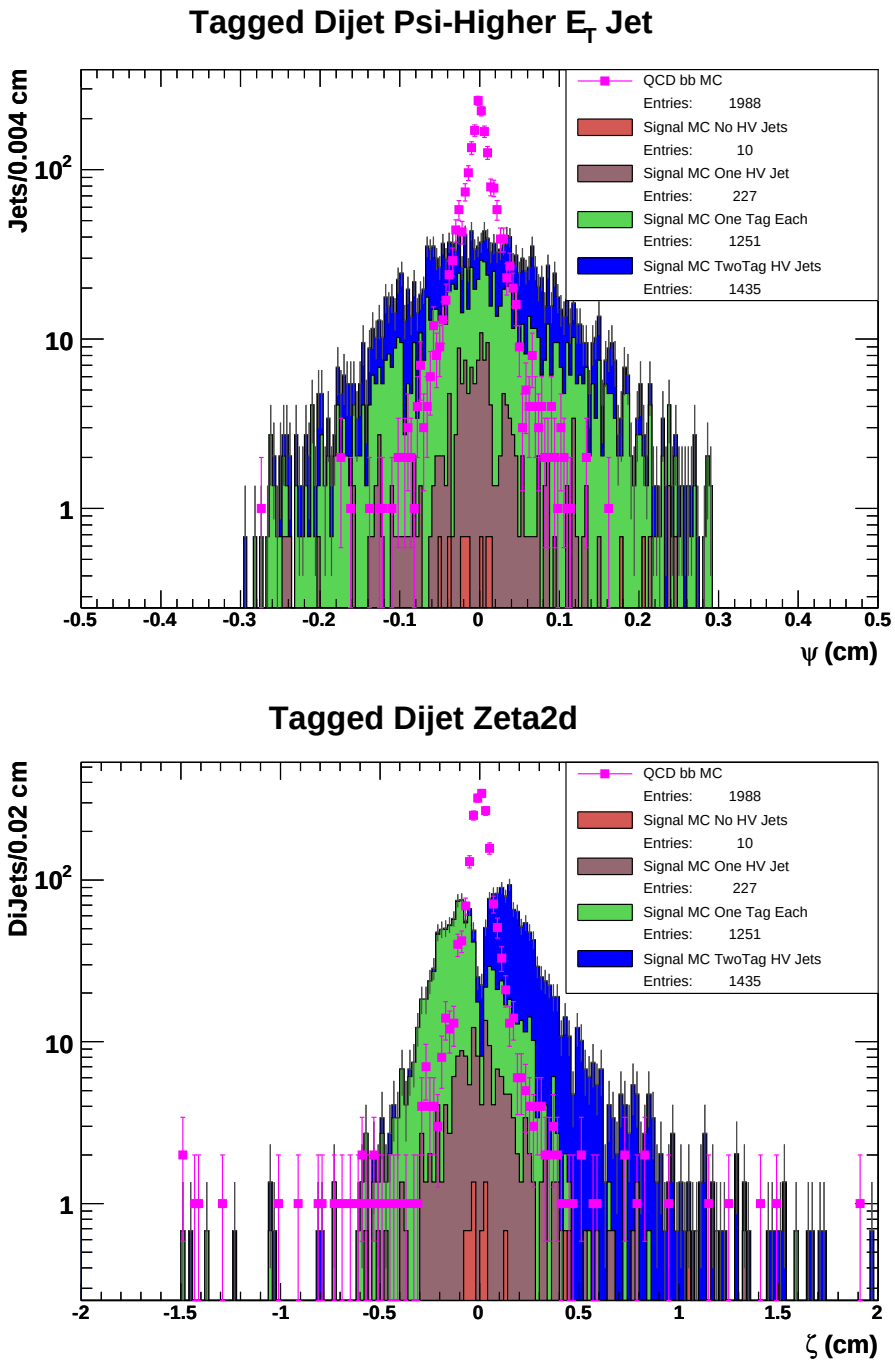

Figure 4.8: ψ (top) and ζ (bottom) distributions for $|d_0|_{max}$ cut of 0.30 cm. The signal MC histograms are stacked.

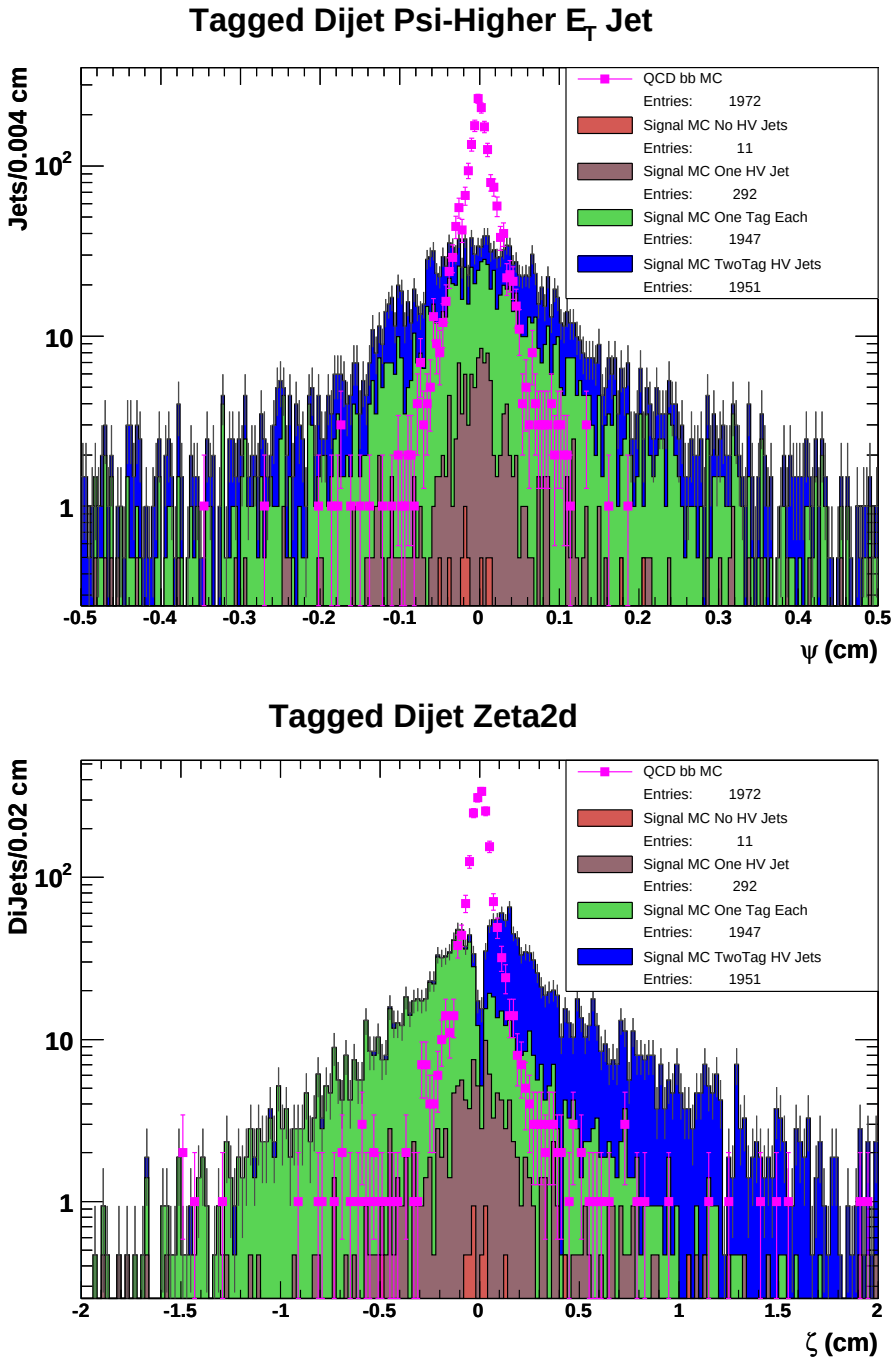

Figure 4.9: ψ (top) and ζ (bottom) distributions for $|d_0|_{max}$ cut of 1.5 cm. The signal MC histograms are stacked.

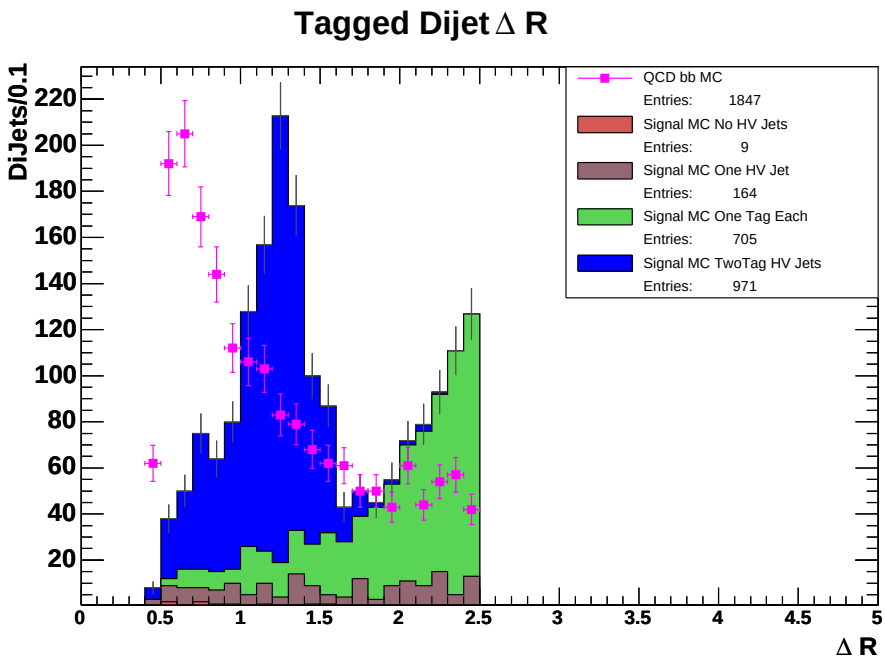

Figure 4.10: ΔR distributions for the default $|d_0|_{max}$ cut of 0.15 cm. The signal MC histograms are stacked. Here a $\Delta R < 2.5$ cut has already been applied. This cut is described in more detail in Section 4.3.2.

4.3 Event Selection

4.3.1 Good Run Lists

Good Run Lists (GRL) are used at CDF in order to select data where the detector and trigger components are known to be operating correctly. Different analyses use different components of the detector, and thus the GRL are logical ANDs and ORs of the status of these subdetectors. Some subdetector components, e.g., the calorimeters, are required to be good for all analyses. For example, this analysis requires the SVX II silicon tracker and generally does not use the ShowerMax (electron) detectors at CDF. Thus the silicon detector bit is turned on in the GRLs and the ShowerMax detector is turned off.

CDF provides default good run lists that generally have three bits: silicon detector(s), ShowerMax (electron) detector(s), and muon detector(s). However, in this analysis, because we use the ZBB trigger, we also demanded that an additional SVT GRL bit be set to true. As a result custom Good Run Lists are generated using a default CDF prescription and used for this analysis. In general we do not require the ShowerMax detector bit or muon detector bit, except for one data trigger where both are required. Thus the "default" Good Run List for this analysis is a combination of the silicon and SVT bits, while a silicon, SVT, muon, and electron bit GRLs is generated for the MUON_CMUP8 trigger used to construct p.d.f.s. Table 4.3 shows the different GRLs used for this analysis.

Trigger/MC	**Good Run Lists**
ZBB	Silicon bit and SVT bit `TRUE`
JET triggers	Silicon bit and SVT bit `TRUE`
HV Signal MC	Silicon bit and SVT bit `TRUE`
Pythia QCD dijet MC	Silicon bit and SVT bit `TRUE`
MUON_CMUP8	Silicon bit, ShowerMax bit, Muon bit ignoring bad CMX, and SVT bit `TRUE`

Table 4.3: Custom Good Run Lists used in this analysis.

4.3.2 Signal and Control Regions

While the Hidden Valley model predicts four jets in the final state, we allow events with three jets in order to increase our acceptance. In addition, the plug-jet veto in the ZBB trigger at Level-2 reduces jet multiplicity (while simultaneously lowering the trigger rate at high luminosity). Thus in order to maintain acceptance the signal region is defined with three or more tight-central jets.

The MC studies in Section 4.2.2 show that the opening angle between the two jets is not back-to-back, but instead usually smaller. The effect of a lighter HV particle is more co-linear decay daughters, i.e., jets. Thus for each dijet pair in a 3-or-more jet event, we apply a cut of $\Delta R < 2.5$ on each pair. Events which pass the jet multiplicity cut and have a dijet pair passing the ΔR cut are said be in the signal region. Later, ΔR will be used to further optimize the signal search, but for now the cut is meant to separate signal like events from the large QCD background. A major source of this QCD background is dijet events, many of which have back-to-back pairs of jets. In Fig. 4.11 there also exists a peak of events with smaller ΔR. These are mostly due to gluon radiation.

In addition to the signal region, a two-jet control region is defined as follows. Events are required to have exactly two jets (again with $E_T^{L5} > 20$ GeV) and a third jet with $E_T^{uncorr} < 15$ GeV. There is no ΔR requirement on the two jets in this sample. Because we demand a low energy third jet a large majority of these events will be back-to-back, which is seen in Fig. 4.11. The purpose of this control region is to allow us to test our background estimation technique on a set of events that is devoid of signal. By comparing the background estimate to the real events in the control region, we can make a statement as to the validity of the technique without biasing ourselves if any signal happens to be present.

Table 4.4 show the cuts made to define both the signal and control regions.

Region	**Selection Cuts**
Control	2 $E_T^{L5} > 20$ GeV, $\|\eta\| < 1.0$ jets
	3rd jet $E_T^{uncorr} < 15$ GeV
Signal	3 or more $E_T^{L5} > 20$ GeV, $\|\eta\| < 1.0$ jets
	with one jet pair having $\Delta R < 2.5$

Table 4.4: Definition of the control and signal regions.

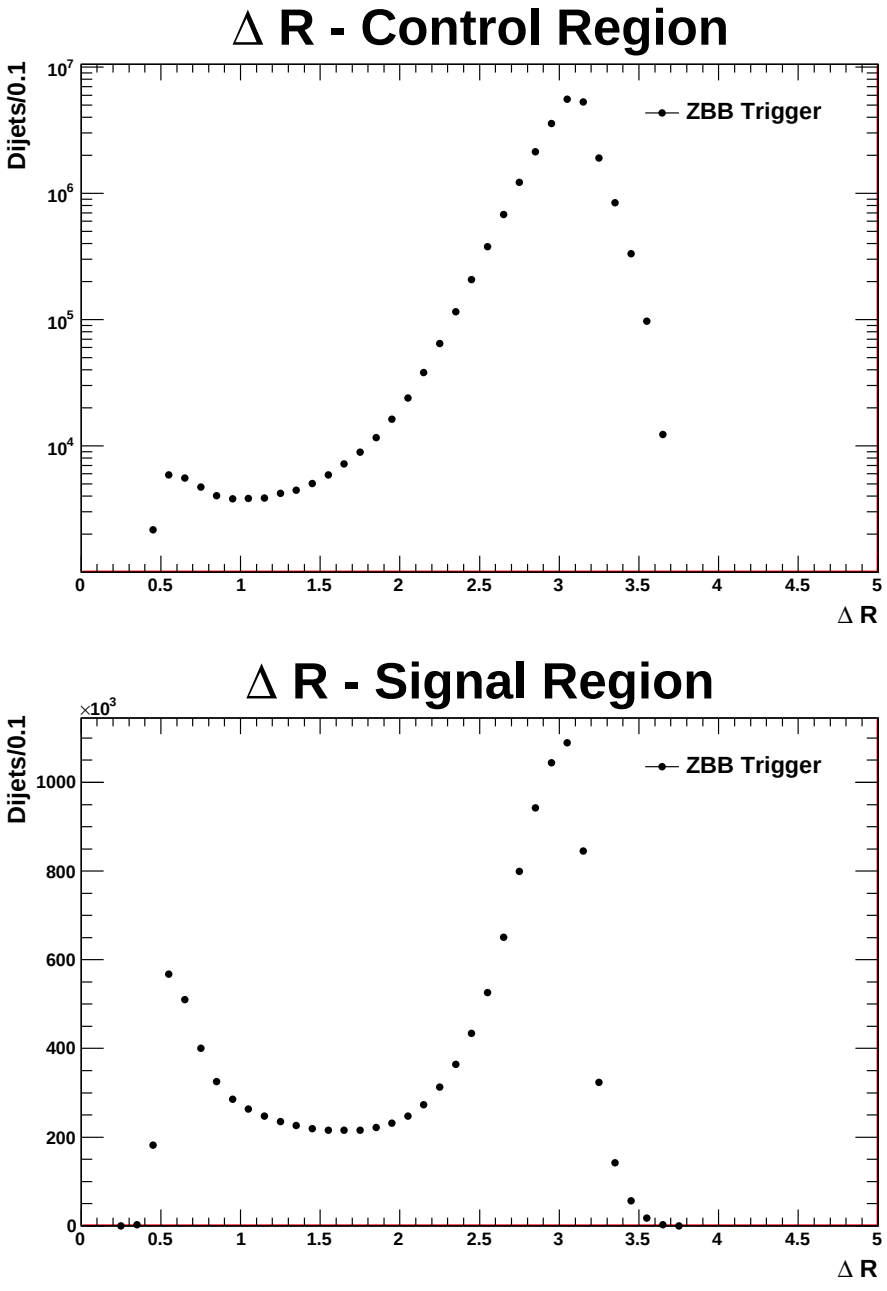

Figure 4.11: ΔR distributions of the ZBB trigger data; n.b. the control region (top) is plotted on a log scale, while the signal region (bottom) is not. The ΔR cut has not been applied to these data.

4.4 Secondary Vertex Tagging

4.4.1 Introduction

Identifying b-quark jets is an important part of many CDF measurements. SecVtx is the most commonly used b-jet tagger (or b tagger). It is used in top-quark mass measurements as well as many searches for new physics. While SecVtx is a powerful tool it does have its limitations. Generally data recorded at CDF are reconstructed into Production-level data, and then Ntupled for analysis. Since SecVtx is a Production-level module, if users wish to adjust a parameter of SecVtx they must reprocess and re-Ntuple the data.

Stntuple Secondary Vertex Finder (TStnSVF) is a program that is designed to perform b-tagging but with data in STNTUPLE format. STNTUPLES are smaller and faster to process than Production-level data. TStnSVF is designed to perform the same general algorithm as SecVtx. It also features nearly all of the input parameters that SecVtx uses, and allows the user to adjust these parameters.

Many of the details of this program can be found in the CDF Note 9689 describing TStnSVF [58]. The salient features are presented here.

4.4.2 Description

TStnSVF is a port of SecVtx for the STNTUPLE. A full description of SecVtx is available elsewhere [59] [60]; here we present a basic outline. Tracks and jets from the STNTUPLE are required as inputs to the program. In addition a primary vertex and its error matrix are required (more on this later).

TStnSVF has four distinct steps:

1. Associate tracks with jets

2. Remove K_Ss and Λs

3. Select tracks for vertexing

4. Create a secondary vertex from selected tracks

Figure 4.12 shows a flowchart outlining the basic algorithm of TStnSVF.

TStnSVF only considers jets which, by default, have $E_T^{uncorr} > 10.0$ GeV and $|\eta| < 2.4$. These cuts, and nearly all the cuts described below are adjustable. The default parameters are known as tight-level cuts (or operating point), which are identical to the tight-level cuts in SecVtx.

The first step is to find all the tracks within the ΔR cone of a jet. The cone-size is an adjustable parameter (defaults to 0.4).

After associating tracks to a jet, the program attempts to fit pairs of tracks to see if they originated from a K_S or Λ decay. If so, they are removed from vertexing consideration.

The program selects which tracks in a jet are Good, Pass1, and/or Pass2, each having more stringent track requirements. Tracks are selected based on multiple quantities: $\mathrm{p_T}$, $|d_0|_{max}$, Δz_0 with respect to the primary vertex, d_0 significance ($S_{d_0} = d_0/\sigma_{d_0}$), and silicon layers hit. All the parameters are listed with their cut values in Table 4.5.

Good tracks are defined without the S_{d_0} requirement. Pass1 tracks are Good tracks with an additional S_{d_0} cut. Pass2 tracks have more stringent S_{d_0} and $\mathrm{p_T}$ cuts. Each definition is a subset of the previous; thus all Pass2 tracks are automatically Pass1 and Good tracks. These definitions are in place because there are two different vertexing strategies, Pass1 and Pass2, which use their respective sets of tracks.

Pass1 vertexing begins by attempting to fit a seed vertex with pairs of Pass1 tracks using the CTVMFT fitting routine. A seed vertex must pass a cut on the chi-squared of the fit in order continue. Afterwards, additional Pass1 tracks are attached to this vertex if their S_{d_0} with respect to the seed vertex passes an S_{d_0} attachment cut. A vertex

containing at least three tracks is considered a candidate vertex.

If no Pass1 candidate vertex can be found then the program executes the Pass2 vertexing strategy. Here all Pass2 tracks are simultaneously fit. As long as the fit succeeds, a candidate vertex is formed.

In either case the candidate vertex is then pruned of tracks that contribute the most to the chi-squared of the fit. Pruning continues until the track with the largest chi-squared contribution has a chi-squared smaller than a parameter track chi-squared cut, or until the number of tracks drops to three (two for Pass2 vertexing).

Now the vertex is subjected to a final battery of cuts and tests to determine if it is in fact a secondary vertex. These cuts include: a final chi-squared cut on the vertex, L_{2d}, L_{2d} significance, pseudo $c\tau$, a final test for K_Ss and Λ decays, and a series of material vetoes to make sure the vertex did not come from an interaction with detector material. After all these cuts, a vertex is declared found, and the jet is considered b tagged.

L_{2d} is defined as the two-dimensional distance from the primary vertex to the secondary vertex (L_{xy}) projected onto the two-dimensional jet momentum vector. If this projection's direction is in the same hemisphere of the detector as the p_T of the jet, L_{2d} is considered positive and the b tag value is $+1$. If the direction is in the opposite hemisphere then L_{2d} is negative and the b tag value is -1. Thus a jet can be positively or negatively b tagged. These negative b tags are useful in understanding the fraction of light flavor jets that have been positively mistagged.

There are some inherent differences between the two b taggers. SecVtx is designed to run over Production-level data while TStnSVF runs over STNTUPLE data. While the two are the same to first order, there are some second order differences. One difference is that some data are not available at the Ntuple-level, for instance the Silicon database which helps determine the quality of individual hits. Another difference is what is termed "resolution effects" where a variable falls on either side of a cut value. For instance the

S_{d_0} of a track in Production-level data may be 3.51 while in STNTUPLE may be 3.49. If the cut is $S_{d_0} > 3.5$, then one track will pass while the other will fail.

A final difference is that SecVtx fits its own primary vertex. Instead TStnSVF uses previously calculated vertices. It finds the best (class 12) primary vertex in the ZVERTEX block, call it the seed vertex, and then finds the closest primary vertex in the PRIMEVTX block to this seed vertex. This procedure mimics SecVtx which takes the highest quality ZVERTEX vertex and attempts to fit a new primary vertex constraining the result to the beamline. There are rare times when TStnSVF and SecVtx do not agree on the primary vertex for the event, which will impact the vertexing results.

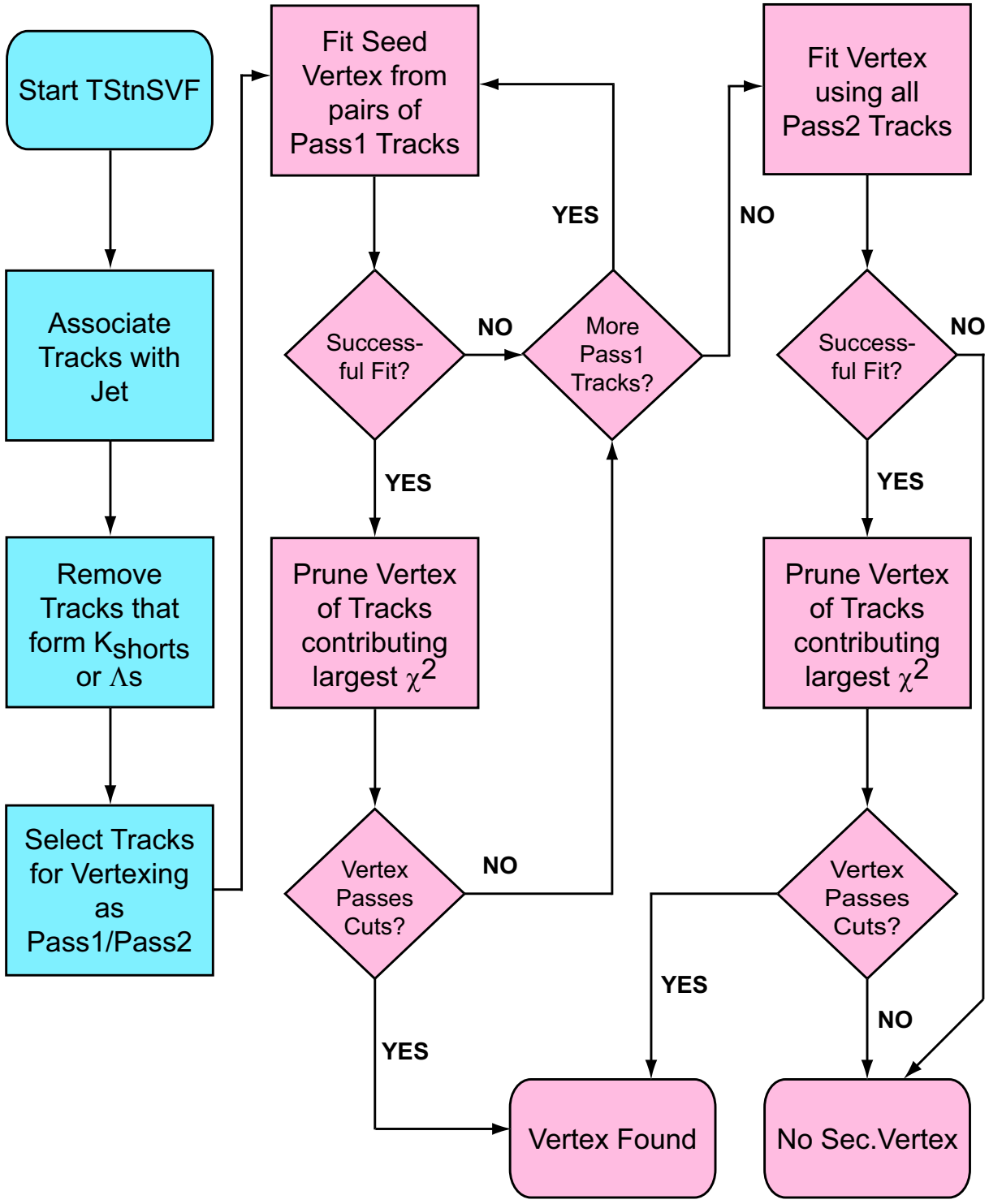

Figure 4.12: Flowchart of the TStnSVF algorithm.

Variable		Tight		Loose		Ultratight	
		Pass1	Pass2	Pass1	Pass2	Pass1	Pass2
Jet E_T^{uncorr} (GeV)	$>$	10.0		10.0		10.0	
Jet $\|\eta\|$	$<$	2.4		2.4		2.4	
Track Jet ΔR	$\leq$	0.4		0.4		0.4	
Track Type [a]		no standalone		no standalone		no standalone	
Track p_T (GeV)	$>$	0.5	1.0	0.5	1.0	0.5	1.0
Track d_0 (cm)	$<$	0.15		0.15		0.15	
Track Δz_0 (cm)	$<$	2.0		2.0		2.0	
Track χ^2/Si layers hit $r-\phi$	$<$	8.0		8.0		8.0	
Track Si layers hits $r-\phi$	$\geq$	3		3		3	
OR Track Si hits $r-\phi$ [b]	$\geq$	4		4		4	
Track d_0 Sig.	$>$	2.0	3.5	2.0	3.0	3.5	
Min N_{tracks} for vertexing	$\leq$	3	2	3	2	3	10^7 [c]
K_Ss and Λ (lifetime) fit χ^2	$<$	50.0		50.0		50.0	
≥ 1 Track with p_T (GeV)	$>$	1.0	1.5	1.0	1.5	1.0	-
Seed Vertex χ^2 [d]	$<$	50.0	-	50.0	-	50.0	-
Attachment d_0 Sig.[d]	$<$	4.0	-	6.0	-	4.0	-
Track Prune χ^2 [e]	$>$	45.0	30.0	90.0	10,000.0	45.0	-
Vertex fit χ^2	$<$	50.0		120.0	2,000.0	50.0	
Vertex Radius (cm) [f]	$<$	2.5		2.5		2.5	
Vertex $c\tau$ (cm)	$<$	1.0		1.0		1.0	
Vertex L_{2d} (cm)	$<$	5.0		5.0		5.0	
Vertex L_{2d} Sig.	$>$	7.5		6.0		7.5	
Material Removal		yes		no		yes	

Table 4.5: Jet, track, and vertex cuts used in TStnSVF. Tight, loose, and ultratight-level parameter cuts/operating points are listed. All these parameters are adjustable.

a. Tracks with track algorithms 2, 16, and 21 are ignored.

b. This condition is ORed with the AND of the two requirements above.

c. This has the effect of turning off Pass2 vertexing.

d. Only used for Pass1 vertexing.

e. Tracks with χ^2 greater than this value are pruned from the vertex.

f. Vertex Radius is only used for vertices with only two tracks.

4.4.3 B-tagger Comparison

We performed three validation analyses: a Mistag Matrix (MM) analysis, a B-Tagging Scale Factor (BTSF) analysis, and a Mistag Asymmetry analysis (MAsym). The purpose of these analyses is two-fold. First is to verify that TStnSVF behaves as expected, without any erratic behavior. The second is to compare the results from TStnSVF to SecVtx. While the two b taggers have their differences as described above, their basic algorithms are the same and thus they should give comparable results.

For all three of these analyses we only processed data from periods 0 through 8. In addition, we only performed the analyses for tight-level parameter cuts and without considering the systematic uncertainties that will have to be applied to real analyses that use b tagging.

Only the results are shown here; for more detail see CDF Note 9689 [58].

Mistag Matrix

The mistag matrix analysis is performed the same as previous SecVtx mistag matrix analyses [61] [62]. A mistag matrix object is a 6-dimensional histogram that records the positive and negative tag rates (for any tagger) as a function of 6 different variables: jet E_T, jet η, number of good tracks in the jet, sum E_T in the event, number of primary vertices, and the primary vertex Z position [61]. A good track is defined in the same way as SecVtx: it must have certain p_T, silicon, d_0 and z_0 requirements, but with no d_0 significance requirement.

Mistag matrices are built using the four jet trigger samples JET_20, JET_50, JET_70, and JET_100; data from periods 0 through 8. This data period is chosen because it is well understood. Table 4.6 summarizes the different datasets used for the mistag matrix analysis.

Trigger	Run Range				
	138425 -186598	190697 -203799	203819 -206989	206990 -212133	217990 -222426
JET_20	gjt1ad	gjt1ah	gjt1ai	gjt1bi	gjt1ci
JET_50	gjt2ad	gjt2ah	gjt2ai	gjt2bi	gjt2ci
JET_70	gjt3ad	gjt3ah	gjt3ai	gjt3bi	gjt3ci
JET_100	gjt4ad	gjt4ah	gjt4ai	gjt4bi	gjt4ci

Table 4.6: `Stntuple` datasets used for mistag matrix analysis.

These data are Ntupled with Gen6 STNTUPLE. We only considered runs defined by the default good run list requiring good silicon, muon (ignoring bad CMX), and ShowerMax runs. (For these validation analyses we use the default GRLs and not our custom ones discussed in Section 4.3.1.) Data from JET_20 and JET_50 are corrected due to the different dynamic prescale present in early run periods.

The mistag matrix analysis uses SecVtx to form a mistag matrix using all events in the jet samples. Then using TStnSVF over the same events we observe the tag rates for positive and negative jets. This is compared to the rates as predicted from a SecVtx mistag matrix. We should note that the mistag matrix is not actually used in the analysis itself, but is presented here as a check of the TStnSVF b-tagging algorithm.

Table 4.7 shows the results of the comparison between the two b taggers. The overall result is that TStnSVF is a little lower in efficiency than SecVtx, a difference we believe is due to the differences between the b taggers described previously.

Histograms are made showing the trend of the tag rates and the ratio for six variables, including variables that are parameterized in the mistag matrix, and additional variables that are not parameterized such as run number and instantaneous luminosity. These histograms are shown in Fig. 4.13 to 4.18. The first three are parameters in the mistag matrix, while the second three are not. The first case shows some discrepancies in E_T and η. However, for the displaced vertex analysis, we are only concerned with jets in the

Tag Rate	**JET_20**	**JET_50**	**JET_70**	**JET_100**	**All JET**
Observed Positive	0.015735± 0.000026	0.028399± 0.000044	0.033248± 0.000044	0.039850± 0.000041	0.029281± 0.000013
Predicted Positive	0.0160523± 0.0000038	0.0298120± 0.0000091	0.0350573± 0.0000095	0.0420448± 0.0000097	0.0307033± 0.0000040
Ratio	0.9802± 0.0016	0.9526± 0.0015	0.9484± 0.0013	0.94780± 0.00099	**0.95366± 0.00043**
Observed Negative	0.003230± 0.000012	0.008145± 0.000024	0.010590± 0.000025	0.014715± 0.000025	0.0092419± 0.0000071
Predicted Negative	0.0031548± 0.0000011	0.0084059± 0.0000035	0.0111379± 0.0000037	0.0154184± 0.0000045	0.0096047± 0.0000017
Ratio	1.0239± 0.0037	0.9689± 0.0029	0.9508± 0.0023	0.9544± 0.0016	**0.96222± 0.00076**

Table 4.7: Tag rates and ratios for the b-tagger comparison analysis. The overall tag rate ratio for all jet samples is presented in **bold** text.

central region where the ratio is flat. In addition, the jet E_T of the ZBB trigger sample is primarily between 25 GeV and 90 GeV; where the ratio is flatter.

In the second case, i.e., the variables not parameterized by the mistag matrix, the ratios are fairly consistant with 0.95, although they also show some minor discrepancies. Overall these graphs show that the TStnSVF b-tagging algorithm does not behave in a pathologically different way than the SecVtx algorithm.

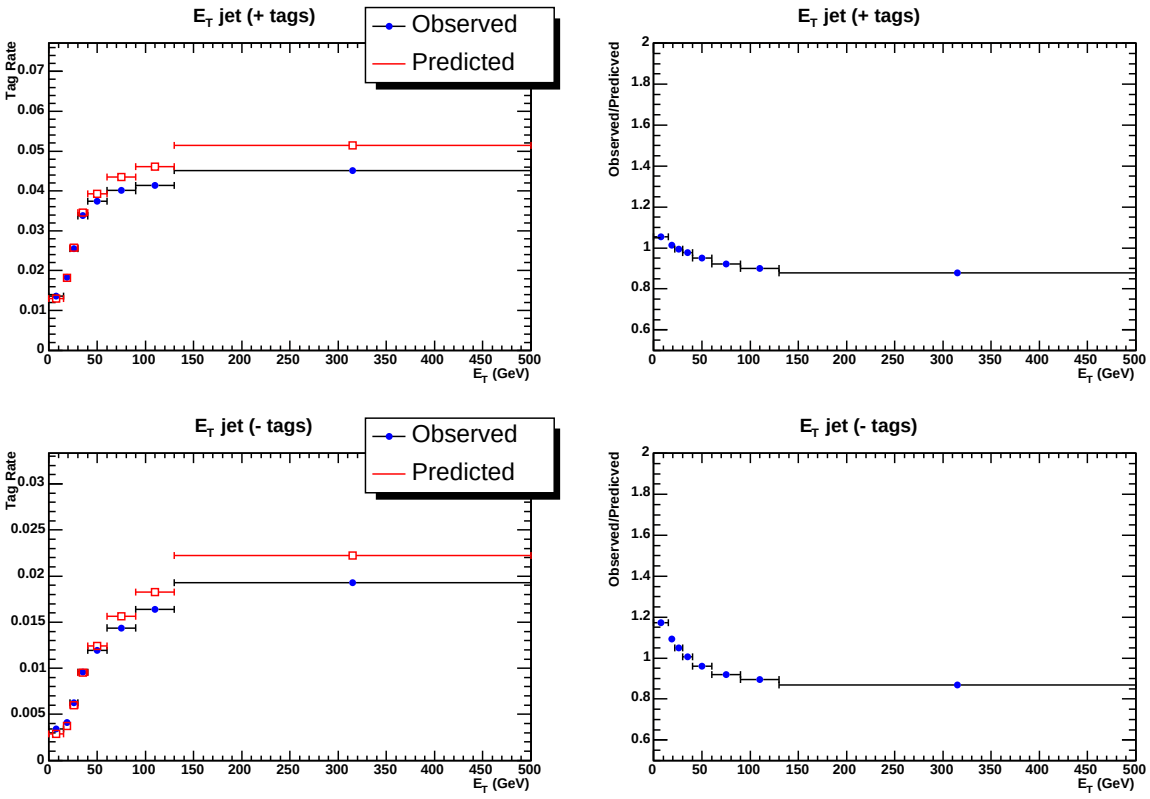

Figure 4.13: Mistag Matrix b-tagger comparison analysis tag rates and ratios vs. E_T. The observed tag rates come from TStnSVF, and the predicted tag rates are from a matrix defined with SecVtx.

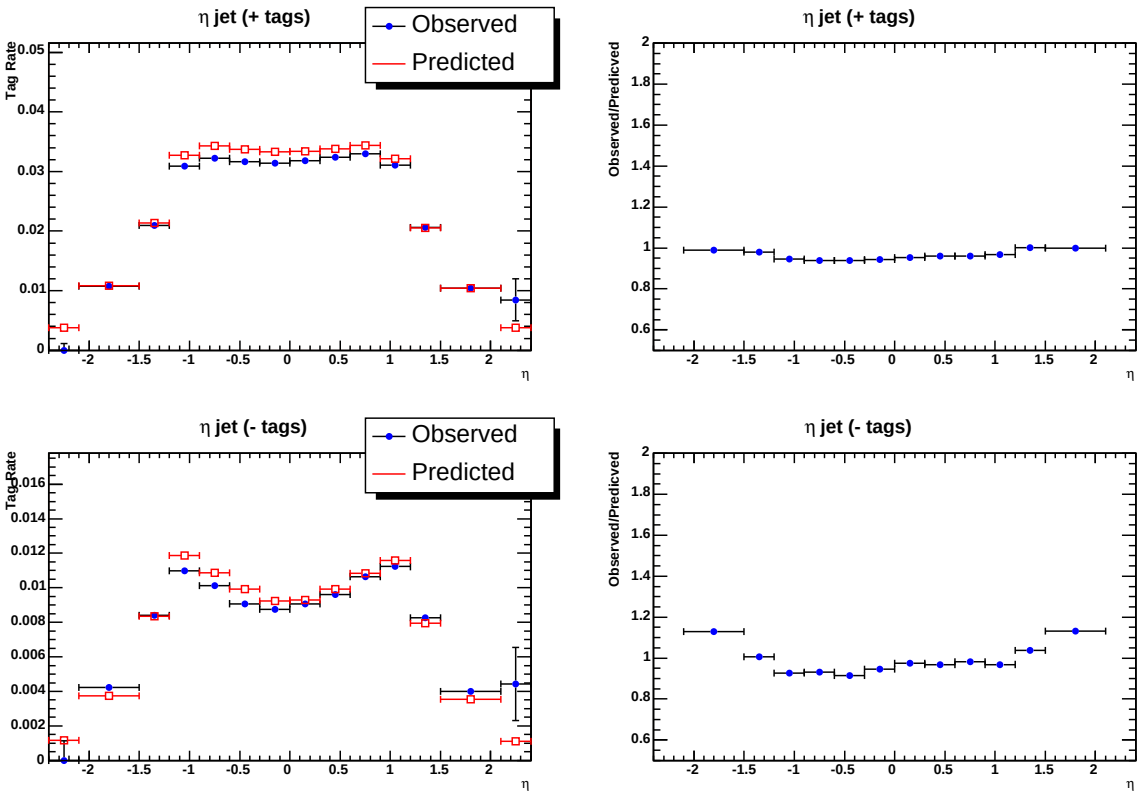

Figure 4.14: Mistag Matrix b-tagger comparison analysis tag rates and ratios vs. η. The observed tag rates come from TStnSVF. The predicted tag rates are from a matrix defined with SecVtx.

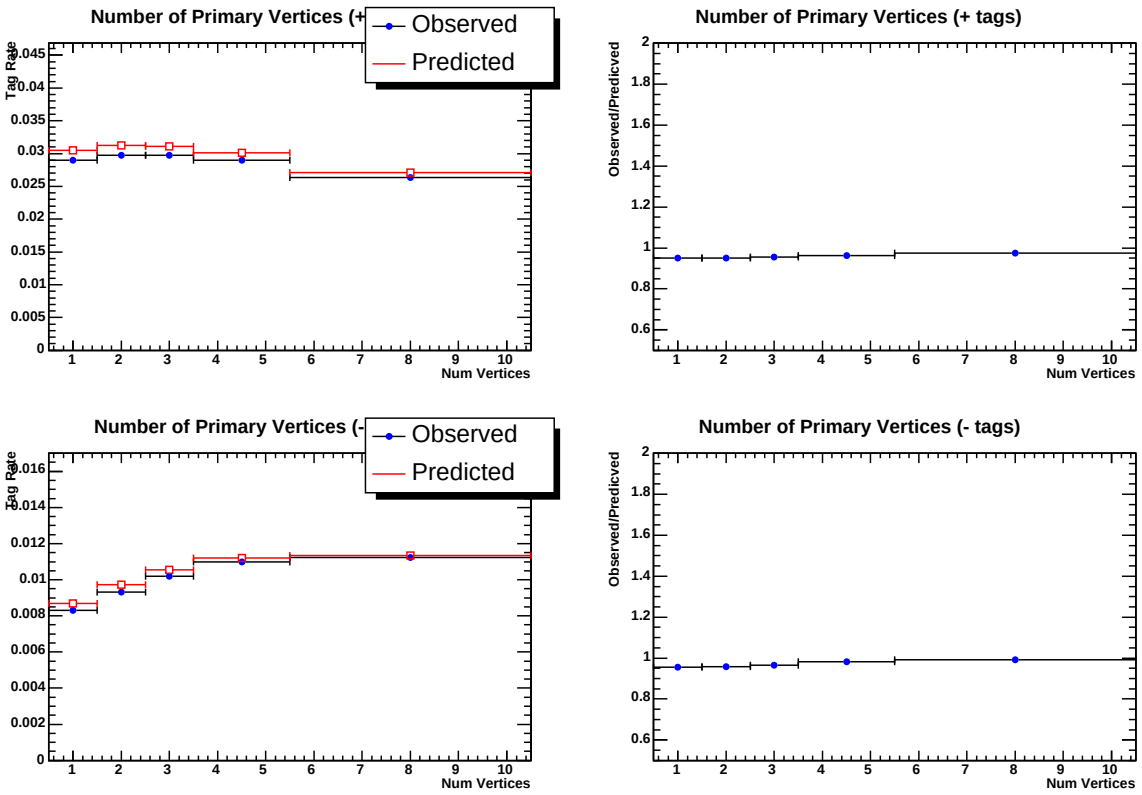

Figure 4.15: Mistag Matrix b-tagger comparison analysis tag rates and ratios vs. $N_{Prim.\ Vtx}$. The observed tag rates come from TStnSVF. The predicted tag rates are from a matrix defined with SecVtx.

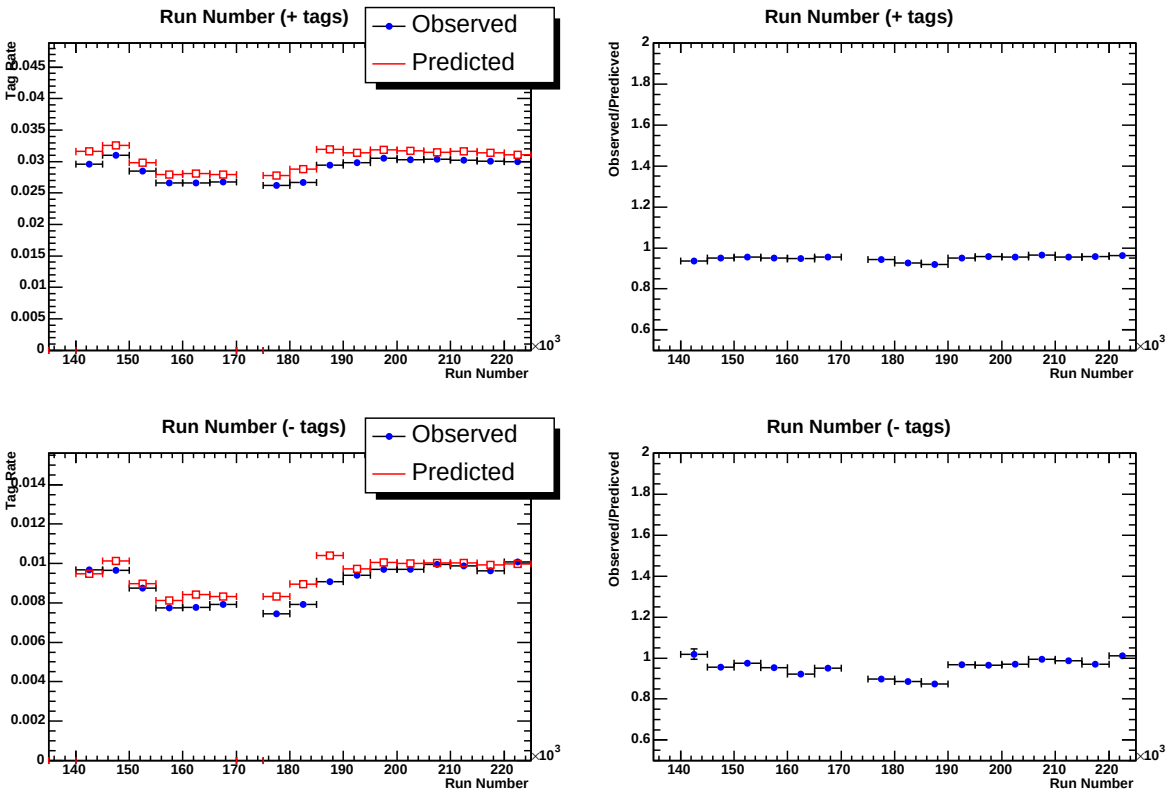

Figure 4.16: Mistag Matrix b-tagger comparison analysis tag rates and ratios by run number. The observed tag rates come from TStnSVF. The predicted tag rates are from a matrix defined with SecVtx.

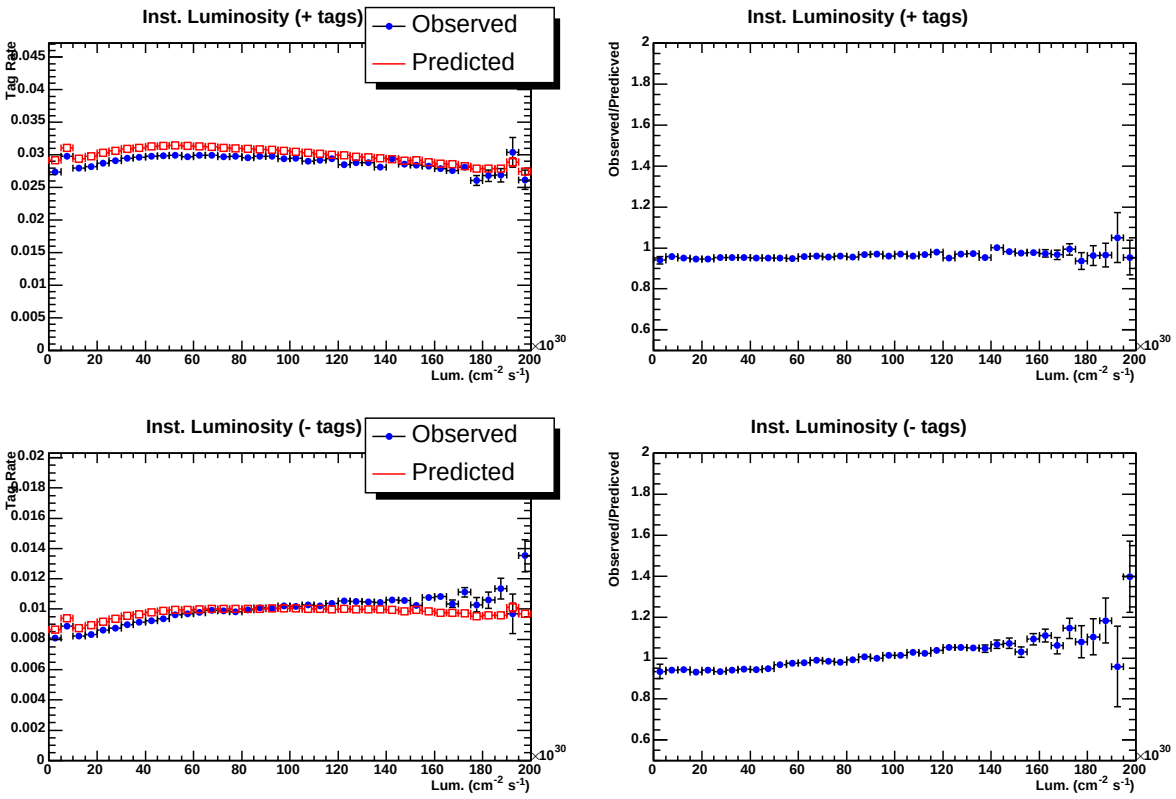

Figure 4.17: Mistag Matrix b-tagger comparison analysis tag rates and ratios vs. instantaneous luminosity. The observed tag rates come from TStnSVF. The predicted tag rates are from a matrix defined with SecVtx.

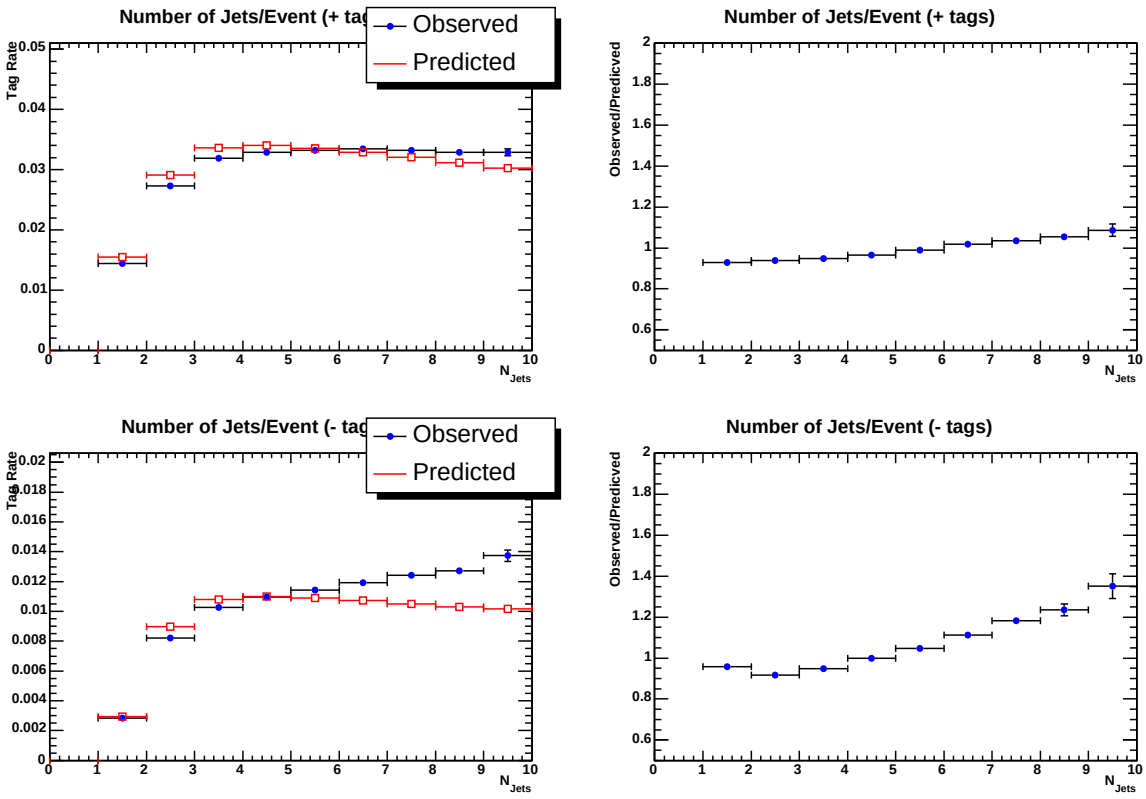

Figure 4.18: Mistag Matrix b-tagger comparison analysis tag rates and ratios vs. N_{jets} per event. The observed tag rates come from TStnSVF. The predicted tag rates are from a matrix defined with SecVtx.

B-Tagging Scale Factor

The B-Tagging Scale Factor (BTSF) is a measurement of the efficiency of the b tagger in data divided by the efficiency of the b tagger in MC. Calculating the efficiency in MC is straightforward, we can divide the number of tagged b jets in the MC by the number of total b jets in the MC. These quantities are known because we have the HEPG information for MC.

For the data, the efficiency is more difficult. We know the number of tagged jets but not the number of tagged b jets. We need to determine how many of the former in the data sample came from a b quark. We have MC which can help us extract this number.

The analysis consists of looking at dijet pairs, where one jet contains a muon (muon-jet) and the other is tagged with the loose tagger (away-jet). The $p_{T,rel}$ between the muon and the jet is used as the primary variable in this analysis. This variable is different for b-quark jets and non b-quark jets. B-quark and non b-quark templates are constructed using this variable. The data is fitted using ROOT's TFractionFitter to determine the fraction of muon-jets in the data, both tagged and untagged, produced by a b quark. From this we can determine the efficiency in data. More information of the technique of this analysis, including the cuts on the muon and away jets, can be found in CDF Note 8640 [63].

This analysis is done for both TStnSVF and SecVtx b-taggers; and for both the tight and loose-level parameter cuts because the away-jet requires a loose tag. The TStnSVF BTSF result will be eventually used as a systematic uncertainty for the displaced vertex analysis.

Table 4.8 shows the datasets we use for this analysis. The data comes from the muon calibration trigger (MUON_CMUP8). There are two sources of MC, Pythia QCD dijet with electron(muon) production, and regular Pythia QCD dijet. From the data and MC,

Trigger	Run Range		
	138425 -186598	190697 -203799	203819 -222426
MUON_CMUP8	`bmclad`	`bmclah`	`bmclai`
Pythia dijet $p_T > 20$, w/ $e(\mu)$	`bt0sla`		
Pythia dijet $p_T > 18$	`bt0sqb`		
Pythia dijet $p_T > 40$	`bt0srb`		

Table 4.8: Data and MC datasets for the b-tagging scale factor analysis.

one b-quark template (from `bt0sla`) and four non-b templates are constructed.

1. c-quark non-b templates from `bt0sla`
2. light flavor non-b templates from `bt0s[qr]b`
3. muon anti-match in data; where the muon CMU ΔX and CMP ΔX cuts are inverted.
4. zero Pass1 tracks from data; the muon-jet has no Pass1 tracks

These data are processed with StNtuple Gen6. We require that runs in the data are part of the GRL requring good silicon, muon (ignoring bad CMX) and ShowerMax detectors, while runs in the MC are part of the GRL requiring only the silicon and ShowerMax bits. Because MUON_CMUP8 is dynamically prescaled, we weight the events in data by their dynamic prescale value for the given run section.

For the data and b templates, muon-jets are separated into those with positive tags and those without a positive tag (i.e., negative or no tag). For all non-b templates, all muon-jets are used due to statistical limitations.

Each fit is performed with a b template and one non-b template. Thus there are four independent fits. From this fit we can extract the b and non-b fraction from the data. With those fractions we can calculate the efficiency using each of the non-b templates as a separate measurement.

Table 4.9 shows the results for TStnSVF and SecVtx for tight-level cuts. The four measurements of the data efficiency are used to calculate the BTSF. The weighted mean of these SF are calculated for the data efficiency and shown in the table. The first uncertainty on the SF is the weighted standard devitation of the four measurements. The second uncertainty in the table is the RMS of each of the four measurements w.r.t. the average result. There is good agreement between TStnSVF and SecVtx.

	TStnSVF Tight	**SecVtx Tight**
Data Efficiency, charm template	0.3722 ± 0.0054	0.3919 ± 0.0055
Data Efficiency, light flavor	0.3798 ± 0.0067	0.3988 ± 0.0069
Data Efficiency, anti-muon match	0.3706 ± 0.0053	0.3910 ± 0.0053
Data Efficiency, zero Pass1 tracks	0.3872 ± 0.0058	0.4084 ± 0.0059
Average Data B-Tagging Efficiency	$0.3768 \pm 0.0028 \pm 0.0067$	$0.3969 \pm 0.0029 \pm 0.0070$
MC B-Tagging Efficiency	0.4041 ± 0.0032	0.4221 ± 0.0032
B-Tagging Scale Factor	$0.932 \pm 0.022 \pm 0.026$	$0.940 \pm 0.020 \pm 0.025$

Table 4.9: Data and MC b-tagging efficiencies, and b-tagging scale factors for the TStnSVF and SecVtx b-taggers, tight-level cuts.

Mistag Asymmetry

In an ideal world, only heavy jets (b or c quarks) would be positively tagged, while only light quark jets would have negative tags. But light quarks sometimes are tagged with a positive tag and heavy quarks can decay near the beamline with resolution effects producing a negative tag. In general a mistag is a light quark jet that has a positive tag. It is important to understand the mis-measurement of these light quark jets because they can contribute to the overall error of any measurement. Mistags can arise from limited detector resolution, long-lived light particles such as K_Ss or Λs, or interactions in the beampipe or detector material. If resolution effects are the only source of mistags, then it would be possible to use the negative tag distribution as a model for positive mistags. (Negative tags are secondary vertices where the vertex's displacement vector and the jet's momentum vector point in opposite directions in two-dimensions.) However, other effects contribute to the mistag asymmetry and contribute more positive tagged light-flavor jets.

In order to determine the heavy-flavor content of the generic jet tag rate the mistag asymmetry is derived. This analysis is based on CDF Notes 8626 [64] and 9277 [65]. This parameter is applied as a correction to the mistag matrix (MM). The MM can give the negative tag rate. But not all of these negative tags are from light quarks. The negative tag rate can be defined as:

$$R^-_{mistag} = \frac{N^-_{light} + N^-_{heavy}}{N^{pre}_{light} + N^{pre}_{heavy}}. \tag{4.1}$$

The "pre" sample refers to the jets that are fiducial to the b tagger, $E_T > 10$ GeVand $|\eta| < 2.4$.

Two corrections, α and β are used to correct R^-_{mistag}. They are defined as:

$$\alpha = \frac{N^+_{light}}{N^-_{light} + N^-_{heavy}} \tag{4.2}$$

$$\beta = \frac{N_{light}^{pre} + N_{heavy}^{pre}}{N_{light}^{pre}} \tag{4.3}$$

where α corrects the numerator while beta corrects the denominator. The result of $\alpha\beta R_{mistag}^{-}$ is the number of positive tagged light jets divided by the total number of fiducial (pre) light jets, or the mistag rate. Like the mistag matrix analysis, these results are not directly used in the displaced vertex analysis, but again used to check that the TStnSVF b tagger is performing similarly to the SecVtx algorithm.

The data used to determine the mistag asymmetry is the same data used to calculate the MM. The four jet trigger samples JET_20, etc. are used for the data distributions. These data are required to be included in the GRL identical to the MM analysis. Table 4.10 shows the data and MC datasets used for this analysis.

For the MC, four Pythia QCD dijet samples are used. Because the four MC datasets' p_T do not match with the real data's E_T, we weight the MC in order to mimic the E_T distribution of the data jet trigger samples. This is done by smearing the leading jet E_T with a Gaussian turn-on at 5 GeV below the jet sample trigger threshold with a 5 GeV width. For example QCD $\hat{p_T} > 90$ GeV MC jets, which correspond to JET_100 data jets, would have a Gaussian peak at 95 GeV with a width of 5 GeVas shown in Fig. 4.19. ($\hat{p_T}$ is defined as $\sqrt{tu/s}$ where s, t, and u are the Mandelstam variables associated with the QCD $q\overline{q}$process.) Table 4.11 shows the different Gaussian means for different MC datasets.

After processing, all four data datasets are combined into one large sample, and then split again into four different E_T bins. α and β depend on the number of heavy flavor jets which in turn is dependent upon E_T. Thus α and β are calculated for each of these four E_T bins. These bins mostly correspond to the E_T bins of the MMs. The bins are: 10-22, 22-40, 40-60, and 60-1000 GeV.

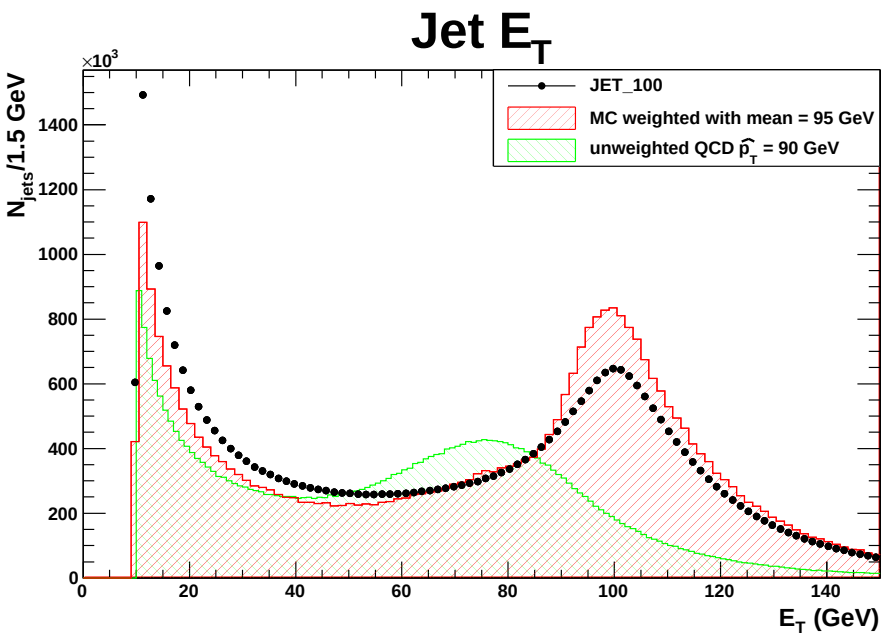

Figure 4.19: JET_100 data and QCD $\hat{p_T} > 90$ GeV MC (red) with the latter being weighted with a Gaussian with $\mu = 95$ GeV and $\sigma = 5$ GeV. An unweighted distribution (green) is also included for comparison.

The MC is split into E_T bins in a similar fashion. In addition, the MC is weighted with the relative tag fractions from the corresponding data jet dataset. For example, given the QCD $\hat{p_T} > 40$ GeV MC, the number of tagged jets in its corresponding data, JET_50, for each of the E_T bins is calculated. The number of tagged jets is divided by the total number of tagged jets across all E_T bins to calculate the relative fraction of tagged jets for each E_T bin. Returning to QCD $\hat{p_T} > 40$ GeV MC, each E_T bin is now scaled to have the same relative fraction of tagged jets as the JET_50 data sample.

The method involves fitting distributions of MC templates from bottom, charm and light quark jets to extract the heavy flavor fraction of positive and negative tagged data jets, more details are available in Ref. [64]. The fit is performed on the tag excess, the difference between the positive and negative tagged samples. The fitted variable in this case is the signed tag vertex mass (the invariant mass of the secondary vertex's tracks).

Trigger	**Run Range**				
	138425 -186598	190697 -203799	203819 -206989	206990 -212133	217990 -222426
JET_20	gjt1ad	gjt1ah	gjt1ai	gjt1bi	gjt1ci
JET_50	gjt2ad	gjt2ah	gjt2ai	gjt2bi	gjt2ci
JET_70	gjt3ad	gjt3ah	gjt3ai	gjt3bi	gjt3ci
JET_100	gjt4ad	gjt4ah	gjt4ai	gjt4bi	gjt4ci
Pythia dijet $p_T > 18$	bt0sqb				
Pythia dijet $p_T > 40$	bt0srb				
Pythia dijet $p_T > 60$	bt0ssb				
Pythia dijet $p_T > 90$	bt0stb				

Table 4.10: `Stntuple` datasets used for mistag asymmetry analysis.

Data/MC	Data leading Jet E_TGeV	MC leading jet E_TGeV	Gaussian mean (GeV)
JET_20/bt0sqb	20	18	15
JET_50/bt0srb	50	40	45
JET_70/bt0ssb	70	60	65
JET_100/bt0stb	100	90	95

Table 4.11: Gaussian means for corresponding data and MC datasets.

The sign is determined by the sign of the tag; thus a negative tagged jet has a negative mass and a positive tagged jet has a positive mass.

Mass templates for each of the three species of jet are collected. Then the positive tag excess is calculated for each of the three templates. These are fitted using ROOT's TFractionFitter to the tag excess in the data.

These MC fit fraction are used to determine the number of b, c, and light quark jets from the data distribution. This tells us the number of light quarks that have a positive tag which is used to calculate α. The denominator for α is just the number of negative tagged light and heavy jets in data.

The calculation of β is determined by the number fiducial (pre-tag) jets which are heavy or light. The fit fractions of bottom, charm, and light quarks from above are used

to determine how many of the total pre-tag sample come from b quarks, c-quarks or light quark jets. These fit fractions are divided by the b and c quark tagging efficiencies as calculated from the MC datasets. In order to correct for MC/data discrepancies these efficiencies are first multiplied by the B-Tagging SF where the SF for both b and c-quarks are assumed to be the same, but the charm quark Scale Factor error is doubled.

Since the total number of pre-tag jets is easily known, we subtract the calculated number of pre-tag b and c-quark jets from it, and divide that number by the total number of pre-tag jets to determine β.

Finally, α and β are multiplied together to determine the mistag asymmetry parameter which can be multiplied by R^{-}_{mistag} to determine the mistag rate. Table 4.12 and Fig. 4.20 show the results for this analysis. The result is that there is good agreement between the two b taggers.

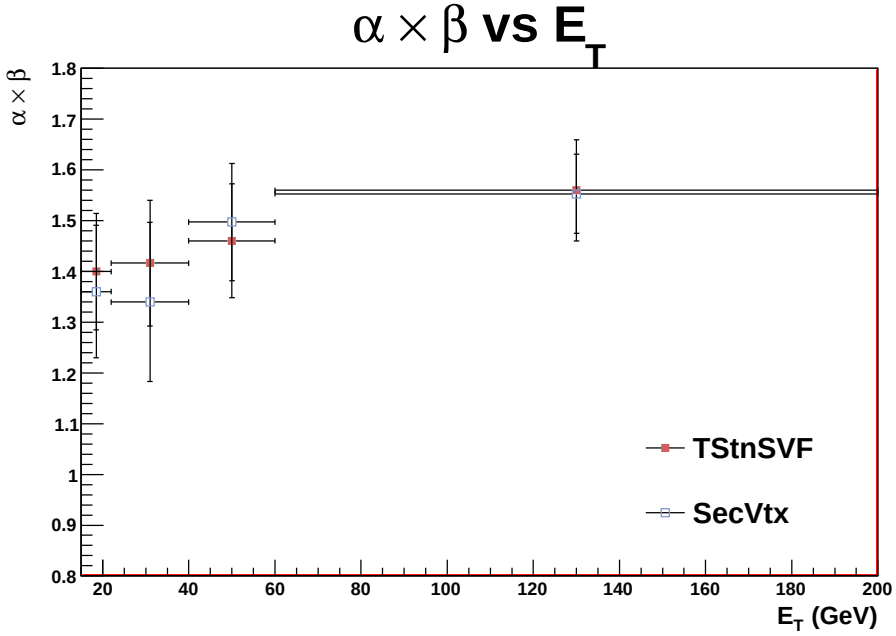

Figure 4.20: $\alpha \times \beta$ as a function of E_T for both TStnSVF and SecVtx b taggers.

TStnSVF Tight	Scale Factor		0.932 ± 0.026	
Bin Boundaries	10-22 GeV	22-40 GeV	40-60 GeV	60-1000 GeV
Num Pretag Jets	$68.2M \pm 8.3k$	$3.09M \pm 5.6k$	$20.9M \pm 4.6k$	$33.7M \pm 5.8k$
Fitted #b jets	$224k \pm 6.8k$	$220k \pm 6.6k$	$177k \pm 6.0k$	$275k \pm 13.5k$
Fitted #c jets	$115k \pm 8.3k$	$104k \pm 9.0k$	$93.8k \pm 9.8k$	$144k \pm 27.0k$
b Efficiency	0.21 ± 0.0017	0.33 ± 0.003	0.384 ± 0.0043	0.389 ± 0.0046
c Efficiency	0.04 ± 0.00045	0.0649 ± 0.00084	0.0822 ± 0.0012	0.0979 ± 0.0014
Calculated #bs	$1.15M \pm 41.4k$	$713k \pm 25.5k$	$493k \pm 19.6k$	$756k \pm 40.3k$
Calculated #cs	$3.04M \pm 275k$	$1.71M \pm 178k$	$1.22M \pm 149k$	$1.57M \pm 309k$
α	1.31 ± 0.11	1.30 ± 0.11	1.34 ± 0.10	1.40 ± 0.09
β	1.07 ± 0.000012	1.09 ± 0.00002	1.08 ± 0.000031	1.0 ± 0.000023
$\alpha \times \beta$	1.40 ± 0.15	1.42 ± 0.12	1.46 ± 0.11	1.50 ± 0.099
SecVtx Tight	Scale Factor		0.940 ± 0.025	
Bin Boundaries	10-22 GeV	22-40 GeV	40-60 GeV	60-1000 GeV
Num Pretag Jets	$68.2M \pm 8.3k$	$3.09M \pm 5.6k$	$20.9M \pm 4.6k$	$33.7M \pm 5.8k$
Fitted #b jets	$224k \pm 5.6k$	$221k \pm 7.6k$	$184k \pm 6.4k$	$303k \pm 12.0k$
Fitted #c jets	$122k \pm 7.0k$	$123k \pm 10.9k$	$95.8k \pm 10.3k$	$156k \pm 20.9k$
b Efficiency	0.21 ± 0.00173	0.34 ± 0.003	0.41 ± 0.004	0.42 ± 0.0049
c Efficiency	$0.04 \pm 4.73e^{-4}$	$0.071 \pm 8.8e^{-4}$	0.091 ± 0.0013	0.11 ± 0.0015
Calculated #bs	$1.12M \pm 34.7k$	$688k \pm 26.9k$	$481k \pm 19.2k$	$762k \pm 33.9k$
Calculated #cs	$2.98M \pm 231k$	$1.84M \pm 192k$	$1.11M \pm 136k$	$1.49M \pm 216k$
α	1.28 ± 0.12	1.23 ± 0.14	1.38 ± 0.11	1.45 ± 0.07
β	1.06 ± 0.000011	1.09 ± 0.000024	1.08 ± 0.000029	1.07 ± 0.000021
$\alpha \times \beta$	1.36 ± 0.13	1.34 ± 0.16	1.50 ± 0.12	1.55 ± 0.078

Table 4.12: Summary of results: number of jets, b/c fractions and efficiencies, and α and β for both TStnSVF and SecVtx b-taggers, tight operating point.

4.5 PDF Construction

4.5.1 Introduction

In Section 4.1.4, secondary vertex p.d.f.s were introduced. These p.d.f.s are constructed from SM secondary vertices in order to model vertices later in the analysis. Here we discuss the variables that are used to construct these p.d.f.s, their data, and in one case MC, sources, and finally the selection cuts to construct these p.d.f.s.

4.5.2 Variables

Probability density functions (p.d.f.s) are constructed from standard model secondary vertices in order to model the background. These p.d.f.s encapsulate the information of a secondary vertex, namely its position and its momentum (direction). Figure 4.21 shows the different p.d.f. variables and how they are defined. The diagram is drawn in a plane transverse to the beamline, and all variables are two-dimensional. We defined the secondary vertex's variables with respect to its parent jet's momentum vector, also called the jet axis. First, define $\vec{L_{xy}}$ as the two dimensional distance from the primary vertex to the secondary vertex. There are two components to this L_{xy} vector, one parallel to the jet axis, one perpendicular. These two components are the first two p.d.f. variables, and are named u and v respectively. (The definition of u is identical to another variable named L_{2d}, however we will refer to this variable as u for this analysis.) These two variables define the position of a secondary vertex with respect to a jet axis.

The secondary vertex has a momentum associated with it. It is defined as the sum of the transverse momentum vectors of the tracks that are used to form the vertex. The $\Delta\phi$ angle between the jet axis and this momentum vector is the third p.d.f. variable, named α. This variable defines the direction of a secondary vertex with respect to a jet axis.

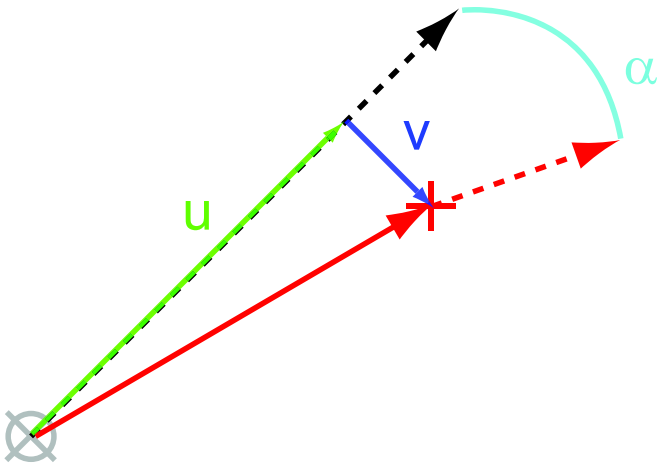

Black Dashed Line	Jet Momentum
Red Cross	Secondary Vertex
Red Solid Line	Sec Vertex L_{xy}
Red Dashed Line	Sec Vertex Momentum
Green Line (u)	Parallel component of L_{xy}
Blue Line (v)	Perp. component of L_{xy}
Cyan Arc (α)	Angle b/w the two momenta

Figure 4.21: Diagram of PDF variables. The black dashed arrow represents the jet's momentum vector. The red arrow is L_{xy}, which can be deconstructed into two vectors with respect to the jet's momentum, u and v. The momentum of the secondary vertex, the red dashed arrow, has an angular difference, α, with respect to the jet's momentum. This diagram is drawn in a plane transverse to the beamline.

4.5.3 Sources

The p.d.f.s are constructed from data sources, whenever possible, in order to encapsulate standard model secondary vertices. The different categories from which p.d.f.s are constructed are listed in Table 4.13. We split the p.d.f.s into three quark categories: b quark, c quark, and light-flavor which encompasses all other quarks as well as gluons. The p.d.f.s are also split into four different jet E_T bins to account for differences in the shape of the p.d.f.s for different energy ranges. Finally the jets are split into different bins that account for the number of SVT tracks in the jet that satisfy the ZBB trigger requirement of large impact parameter tracks. These SVT track requirements are identical to the Level-2 requirement in the ZBB trigger (Table 3.1) for a single track: an SVT track with $P_T > 2$ GeV, 160 $\mu m < |d_0| < 1000$ μm, and $\chi^2 < 12$. The numerical requirements are zero, one, and greater than or equal to two. These categories were chosen because the trigger requires either two displaced tracks in one jet or one such track in each of two jets. Throughout this document, these bins are referred to as the E_T/nSVTTRK bins.

Variable	**Bins**
quark flavor	b-quarks, c-quarks, light-flavor
jet E_T(GeV)	[20, 30), [30, 70), [70, 110), [110, 200)
number SVT tracks	0, 1, $\geq$2

Table 4.13: Different bins for the SM secondary vertex p.d.f.s

These data are stored in three-dimensional histograms, one for each E_T/nSVTTRK bin, a total of 36 three-dimensional histograms. We find that correlations exist among all three variables; see Section 4.5.4. Although the correlations between u and the other two variables are weak, we found that constructing secondary-vertex information (pseudo secondary vertices) from these p.d.f.s does not work well unless all correlations are present. In order to find a $|d_0|_{max}$ cut that maximizes our signal sensitivity, we have run the TStnSVF b tagger 20 times, each for a slightly different $|d_0|_{max}$ cut. Each $|d_0|_{max}$ cut

results in a slightly different set of secondary vertices, thus a set of 36 three-dimensional p.d.f.s is constructed for each $|d_0|_{max}$ cut used by b tagger.

Different data sources are used to construct these p.d.f.s. Table 4.14 shows the datasets and MC used to construct the different quark flavors. In addition, the MC is used to perform other tasks, namely heavy flavor subtraction, which is discussed later. We use the MUON_CMUP8 trigger to construct b-quark p.d.f.s because the data is rich in heavy flavor. For the light-flavor p.d.f.s, we use the various JET triggers which collect a large amount of QCD multi-jet production. Finally, for the c-quark p.d.f.s we are not able to use data because there is no dedicated charm trigger. As a result we turned to the Pythia QCD dijet MC. Although the MC has limitations, (after all we are trying to avoid using MC in order to have data-driven backgrounds) we find that the overall contribution from charm quarks to this analysis is small. This is borne out in more detail in Section 4.6.3 where the flavor composition of jets in the ZBB sample is discussed. In addition, we attempt to rectify some of the data, MC differences in the p.d.f.s' shapes with the use of a scale factor. This is discussed later in Section 4.5.3.

b-quark p.d.f.s

Heavy flavor jets for the b-quark p.d.f.s are constructed from data collected with the MUON_CMUP8 trigger. This 8 GeV muon trigger collects muon data, which contains B hadrons that decay semi-leptonically. We can take advantage of the fact that the jet will contain a lepton. The method used to select these semi-leptonic B decays is nearly identical to selecting events for the BTSF analysis, see CDF Note 8640 [63]. Lepton-jet/away-jet select cuts are outlined in Table 4.15. The selection cuts require two positive b-tagged jets (using the TStnSVF b tagger) where a muon is present in one jet, the lepton-jet. Most of the variables are self-explanatory and unchanged from the b-tagging scale factor (BTSF) analysis. Since the muon-jet is expected to be a semi-leptonic B hadron

Trigger	**Run Range**							
	138425 -186598	190697 -203799	203819 -206989	206990 -212133	217990 -222426	233133 -246231	252836 -261005	261119 -277511
MUON_CMUP8	bmclad	bmclah	bmclai			bmclaj	bmclak	bmclam
SINGLETOWER5	gjs0ad	gjs0ah	gjs0ai	gjs0bi		gjs0bj	gjs0bk	gjs0bm
JET_20	gjt1ad	gjt1ah	gjt1ai	gjt1bi	gjt1ci	gjt1bj	gjt1bk	gjt1bm
JET_50	gjt2ad	gjt2ah	gjt2ai	gjt2bi	gjt2ci	gjt2bj	gjt2bk	gjt2bm
JET_70	gjt3ad	gjt3ah	gjt3ai	gjt3bi	gjt3ci	gjt3bj	gjt3bk	gjt3bm
JET_100	gjt4ad	gjt4ah	gjt4ai	gjt4bi	gjt4ci	gjt4bj	gjt4bk	gjt4bm
MC	**Run Range**							
	141572 -222529			222529 -237795			141572 -237795	
Pythia dijet $\hat{p_T} > 18$	bt0sqb			bq0sqc				
Pythia dijet $\hat{p_T} > 40$	bt0srb			bq0src				
Pythia dijet $\hat{p_T} > 60$	bt0ssb			bq0ssc			bt0ssd	
Pythia dijet $\hat{p_T} > 90$	bt0stb			bq0stc			bt0snd	

Table 4.14: Triggers and datasets used for the SM secondary vertex p.d.f.s.

decay, the jet's muon-corrected E_T accounts for the fact that the muon deposits very little of its energy in the calorimeter, resulting in the jet having low E_T. However, the BTSF analysis requires the away-jet to have a loose tag, satisfy a lower E_T requirement and larger η range. Here we demand that the away-jet have a tight-level tag and also pass the requirements to form a tight-central jet.

The away-jet is used to construct the b-quark p.d.f.s. The secondary vertex data, along with the jet momentum direction, are used to calculate u, v, and α. This is also different than the BTSF analysis where the lepton-jet is used as the primary jet of interest. While a fraction of the away-jets will decay semi-leptonically, by construction all of the lepton-jets will be semi-leptonic decays. We chose the away-jet because secondary vertices from semi-leptonic decays are different than secondary vertices from generic B hadron decays.

Finally, there are two more general differences between this heavy flavor selection algorithm and the BTSF algorithm. The first is that the latter weights each event by its trigger prescale value. Since the shape of the b-quark p.d.f. is the quantity of interest and not the rates, we did not implement this weighting. Secondly the good run list used to select events is different. See Section 4.3.1 for further details.

c-quark p.d.f.s

Charm quark jets are not readily identifiable in real data. Therefore we turn to MC in order to collect jets for the c-quark p.d.f.s. Pythia QCD dijet MC in Table 4.14 are used to construct these p.d.f.s. Events are selected with a modified Good Run List which incorporates both good silicon runs as well as runs with good SVT; see Section 4.3.1. In addition, the MC run number must satisfy a "good SVT beam line" condition, where the beam position is well known. The reason for this is due to an effect in the trigger simulation.

The SVT uses the beam line information as well as the origins of each silicon barrel

Variable	**Selection Cuts**	
muon & lepton-jet		
muon z_0 (cm)	$<$	60.0
muonΔz_0 w.r.t. jet (cm)	$<$	5.0
CMU ΔX (cm)	$<$	3.0
CMX ΔX (cm)	$<$	5.0
muon η	$<$	0.6
muon isolation	$>$	0.1
muon p_T (GeV)	$>$	9.0
muon ΔR w.r.t. jet	$<$	0.4
jet E_T L5 corrected (GeV)	$>$	9.0
jet muon-corrected E_T (GeV)	$>$	20.0
away-jet		
jet E_T L5 corrected (GeV)	$>$	20.0
jet η	$<$	1.0
jet $\Delta\phi$ w.r.t. muon-jet	$>$	2.0

Table 4.15: Selection criteria for the lepton-jet/away-jet used in construction of the b-quark p.d.f.s

to calculate the impact parameter of a track. The MC generator and detector simulation does not know where the beam line lies. This information must be calculated when the trigger is simulated. Unfortunately, this must be done manually for earlier runs as the beam line is not correctly calculated. The calculation requires that SVT beam line as well as barrel origin information is present for a particular run, hence the requirement that MC runs have good SVT beam line.

Because the MC has been generated with a specific $\hat{p_T}$, the shape of the E_T distribution of jets has a turn-on. In order to account for this we select events in which the highest E_T jet has an E_T larger than the $\hat{p_T}$ of the sample in question. This E_T is shown in Table 4.16. This is a low E_T cut on the MC jet sample.

Jets from different MC samples, with different $\hat{p_T}$ are used to construct these c-quark p.d.f.s. In order to properly combine these MC sets we normalize each MC such that the Level-5 corrected jet E_T of the combined sample is smoothly falling. In order to make this

process easier, there is a high E_T cut on each sample so that the samples do not overlap.

Trigger	**Low E_T cut (GeV)**	**High E_T cut (GeV)**
SINGLETOWER5	20.0	30.0
JET_20	30.0	70.0
JET_50	70.0	90.0
JET_70	90.0	140.0
JET_100	140.0	200.0
MC		
Pythia dijet $\hat{p_T} > 18$	20.0	70.0
Pythia dijet $\hat{p_T} > 40$	70.0	90.0
Pythia dijet $\hat{p_T} > 60$	90.0	115.0
Pythia dijet $\hat{p_T} > 90$	115.0	200.0

Table 4.16: Low and high E_T selection for the highest E_T jet in an event.

Once events have been selected, jets are collected with an inclusive selection criteria, every positive tagged tight-central jet is used. Jets are categorized by matching with a B (or D) hadron within a $\Delta R < 0.4$ cone. If a jet matches a B hadron then it is classified as a b-quark jet. If no B hadron is present but a D hadron matches, then the jet is a c-quark jet. Finally, if neither of the two previous conditions is satisfied, the jet is classified as light-flavor. Secondary vertex data from c-quark jets are used to construct the c-quark p.d.f.s.

While we are trying to build c-quark p.d.f.s from the MC, we also construct b-quark p.d.f.s from MC and compare them to the b-quark p.d.f.s we construct from the MUON_CMUP8 data trigger using the heavy flavor selection algorithm. Some differences between the MC b-quark shapes and data b-quark shapes are present, and we presume that this difference would be present in any c-quark p.d.f.s built from this MC. We create a scale factor (data/MC) using the distributions of each p.d.f. variable, u, v, and α, to account for the differences in the b-quark p.d.f. variable shapes; see Fig. 4.22. We divide the data by the MC and use a linear fit of the result to construct a scale factor. Then this scale factor is applied to the MC in order to adjust for this difference.

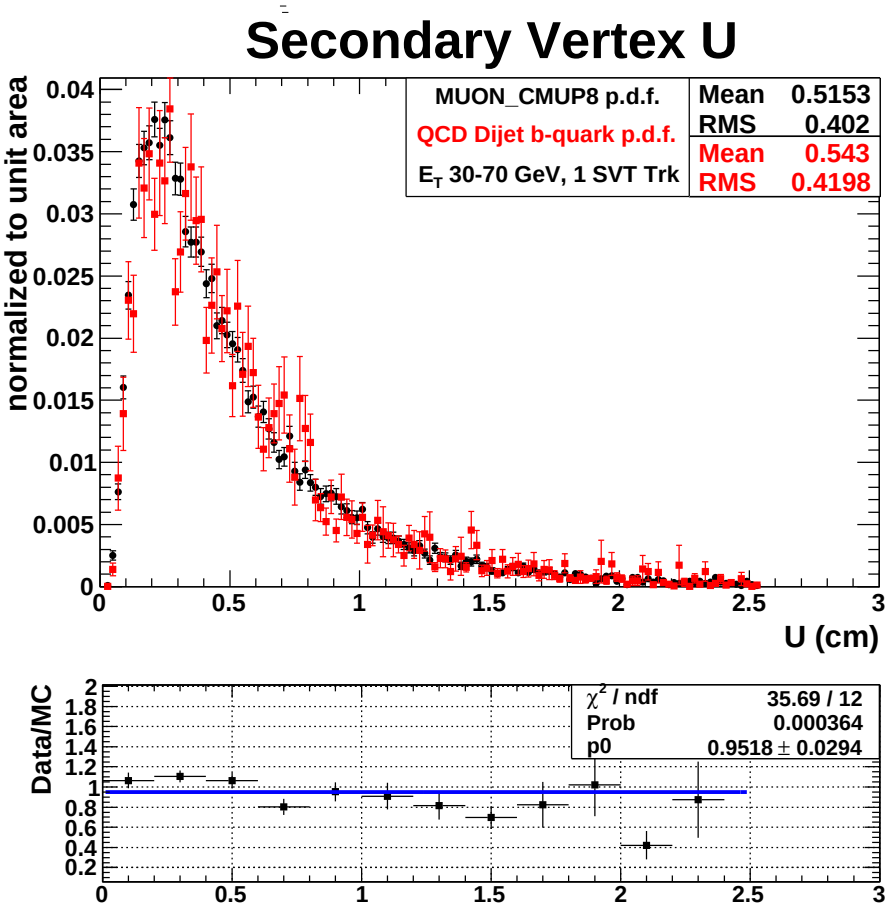

Figure 4.22: Scale Factor example for u, E_T 30 to 70 GeV with exactly 1 SVT trigger track in the jet. The data (black) is from MUON_CMPU8 and the MC (red) is QCD dijet MC. The bottom graph show the division of the two with a linear fit (blue) which is used for the scale factor.

In addition to constructing the c-quark p.d.f.s, these MC data are used to construct vertex mass templates of different quark-flavors. The vertex mass is the invariant mass of the sum of the four-momenta use to reconstruct the secondary vertex. This invariant mass has different shapes for b quark, c quark, and light-flavor jets; with the former two having generally higher vertex mass than the latter. These vertex mass distributions are used as MC templates to fit for the flavor composition of jets in data, which is discussed next.

Light flavor p.d.f.s

We construct light-flavor p.d.f.s from JET trigger data. There are five jet triggers used to collect these data; see Table 4.14. Like the MC, high and low E_T threshold cuts are used to remove effects due to trigger turn-on, at low E_T and overlap at high E_T. The resulting five datasets are merged together with the same normalization procedure as with the MC. The resulting Level-5 corrected E_T spectrum is smoothly falling.

All tight-central jets in the resulting events with positive b tags are used to construct p.d.f.s of the jet trigger data. These are not yet the light-flavor p.d.f.s because by demanding a secondary vertex be present in the jet, the jet is most likely not light-flavored, but in fact heavy flavor. Light-flavor quarks and gluon jets that have positive b tags are mistags. Thus the light-flavor p.d.f.s are actually the mistag p.d.f.s. Thus we must subtract off the heavy flavor contribution from the jet trigger p.d.f.s to construct the light-flavor p.d.f.s, i.e., heavy flavor subtraction.

In order to perform this heavy flavor subtraction we must know the flavor composition of the combined jet trigger sample. The positive b tag's track vertex mass is used. Distributions of the vertex mass are fit to the three MC templates, shown in Fig. 4.23, that are collected from the QCD dijet MC. This vertex mass fit is performed in each of the E_T/nSVTTRK bins. An example fit is shown for one of E_T/nSVTTRK bin in Fig. 4.24.

With the flavor composition of each E_T/nSVTTRK bin calculated, we subtract the b-quark and c-quark p.d.f.s from the QCD MC from the p.d.f.s collected from JET triggers (jet trigger p.d.f.s) to create the light-flavor p.d.f.s. The uncertainty in this procedure is taken into account as a systematic uncertainty.

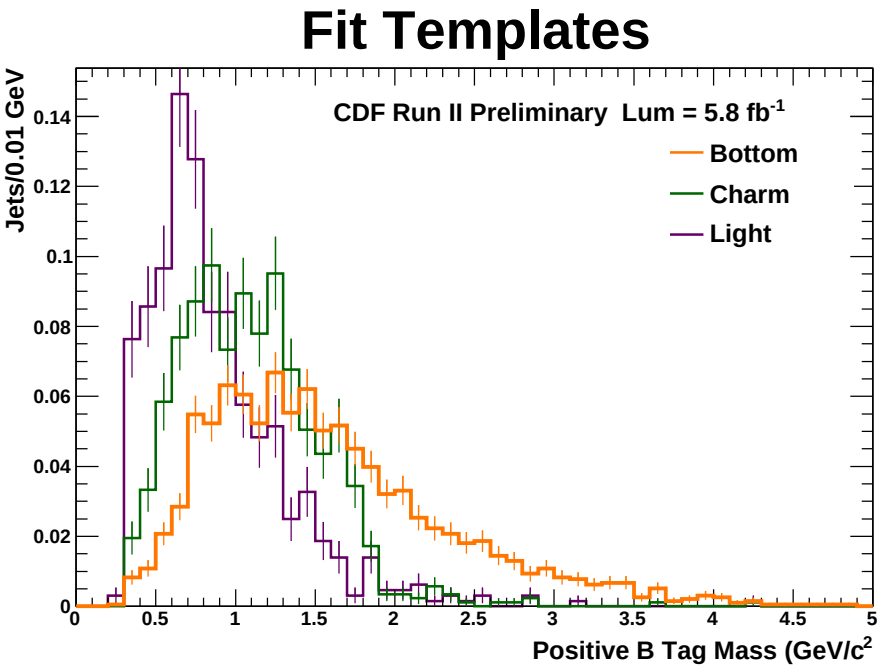

Figure 4.23: Vertex mass templates from QCD dijet MC, E_T 30 to 70 GeV with exactly 1 SVT trigger track in the jet.

4.5.4 Examples

Although the p.d.f.s are actually filled in three dimensional histograms, two dimensional projections are shown here. The first set shown in Fig. 4.25 is for a b tagger with a $|d_0|_{max}$ cut of 0.15 cm. (All the p.d.f.s shows in this section are from a single E_T and nSVTTRK bin, E_T between 30 to 70 GeV with exactly 1 SVT trigger track.) Shown are the b-quark p.d.f.s. There are correlations among all three variables, although for the u vs. v and u vs. α they do not appear significant in these two dimensional projections.

As the $|d_0|_{max}$ cut of the TStnSVF b tagger is increased to allow more tracks, the shapes of these p.d.f.s change as well. This can be most readily seen in the light-flavor p.d.f.s shown in Fig. 4.26 and 4.27. The first set shows how the relationship between u vs. v changes as the $|d_0|_{max}$ cut increases. The $|d_0|_{max}$ cuts shown are $|d_0| < 0.15$ cm, $|d_0| < 0.50$ cm, and $|d_0| < 1.0$ cm. The distribution in the tails changes with the relaxation

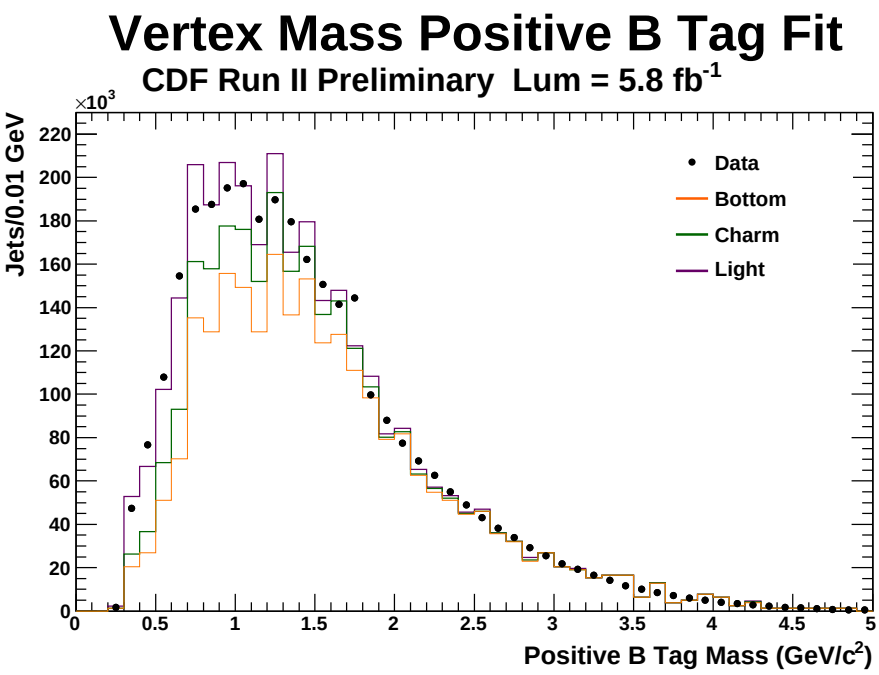

Figure 4.24: Flavor composition fit example for the JET trigger data, E_T 30 to 70 GeV with exactly 1 SVT trigger track in the jet.

of the $|d_0|_{max}$ cut.

The second set shows the changes to v vs. α. Here the shape and the correlations of the distributions broaden with larger max $|d_0|$.

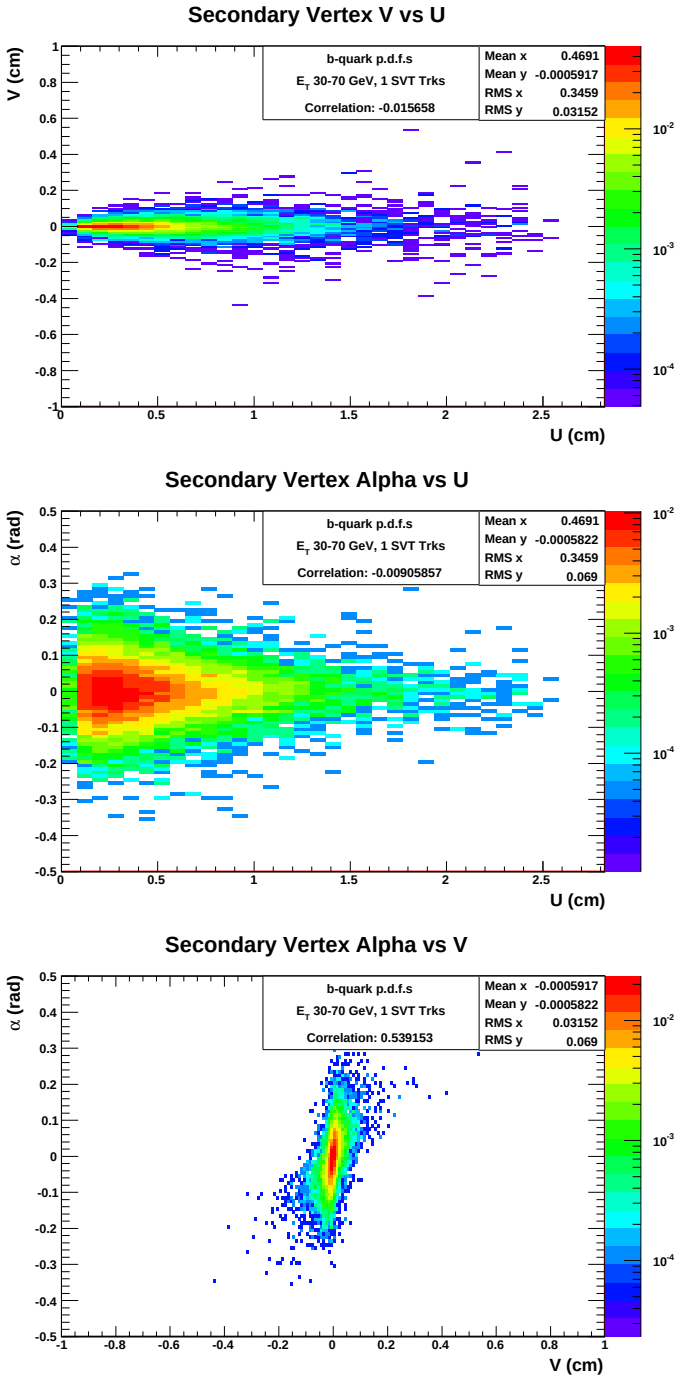

Figure 4.25: B-quark p.d.f.s for the default $|d_0|_{max}$ cut in the b tagger TStnSVF. Correlations among all three variables are present.

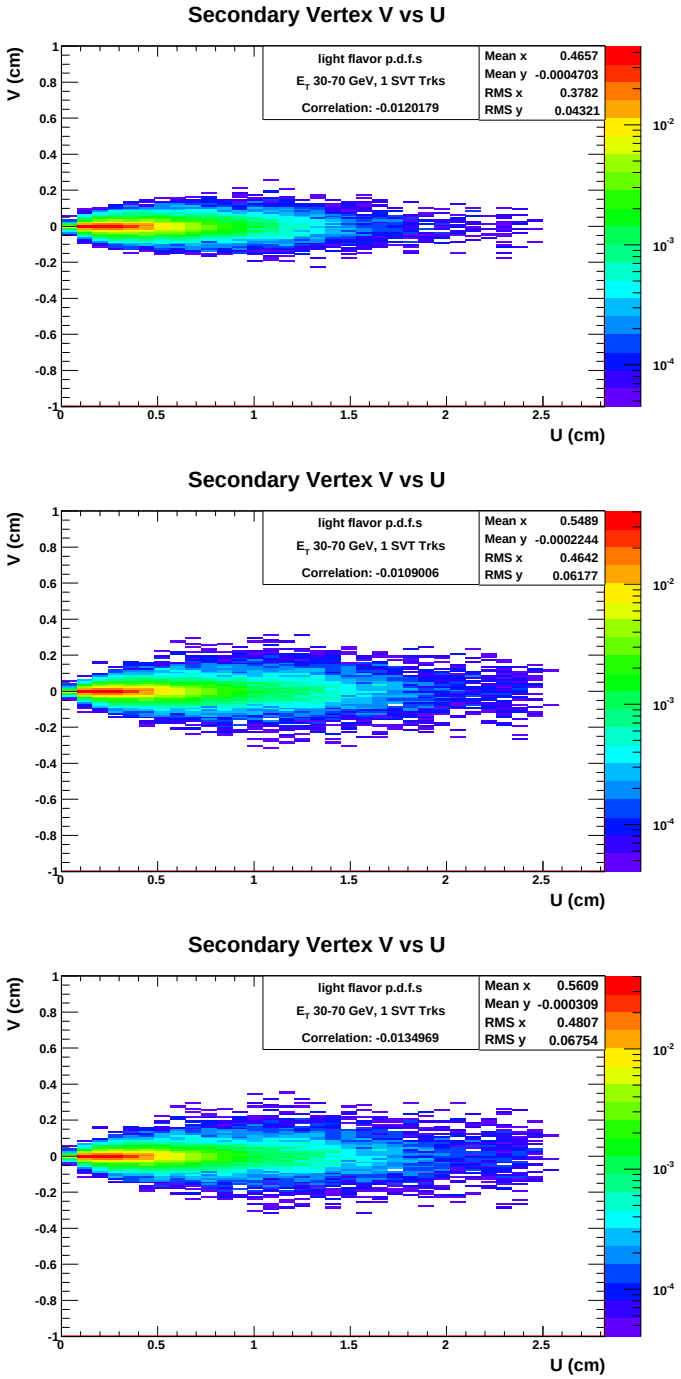

Figure 4.26: Light flavor p.d.f.s showing how the u vs. v distributions change as the $|d_0|_{max}$ cut increases from 0.15 cm (top-left) to 0.50 cm (top-right) and finally to 1.0 cm (bottom).

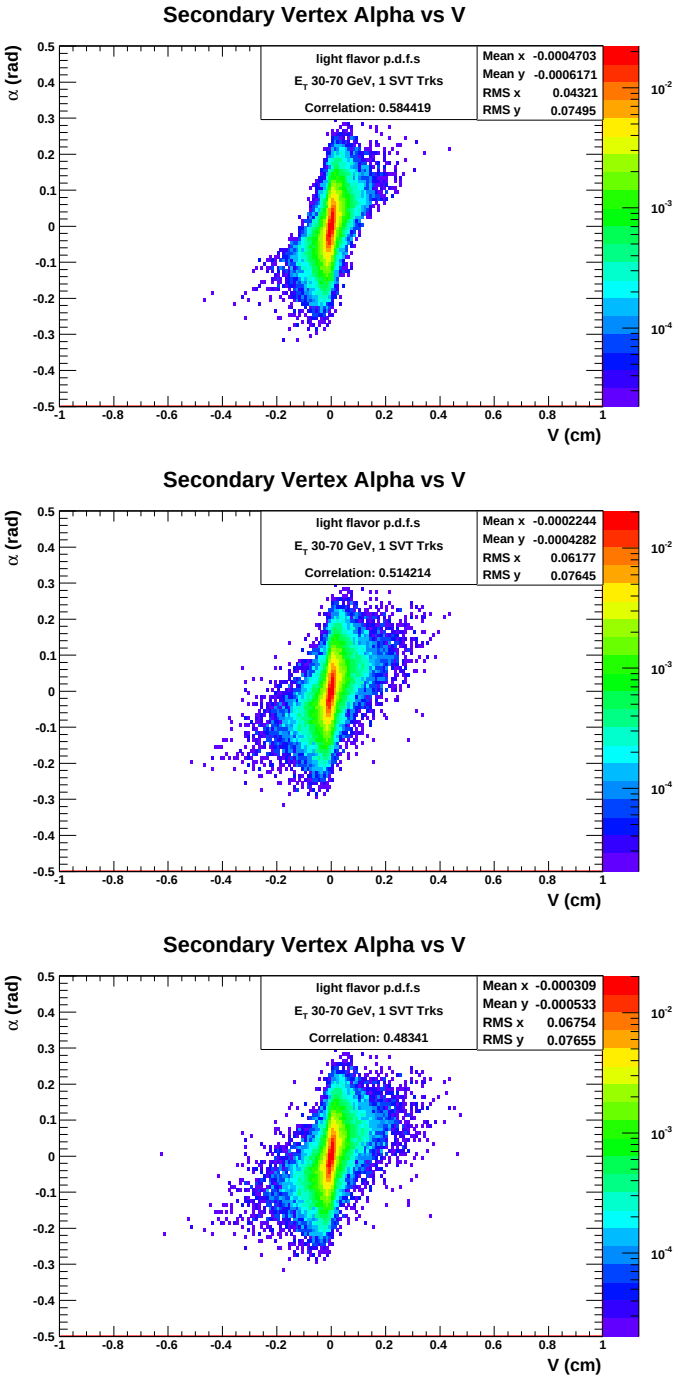

Figure 4.27: Light flavor p.d.f.s showing how the v vs. α distributions change as the $|d_0|_{max}$ cut increases from 0.15 cm (top-left) to 0.50 cm (top-right) and finally to 1.0 cm (bottom).

4.6 Pseudo Event Generation

4.6.1 Description of the Algorithm

Armed with completed p.d.f.s we can now move to generating pseudo events that will be used to estimate the amount of SM background for this search. Figure 4.28 diagrams the algorithm for generating pseudo events. We start with a real ZBB trigger event. The upper-left corner shows the kinematic selection discussed in Section 4.3.2. The control region path is highlighted in green while the signal region path is in red. Both paths end with the selection of a pair of jets, hereafter referred to as a dijet. This dijet becomes the building block for our pseudo events.

The kinematic information of a pseudo event (or pseudo dijet) originates from the real data. Thus the jet's E_T, η, etc. and the pair's ΔR, etc. are all obtained from data. This helps preserve any correlations that exist between any of these quantities. What we construct, and is prefixed with "pseudo" are the secondary verticies.

After a dijet has been identified we proceed to construct the pseudo event. We give each dijet pair "pseudo b tags" and then "pseudo flavor." We could simply look at the real b tagging information that the TStnSVF b tagger finds, but in order not to bias ourselves with any possible signal contamination we only use the kinematics of the event and artificially decide whether or not the two jets in a given dijet pair are both positively b tagged. As for the flavor, we do not have a HEPG bank in which we can determine the quark flavor of the jet. Thus we must assign a quark flavor based on the flavor composition of the jets in the ZBB trigger. Each of these two steps is shown in the flowchart and is discussed next. Finally, the last step is to sample from the p.d.f.s and build the pseudo secondary vertex information, i.e., position and momentum. This will be discussed in further detail afterwards.

Table 4.17 shows the datasets used to construct the pseudo events. The same ZBB

trigger data is used to calculate the b-tagging probability and the flavor composition of the ZBB trigger sample. A custom good run list, as described in Section 4.3.1, is used.

Trigger	**Run Range**						
	138425 -186598	190697 -203799	203819 -206989	206990 -212133	233133 -246231	252836 -261005	261119 -277511
(various) ZBB	`ezbbad`	`ezbbah`	`ezbbai`	`ezbbaj`	`ezbbbj`	`ezbbbk`	`ezbbbm`

Table 4.17: Trigger and Datasets used for constructing pseudo events as well as searching for our signal.

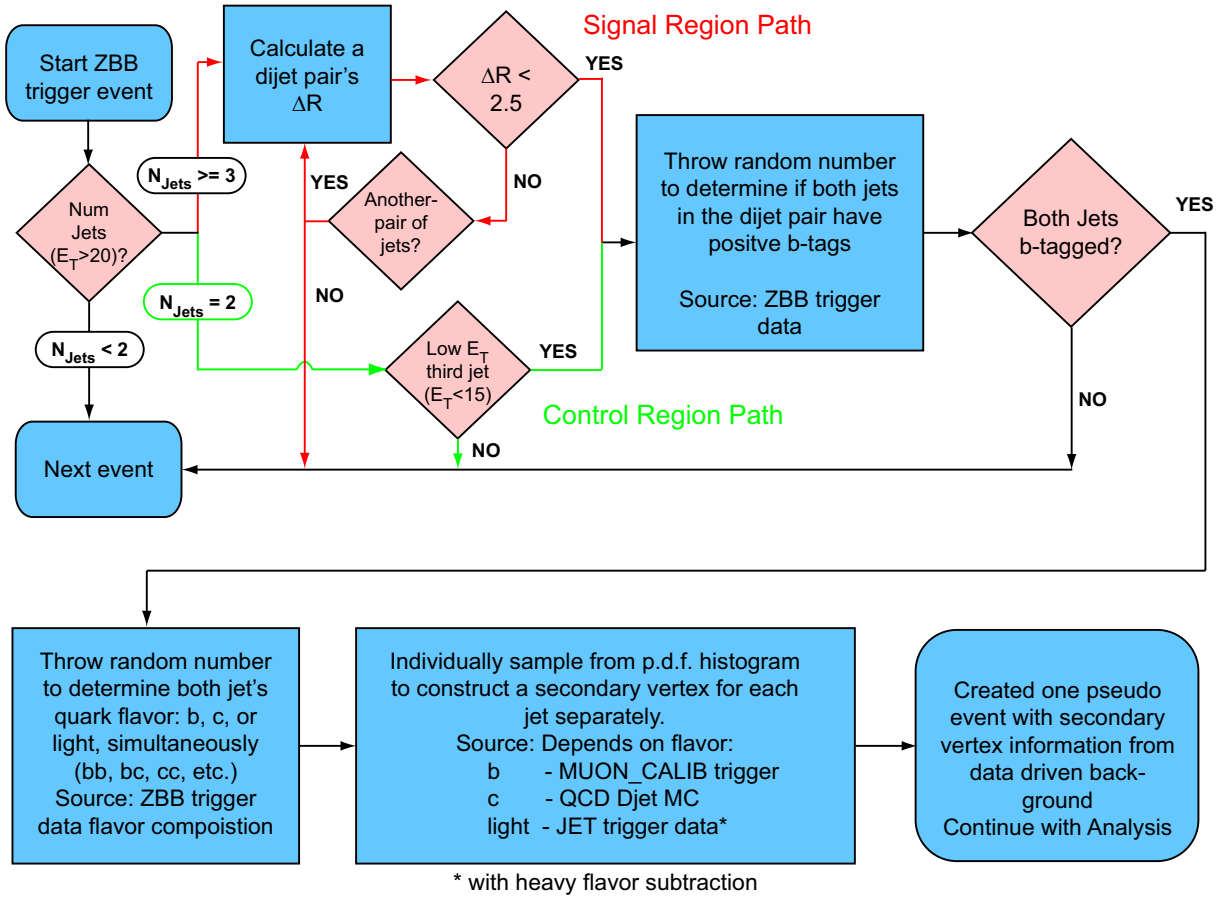

Figure 4.28: Flowchart showing the generation of a pseudo event using ZBB trigger data.

4.6.2 B tag Generation

With a dijet pair selected, from either the control region or signal region, we proceed to assign the jets in the pair pseudo b tags. This is simply a flag, 0 or 1 indicating whether or not the jet has a (pseudo) positive b tag. In order to build pseudo data that has the same luminosity normalization as the real ZBB trigger data, we demand that each dijet pair have the same probability to be b tagged as does the real ZBB trigger data. We construct a dijet b tag probability. This is the probability that **both** jets in the dijet have positive b tags. The purpose of this dijet probability, as oppose to the probability of single jets being b tagged, is to preserve kinematic correlations that exist in heavy flavor production.

A probability table is built for dijets split into 144 bins corresponding to 12 E_T/nSVTTRK bins for each of the jets in the dijet. The probability is simply the number of dijets with two positive b tags divided by the total number of dijets within each of the 144 bins. This division is performed using a Bayesian division calculation in order to calculate accurate asymmetric error bars. These errors will be used to calculate a systematic uncertainty related to this calculation. In addition, the probabilities calculated are done so separately for dijet pairs in the control and signal regions.

Table 4.18 shows how the calculation for the b-tag probability is performed for the case where one jet has $30 < E_T < 70$ GeV and the second has $20 < E_T < 30$ GeV; the dijet is for the signal region. Each jet can be in one of three possible nSVTTRK bins: 0, 1, and $\geq$2. The first section of the table shows the number of dijets where both jets have positive b tags. The middle is the total number of dijets. The bottom section is the division of the top table by the middle table in order to calculate the probability that the both jets have two positive b tags. Note that the largest probability is for both jets to have two or more large impact parameter SVT tracks. This is because the double

b tagged ZBB trigger sample is largely $b\bar{b}$ events (see Table 4.19).

When generating pseudo events a random number between 0 and 1 is generated. If this random number is less that the probability of both jets having positive b tags, then the pseudo dijet is considered b tagged, i.e., both jets has positive b tags. Only if the dijet pair has two positive b tags do we continue with the pseudo event generation. This procedure ensures that the number of pseudo dijet pairs will be comparable to the number of real dijet pairs in the ZBB data.

Tagged dijet	ET3070, SVT0	ET3070, SVT1	ET3070, SVT≥2
ET2030, SVT0	1252	4303	9727
ET2030, SVT1	3220	7385	9857
ET2030, SVT≥2	5119	6717	6637
All dijets	ET3070, SVT0	ET3070, SVT1	ET3070, SVT≥2
ET2030, SVT0	840880	665335	403921
ET2030, SVT1	317183	168691	69302
ET2030, SVT≥2	130013	40258	19826
Probability	ET3070, SVT0	ET3070, SVT1	ET3070, SVT≥2
ET2030, SVT0	0.0015	0.0065	0.024
ET2030, SVT1	0.010	0.044	0.14
ET2030, SVT≥2	0.039	0.17	0.33

Table 4.18: Example of how the double b-tag probabilities are calculated for dijets where one jet has $30 < E_T < 70$ GeV and the second has $20 < E_T < 30$ GeV; signal region. Jets are categorized by the number of SVT tracks.
Top: The number of tagged dijets, i.e., the numerator
Middle: The total number of dijets, i.e., the denominator
Bottom: The probability calculated from the top and middle tables.

4.6.3 Flavor Generation

In order to assign a flavor to each jet in the pseudo dijet pair, we must know the flavor composition of the ZBB trigger sample. However, unlike the flavor composition of the JET trigger samples where we were concerned with single jets, here we are concerned with the flavor composition of a pair of jets. With three possible flavor categories: b quark, c quark, and light-flavor, and two jets, there are nine possible combination of double-flavors for a pseudo dijet: BB, BC, BL, CB, CC, CL, LB, LC, and LL; where mixed states such as the BC and CB states are not considered degenerate since the first flavor is for the more energetic of the two jets. This is done to preserve the correlations between the flavors of jets. Nature tends to create pairs of jets with the same underlaying flavor ($b\bar{b}$, $c\bar{c}$, etc.) which necessitates the need for two-dimensional fits.

These fits are performed separately for both the signal region and the control region. The number of SVT trigger tracks that pass the ZBB displaced track trigger is used to separate the dijets into bins. There are three possible nSVTTRK bins and two jets for a total of nine bins.

We use two dimensional fits of the b tag's vertex mass to determine the flavor of dijet pairs with positive b tags. We use the same Pythia QCD dijet MC as in Section 4.5.3 to build MC templates of the vertex mass. These templates are more complex now that we are dealing with a simultaneous fit. First the individual b quark, c quark, and light-flavor MC templates are joined to form two-dimensional vertex mass p.d.f.s for BB, BC, BL, etc. Then the vertex mass p.d.f.s are merged to form a single set of vertex mass p.d.f.s that encompasses all nine double-flavor states. Because the nine double-flavors are constrained by the physical property that they must add to one, there are eight fractions which we fit. These eight fractions are algebraic combinations of the nine double-flavor states.

Fits are performed using the RooFit package. The resulting fractions are converted

into the double-flavor states, which are more easily understood than the fitted fractions. Figure 4.29 and Table 4.19 show an example of the fits and the results for the signal region when both jets have exactly one SVT trigger track.

Double Flavor State	Percentage (%)
BB	90.9
BC	0
BL	5.09
CB	0
CC	0
CL	0
LB	1.14
LC	0
LL	2.86

Table 4.19: Double flavor fraction fit results for the signal region when both jets have exactly one SVT trigger track.

When generating pseudo events/pseudo dijets, the flavor of the dijets is assigned using the double-flavor states calculated from the fit. For example if the fit reports that 90.9% of the (real) dijets in a particular bin are BB, then the algorithm gives an 90.9% chance that the double-flavor of a pseudo dijet is BB.

At this point in the algorithm we have generated pseudo dijets with b tags and flavors assigned. The last step is assigning information about the secondary vertex.

4.6.4 P.d.f. sampling

Armed with the pseudo flavor of the dijets, we can now sample from the p.d.f.s discussed in Section 4.5. In this step the jets are sampled independently. The p.d.f.s are stored as a three dimensional histogram, thus the procedure to sample is fairly straightforward. First the cumulative distribution function (c.d.f.) of the histogram is calculated, then a random number between 0 and 1 is generated, and its value is found along the c.d.f. A

bin is extracted from the c.d.f. representing the bin in which to sample, and the u, v, and α corresponding to that bin is then assigned to the jet.

This procedure is similar to what nature does when a particle decays at a secondary vertex. A particle with a non-zero lifetime, such as a B hadron, travels for a given lifetime and then decays with a position and a direction. Sampling from the p.d.f.s effectively assigns the pseudo jet a pseudo secondary vertex position and direction. Because the decays in nature are independent events, we can sample from the p.d.f.s separately for each jet.

At the end of this procedure we have created a set of pseudo events (made up of pseudo dijets) where the b-tagging proportion is the same as the ZBB trigger data, the flavor of the pseudo dijets is derived from the same ZBB trigger data, and the secondary vertex information is obtained from the SM via the p.d.f.s. We can then search for our signal using the real ZBB data, while using the pseudo events to estimate the SM background from SM processes.

As we discuss in Section 5.1.1 however, we use this technique to generate multiple background estimates with one set of generated pseudo data.

4.6.5 Validation

We use the control region to validate this algorithm. Because we expect the control region to be devoid of signal, we can compare the real dijet data to the pseudo dijets generated to see if the pseudo events are well behaved. For the purposes of this validation, exactly one pseudo event was generated for each real event, and the p.d.f.s were only sampled once for each pseudo jet. Thus both the real data and the pseudo data should have rates that are within their statistical errors.

We validate by looking at the two variables we developed for this analysis: ψ and ζ. In Fig. 4.30, the real ZBB data (black) ψ is shown along with the pseudo data ψ. The latter

is a stacked histogram with orange representing b quarks, green representing c quarks, and purple representing light-flavor. That the vast majority of pseudo jets are b quarks is not surprising given the displaced track trigger in the ZBB trigger path. Some discrepancies are noted along the tails of the distribution between the real data and the pseudo data. The cause of this discrepancy is due to the binned nature of the p.d.f.s used to sample for the secondary vertex, and thus ψ. This will be part of the systematic uncertainties calculated due to the p.d.f.s. These discrepancies would result in an overestimate of the background as there are more pseudo events than real events along the tails.

Validation plots of ζ are shown in Fig.s 4.31, 4.32, and 4.33. Figure 4.31 shows the ζ distribution for all dijets. Here the real data and pseudo data are very similar. Distributions were also made splitting the dijets into multiple variables: ΔR, ΣE_T, invariant mass, number of primary vertices, etc. in order to verify that this algorithm for generating pseudo events is robust and properly models the correlations that may be present in dijet events.

Figures 4.32 and 4.33 show the ζ distribution for dijets split into different bins; Fig. 4.32 is split into ΔR bins while Fig. 4.33 is split into bins of the number of primary vertices in the event. With no significant differences in the distributions we conclude that the procedure constructs pseudo events that are valid for estimating the background for our signal search.

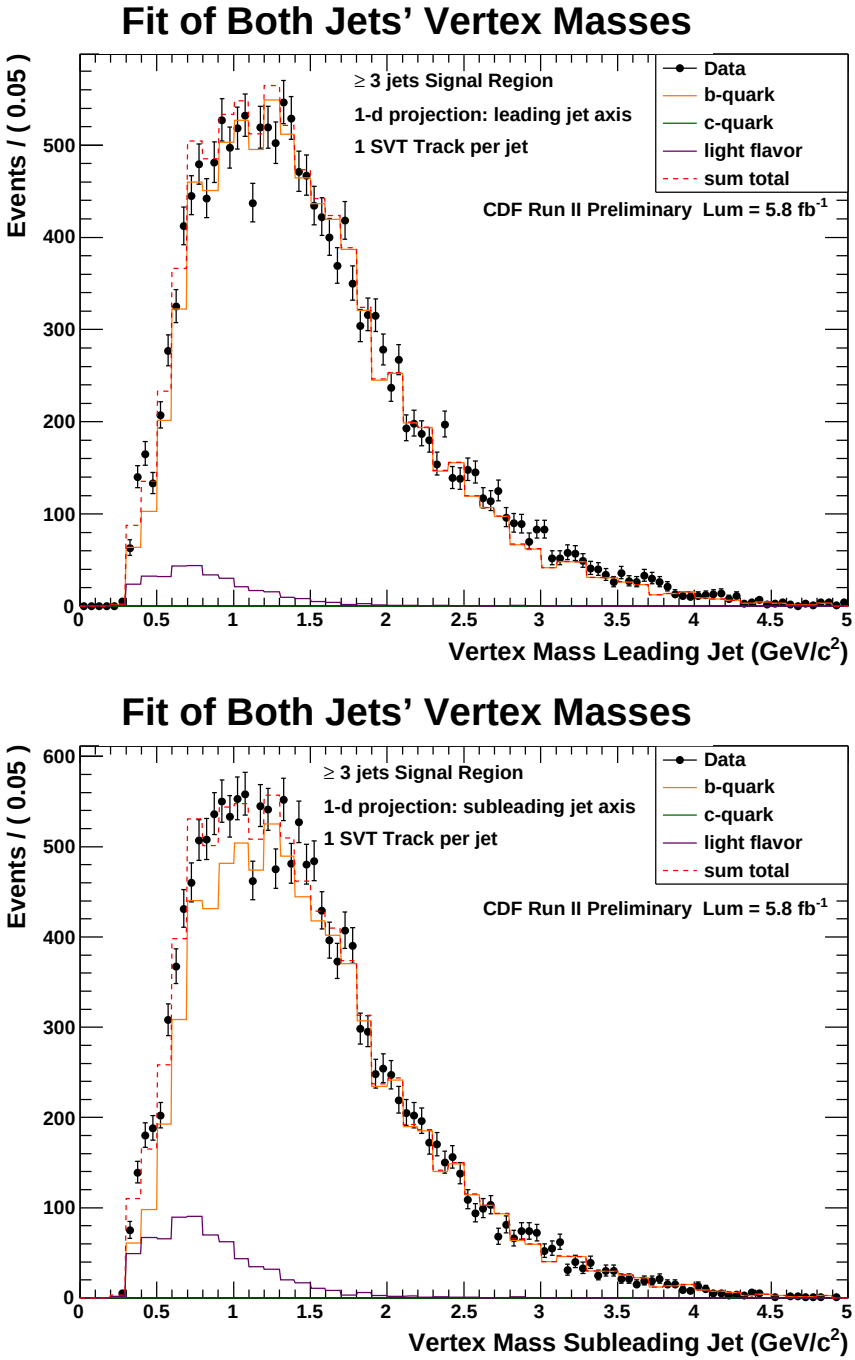

Figure 4.29: Example of double-flavor fits for signal region dijets where each jet has exactly one SVT trigger track. Histograms are projections of the two-dimensional fit onto the axis of each jet.

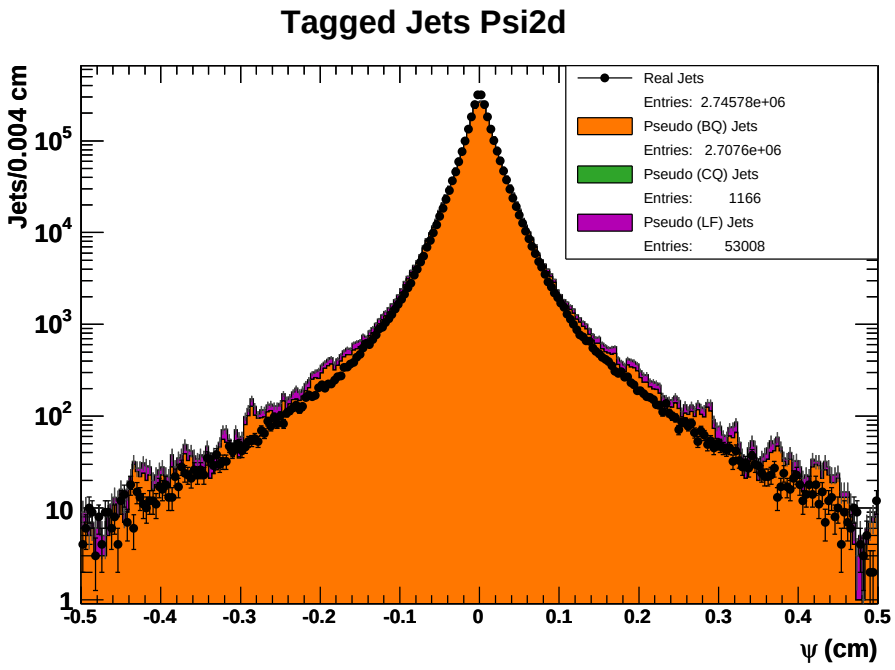

Figure 4.30: Real (points) and pseudo jets (stacked) distributions for ψ for all jets.

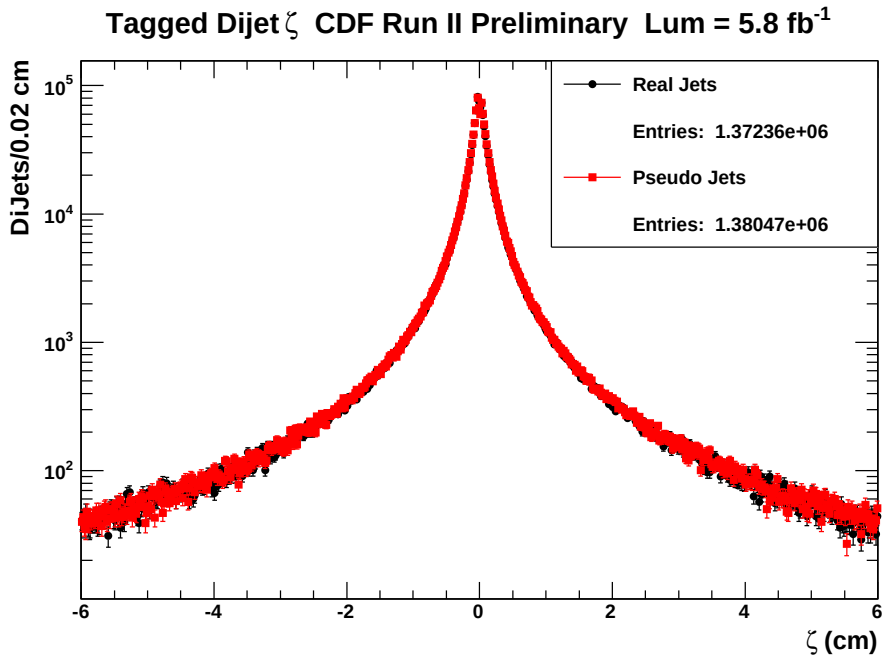

Figure 4.31: Real (black) and pseudo dijets (red) distributions for ζ for all jets.

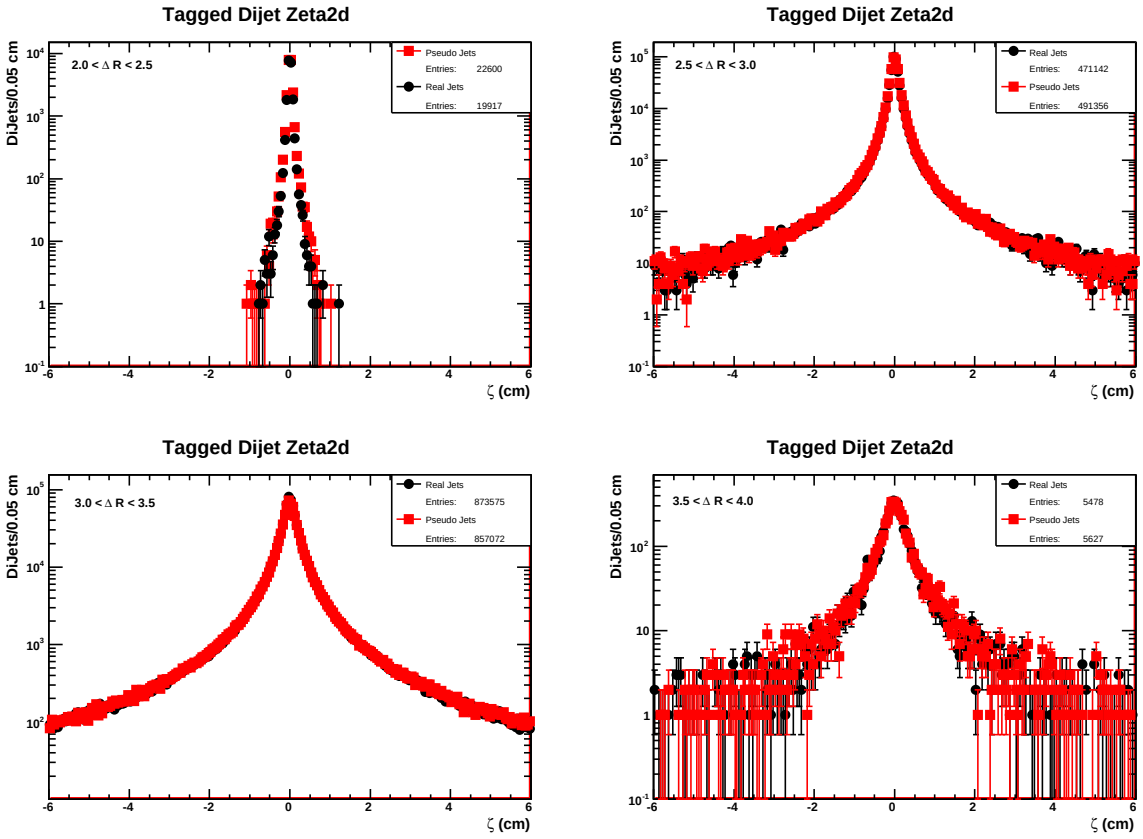

Figure 4.32: Real (blcak) and pseudo dijets (red) distributions for ζ for jets split into bins of ΔR.

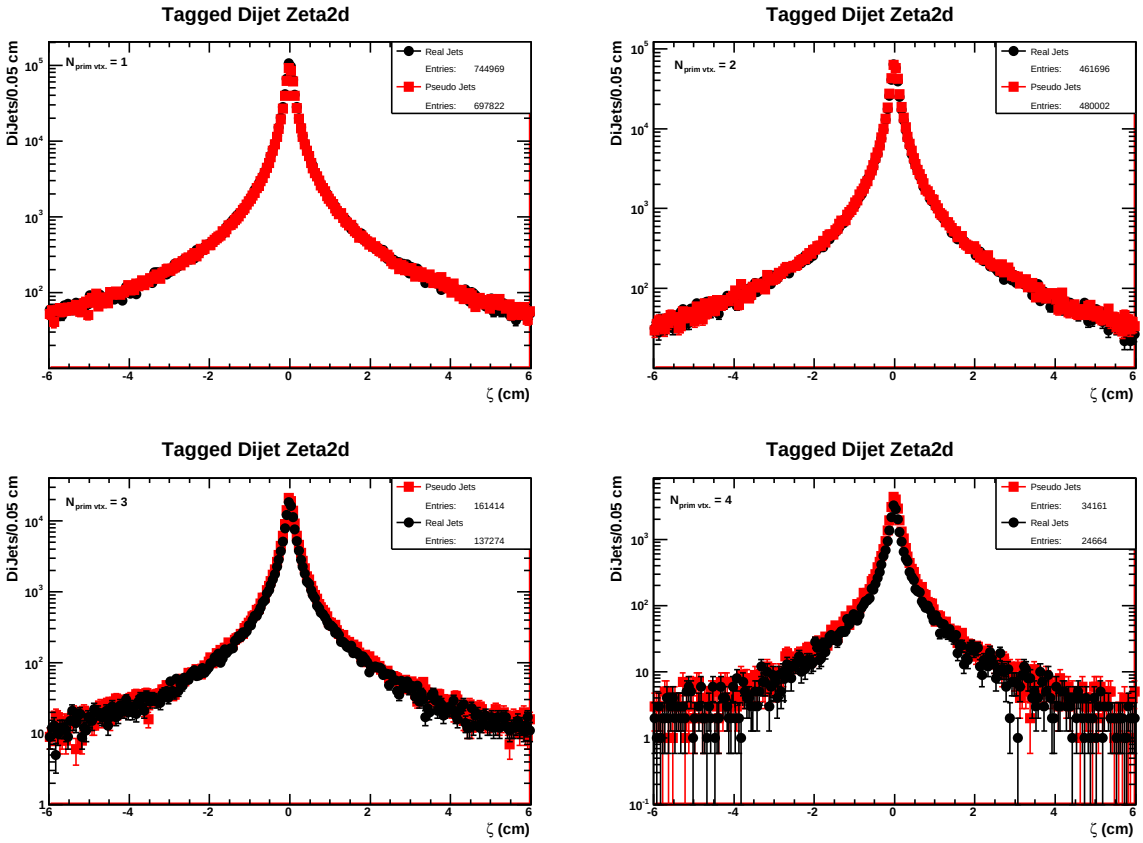

Figure 4.33: Real (black) and pseudo dijets (red) distributions for ζ for jets split into bins of $N_{prim.vtx}$.

CHAPTER 5

RESULTS

5.1 Signal Search

5.1.1 Building A Background Estimate

For the background estimate, we sample from the p.d.f.s many times for a given pseudo dijet pair to build multiple pseudo data. This is best described in Fig. 5.1 and 5.2. Figure 5.1 is simply Fig. 4.28 with boxes overlaid. These boxes are then used in Fig. 5.2. First there is the kinematic selection (orange), and then the pseudo event generation (magenta), which consists of the b-tag generation and flavor assignment. Now for each pseudo dijet, we sample from the p.d.f.s many times (navy). Each set of sampling is called a "pseudo experiment." Each pseudo experiment is then treated independently, and is passed through the same set of analysis cuts, which will be described in further detail below. The resulting number of events that pass these cuts is collected for each pseudo experiment. The mean of this distribution is termed the background estimate.

The background estimate represents the number of events in data that would pass the analysis cuts if only SM processes contributed to the observed data. In effect it is the null hypothesis for this search.

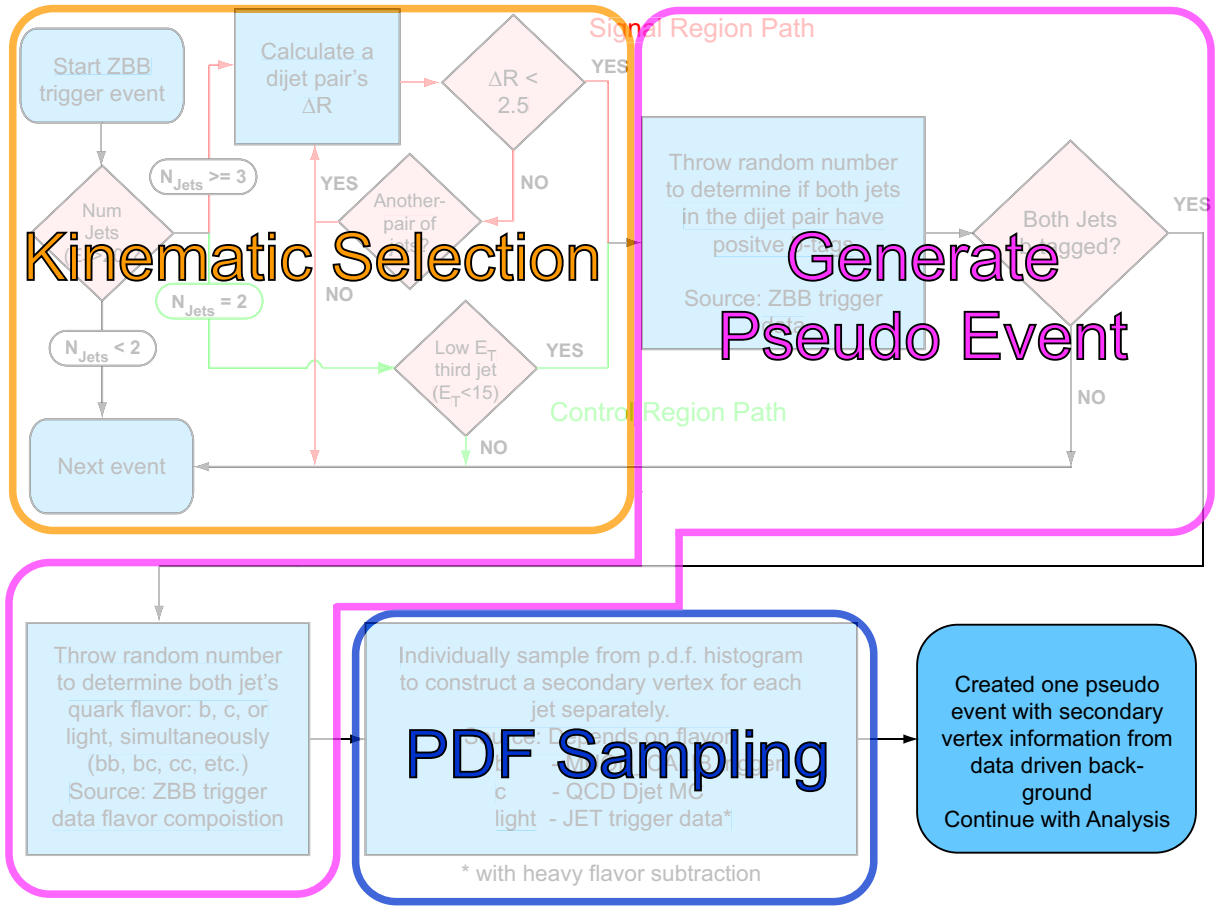

Figure 5.1: Flowchart showing the generation of a pseudo event using ZBB trigger data overlaid with boxes for Fig. 5.2.

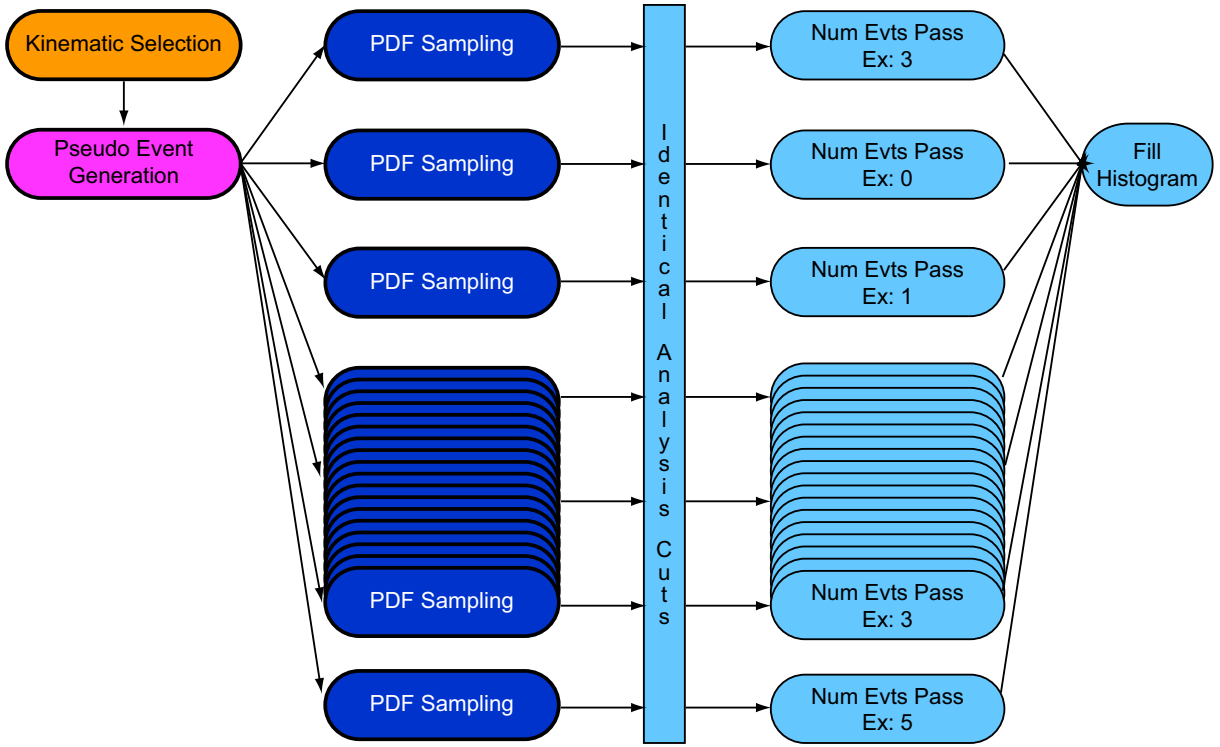

Figure 5.2: Flowchart showing how multiple pseudo experiments are performed with the pseudo data in order to form a background estimate.

5.1.2 Signal Background Optimization

$|d_0|_{max}$ Cut

To decide on a $|d_0|_{max}$ cut we first looked at distributions of the number of events (di-jets) in both signal MC and the pseudo data/background estimate. For the purposes of deciding this cut, we use the one pseudo dijet per real dijet as described in Section 4.6. Twenty $|d_0|_{max}$ cuts were tried in the TStnSVF b-tagging algorithm, representing twenty operating-points. Figure 5.3 shows the distribution as a function of the $|d_0|_{max}$ cut for one signal MC sample ($M_{h_0} = 130$ GeV, $M_{HV} = 40$ GeV, $c\tau_{HV} = 1.0$ cm) and a pseudo event background sample with one pseudo experiment generated. Each data point represents the number of events that have two positive b tags for that particular $|d_0|_{max}$ cut.

At some point both distributions plateau. The number of events in the background sample jumps up and down. This is due to the effect that sometimes adding an additional track reduces the number of b tags at that particular operating point. This occurs when the additional track contributes too much to the χ^2 of the vertex fit and cannot be pruned from the vertex, thus eliminating the b tag altogether.

The distribution for the signal shows that larger $|d_0|_{max}$ cuts allow for more signal acceptance, while the background plateaus at about $|d_0|_{max} < 0.70$ cm. Logically, this means we can pick a maximal $|d_0|_{max}$ cut, which would accept as many signal MC events as possible. However, this is not feasible as there are physical constraints present due to the CDF detector.

The inner detector at CDF, Fig. 5.4, consists of a beampipe where the zero-th layer of the Silicon detector is attached, Layer 00 (L00), followed by layers 1 through 5 of the SVX detector. The inner radius of the beampipe is $r_{bp-in} = 1.26$ cm. In general, tracks at CDF are constructed from the outside-in. COT (outside) hits are fit to a track helix

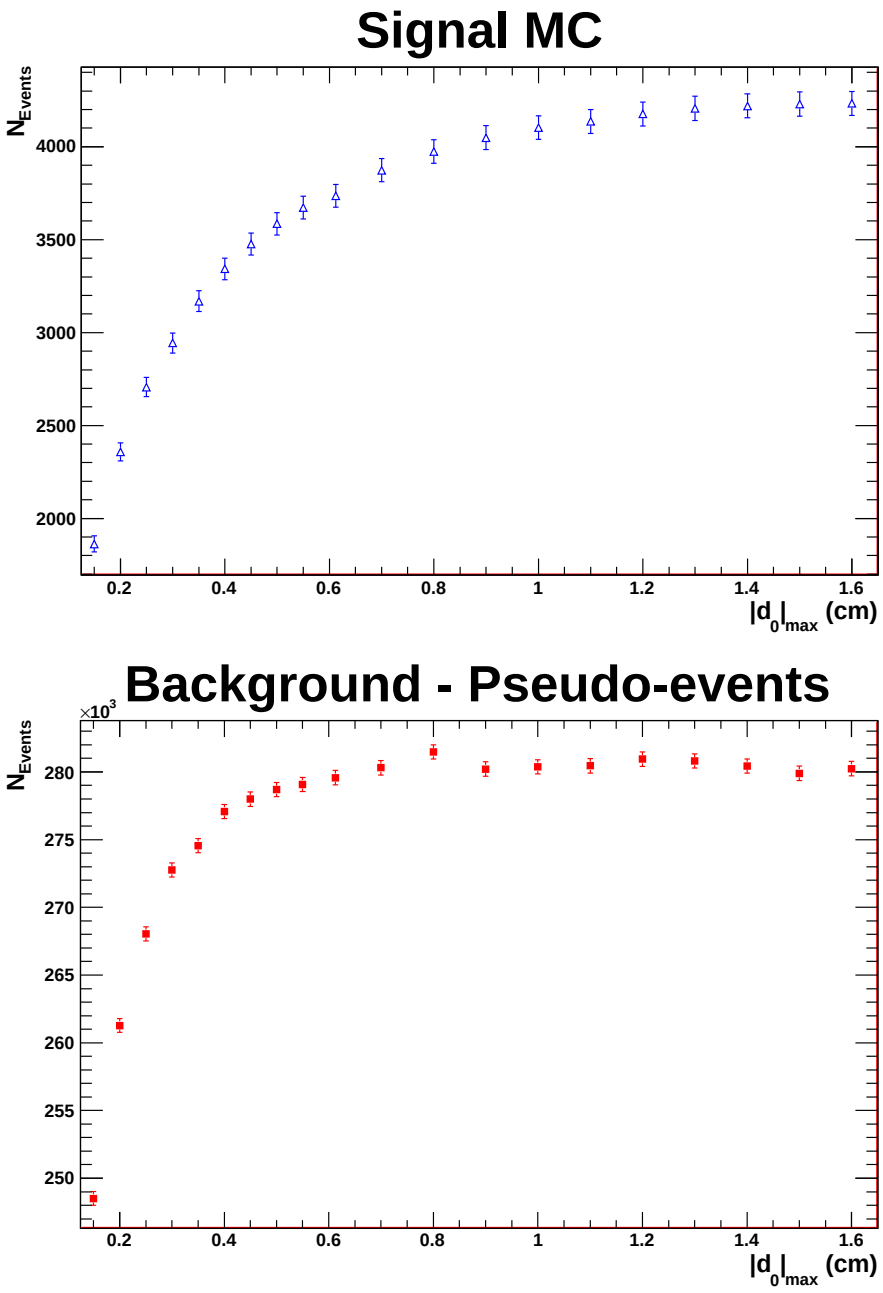

Figure 5.3: Number of signal (left) and background (right) events vs. $|d_0|_{max}$.

and this helix is then extrapolated back into the inner detector, where Silicon detector hits are attached. However, only tracks with $|d_0|$ of the track with respect to the origin (not the primary vertex) less than the radius of the beampipe can physically have L00

hits.

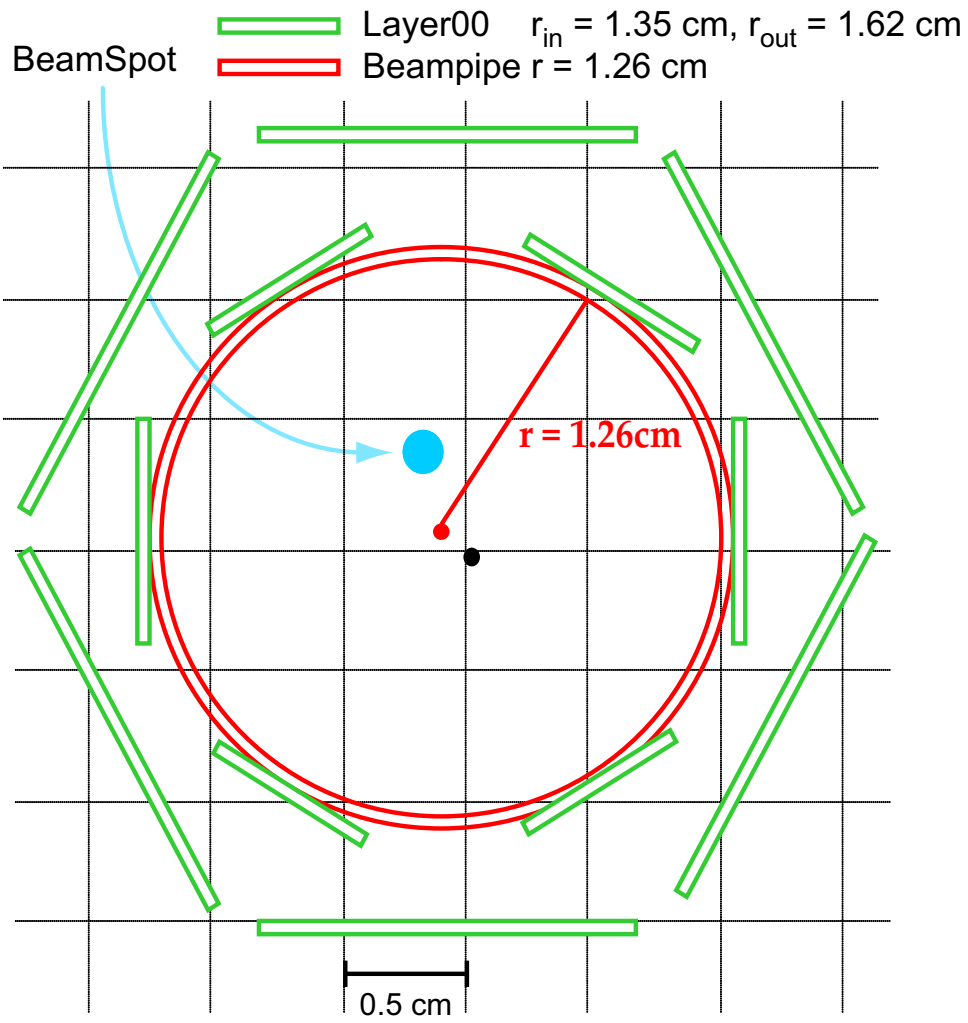

Figure 5.4: Diagram of the inner detector at CDF. The beam spot/primary vertex is not in the center of the detector.

We chose a $|d_0|_{max}$ cut such that the helix of any track within the event is still within the inner beampipe radius, because this track may have L00 hits. The L00 hits are important because they improve the resolution of a track's helix parameters, especially d_0. Figure 5.5 shows the distribution of $r_{prim-vtx}$, the two dimensional radius from the origin to the primary vertex in the plane transverse to the beamline, for the events in the ZBB data sample we are using. On the y-axis is the run number. The vast majority of

events in this data sample have their $r_{prim-vtx} < 0.2$ cm. This means that the $|d_0|_{max}$ w.r.t. to the primary vertex where the helix of the track is still within the inner beampipe radius is $|d_0|_{max} < 1.0$ cm, shown with a dashed magenta line. This dashed line represents the point where any track from a primary vertex on this line will have its $|d_0|_{max}$ with respect to the origin (not the primary vertex) less than 1.26 cm, in which case the track can have a L00 hit. Consequently we choose the $|d_0|_{max}$ cut of 1.0 cm for our signal search.

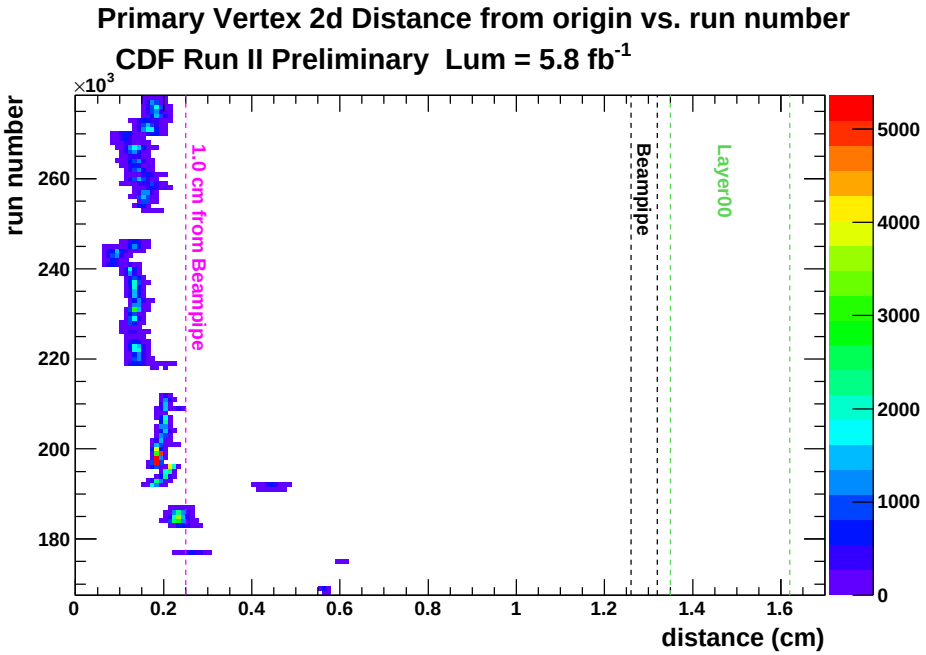

Figure 5.5: Run number vs. two dimensional distance between the primary vertex and the center of the beampipe. The magenta line represents a primary vertex where a track with $|d_0|_{max}$ of 1.0 cm would still be within the beampipe.

Optimization of Variables

With the $|d_0|_{max}$ cut set we proceed to optimize the other variables in the analysis.

1. Angle between the two jets (ΔR)

2. $|\psi|$, the impact parameter of a b tagged jet

3. ζ, the decay distance of the HV particle

For $|\psi|$, we demand that both jets have very high impact parameter as jets from signal generally have large $|\psi|$. For ζ we require that the decay distance be positive and large.

We perform a $S/\sqrt{B}$ analysis in order to optimize these variables. The B in this equation is the result of 1,000 pseudo experiments, where B is the mean value of the distribution of events that pass the various cuts. HV particles that are lighter in mass will have daughter b quarks more co-linear than for heavier HV particles. To account for this we develop two searches: a low HV mass search and a high HV mass search. The signal MC samples where the HV mass is $M_{HV} = 20$ GeV are categorized as the low HV mass search and have different variable cuts. The other samples are placed into the high HV mass search. Table 5.1 lists which search each signal MC sample corresponds to.

Higgs Mass (GeV)	**HV Mass (GeV)**	**HV life-time (cm)**	**Search**
130	20	1.0	low HV mass
170	20	1.0	low HV mass
130	40	1.0	high HV mass
170	40	1.0	high HV mass
170	65	1.0	high HV mass
130	40	0.3	high HV mass
130	40	2.5	high HV mass
130	40	5.0	high HV mass

Table 5.1: Signal MC samples corresponding to low and high mass HV particle searches.

The low HV mass search has a ΔR_{max} cut on the maximum ΔR of the jets. While the high HV mass search has both a ΔR_{min} and a ΔR_{max} cut, specifying a range of opening angles. Numerous $S/\sqrt{B}$ and efficiency graphs are used to study the effects of these variables on the signal and background. Since it would be impractical to show them all, only a few graphs are shown here from the final variable cuts.

The cuts chosen for the high HV mass search are shown in Table 5.2. In addition, Fig. 5.6 shows $S/\sqrt{B}$ graphs for ζ for different signal MC samples. In the left-hand column are the three signal MC samples of different masses, while in the right-hand column are the samples where the lifetimes have been reweighted.

Variable	**high HV mass**		**low HV mass**	
$\|d_0\|_{max}$ (cm)	$<$	1.0	$<$	1.0
ΔR_{min}	$>$	0.75		n.a.
ΔR_{max}	$<$	2.0	$<$	0.75
$\|\psi\|$ (both jets) (cm)	$>$	0.11	$>$	0.12
ζ (cm)	$>$	0.8	$>$	0.7

Table 5.2: Variable cuts for both the low and high HV mass searches.

We chose $\zeta > 0.8$ cm as our variable cut. While there is no one point where the signal is optimized with respect to the background for all six samples, we feel that this value allows for a high signal efficiency while reducing the background in all six cases.

An additional geometric cut is imposed on ζ. The magnitude of ζ must be less than the distance from the primary vertex to the closest secondary vertex. This ensures that the intersection is between the primary vertex both secondary vertices.

For some variables, $S/\sqrt{B}$ optimization is not feasible, and another procedure is used to select the cut value. Figure 5.7 shows $S/\sqrt{B}$ increasing as the $|\psi|$ cut grows for a single signal MC sample. Other signal MC samples behave similarly. In order to understand this behavior we look at the S and the B that are used to calculate this graph; see Fig. 5.8.

On the top is the signal (blue) while on the bottom is the background estimate (red). The number of signal events falls off monotonically at high $|\psi|$. But in this signal MC sample the effect of the cut only reduces the number of signal events by about 10%. However the background falls very quickly at first, and then levels off asymptotically toward zero. Thus our procedure is to select a value of the variable at a point where the cut no longer significantly affects the background distribution. This is the point where a

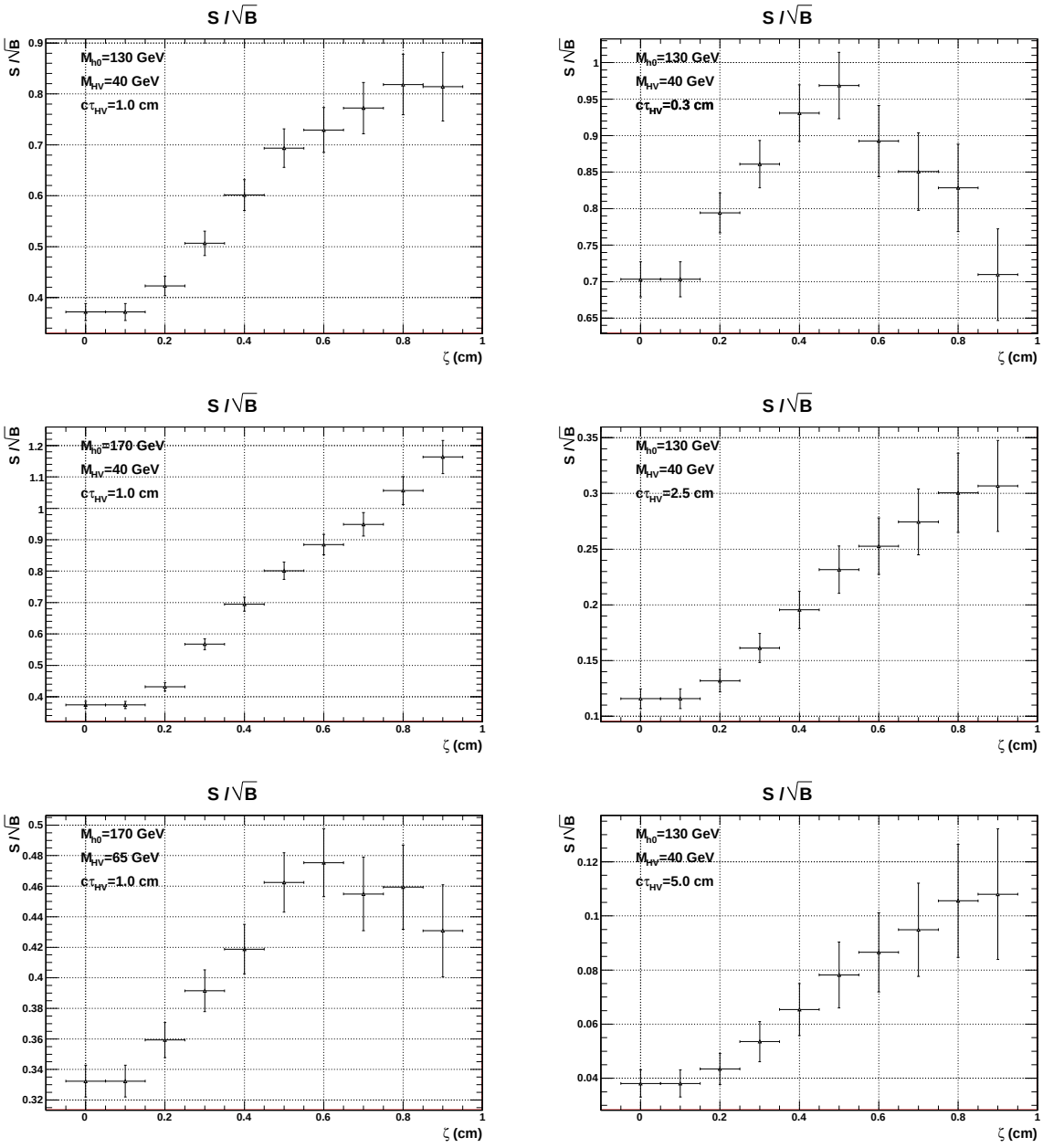

Figure 5.6: $S/\sqrt{B}$ graphs for ζ, other variables held constant, for signal MC samples in the high HV mass search.

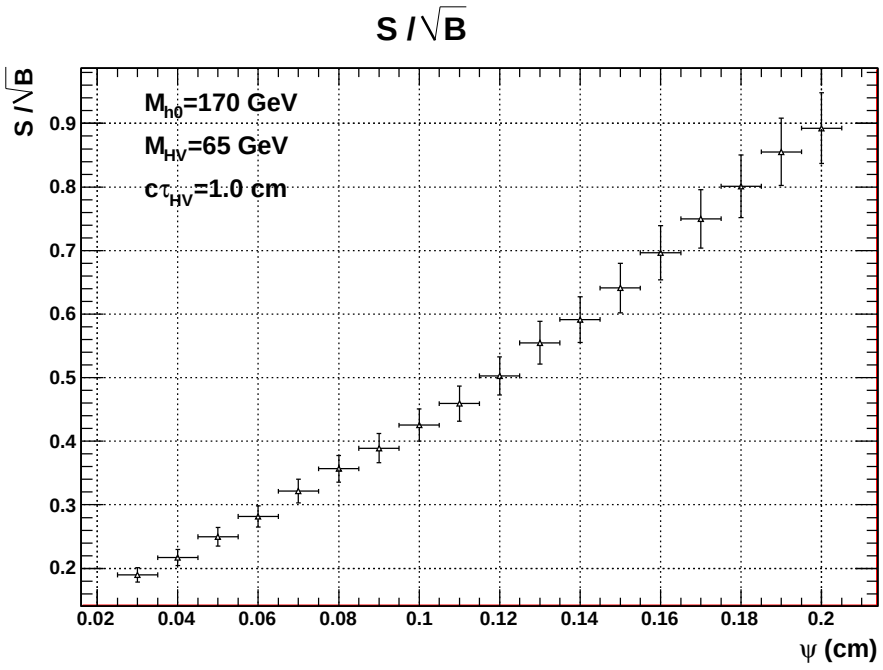

Figure 5.7: $S/\sqrt{B}$ graph of $|\psi|$ for a single MC sample.

larger cut on ψ provides little additional benefit. We choose the "knee" of this background distribution at $|\psi| > 0.11$ cm as the cut in the high HV mass search.

The low mass HV search optimization was performed nearly identically to the high mass HV search. The main difference is the ΔR cut. Since the daughters of the HV particle are more co-linear, only a $\Delta R_{max} < 0.75$ cut is imposed; no ΔR_{min} cut is applied.

An unanticipated source of background became apparent when we applied these analysis cuts to the real ZBB trigger events. A few events in the low HV mass sample appear to contain a single secondary vertex from a B hadron, in which some of the decay products are found in each of two nearby jet cones. Two features of these events are that 1) the two secondary vertices are very close to each other, (ΔS_{2d}), and 2) the total invariant mass of all the tracks in both vertices ($TotalVtxMass$) is less than the b-quark mass; see

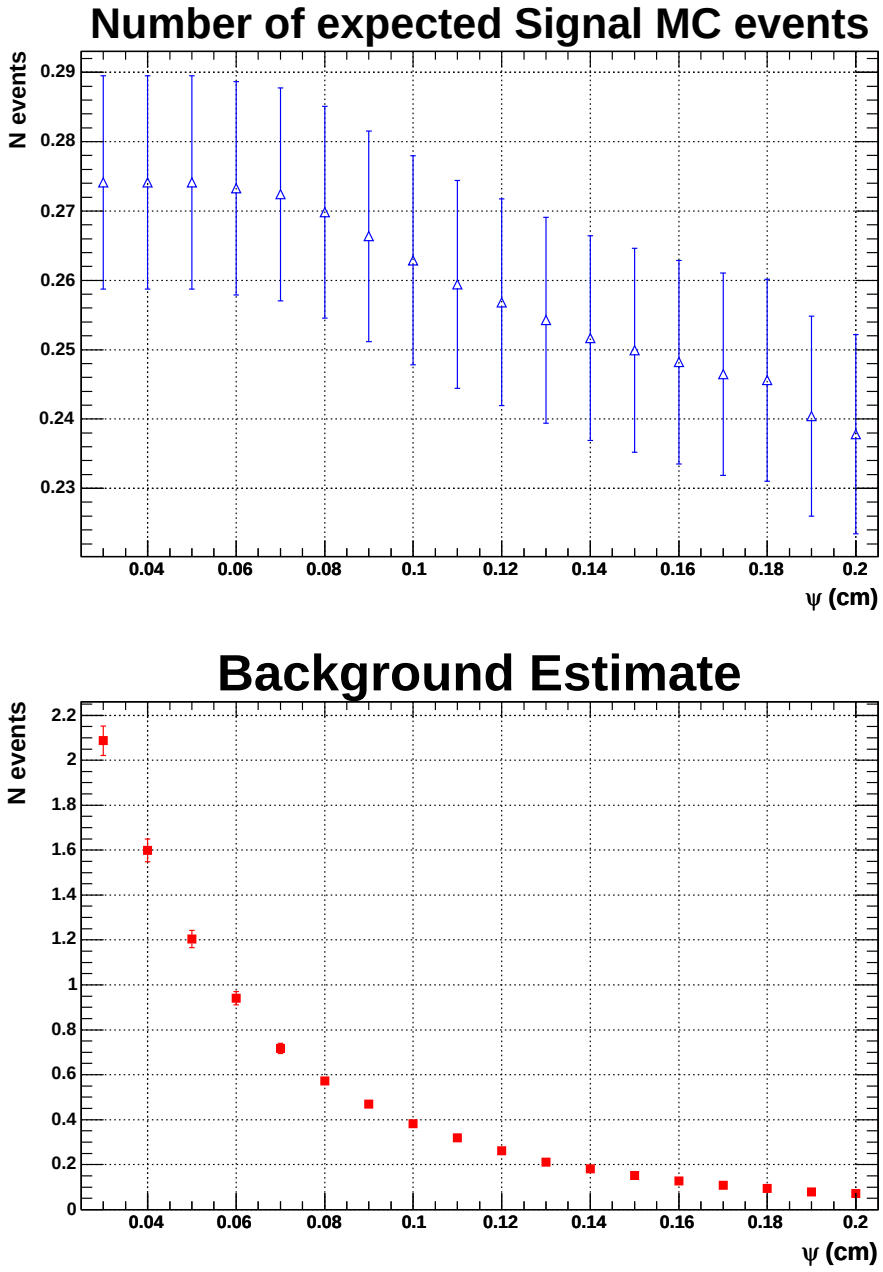

Figure 5.8: The signal (top) and background (bottom) used to calculate the $S/\sqrt{B}$ graph for $|\psi|$.

Table 5.3. These cuts were added to the low HV mass search analysis cuts because when these requirements are applied to the signal MC sample, there is a negligible reduction

in the efficiency. Events with these features are most likely QCD $b\bar{b}$ decays where the jet reconstruction algorithm clusters the energy of one leg of the decay into two jets. Then the TStnSVF b-tagging algorithm vertexes the tracks in each jet separately, but finds the same decay vertex of the B hadron. This effect is a background that was not considered a priori.

In one case, run number 186306, event number 4192804, there is actually a third jet with a secondary vertex as well. This third jet is on the opposite side of the detector from the two jets that make up the dijet analyzed. (This event has three $\Delta R = 0.4$ cone jets.) We believe that this is a QCD $b\bar{b}$ event, where on one side of the detector the energy deposited in the calorimeter is reconstructed as two jets by the jet clustering algorithm. If for this event, we reconstruct the calorimeter energy with a cone $\Delta R = 0.7$, we find only one jet where there was once two. (The aforementioned third jet on the other side of the detector still exists. Thus this event has two $\Delta R = 0.7$ cone jets.) The TStnSVF b-tagging algorithm can be modified to use all the tracks in a cone of $\Delta R = 0.7$ as well. Doing so results in both jets having one secondary vertex. The vertex track masses for these vertices are 3.25 and 3.98 GeV, both high enough to be consistent with a B hadron decay, but below the b-quark mass. This is further evidence that this event may be a $b\bar{b}$ decay.

Variable	**low HV mass**	
ΔS_{2d} (cm) OR	$>$	0.06
$TotalVtxMass$ (GeV)	$>$	5.0

Table 5.3: Additional cuts on the low HV mass search due to an unanticipated background.

5.1.3 Results

With the variable cuts set, we proceed to run 10,000 pseudo experiments for both mass searches. Figure 5.9 shows the results of these pseudo experiments. The low HV mass search (purple) and high HV mass search (green) are Poisson distributions with means $\mu_{low} = 0.58$ and $\mu_{high} = 0.29$. These are the estimated numbers of SM background events. The statistical uncertainty on these numbers, the mean divided by the squared root of the number of pseudo experiments, is negligible.

With the same variable cuts we can also calculate the number of expected signal MC events that we would expect in the same amount of luminosity as the ZBB trigger. This is done by calculating the number of events that pass the cuts in each signal MC sample and multiplying this number by a scale factor consisting of the luminosity of the ZBB trigger sample multiplied by the cross section of the Higgs ($gg \rightarrow h_0$) divided by the number of signal MC events generated. The Higgs cross sections were obtained from Ref. [66] and are reproduced in Table 5.4. The branching ratio of the Higgs is assumed to be 100% to the HV particles, and the branching ratio of the HV particles is assumed to be 100% to $b\bar{b}$ quark pairs.

When calculating the expected number of signal MC, two reweightings are performed in order to account for differences between the ZBB trigger data and signal MC events. First, a reweighting to account for differences in the luminosity profile of the signal MC events vs. data events. Second, a reweighting to account for different trigger efficiencies for different run ranges.

A first reweighting is performed on an event-by-event bases when calculating the yield of signal MC events, Y_i. The luminosity of the ZBB trigger data events and the signal MC events are different. At higher luminosities, more interactions occur, resulting in multiple primary vertices. We use the number of primary vertex distribution (N_{privtx}) as weights

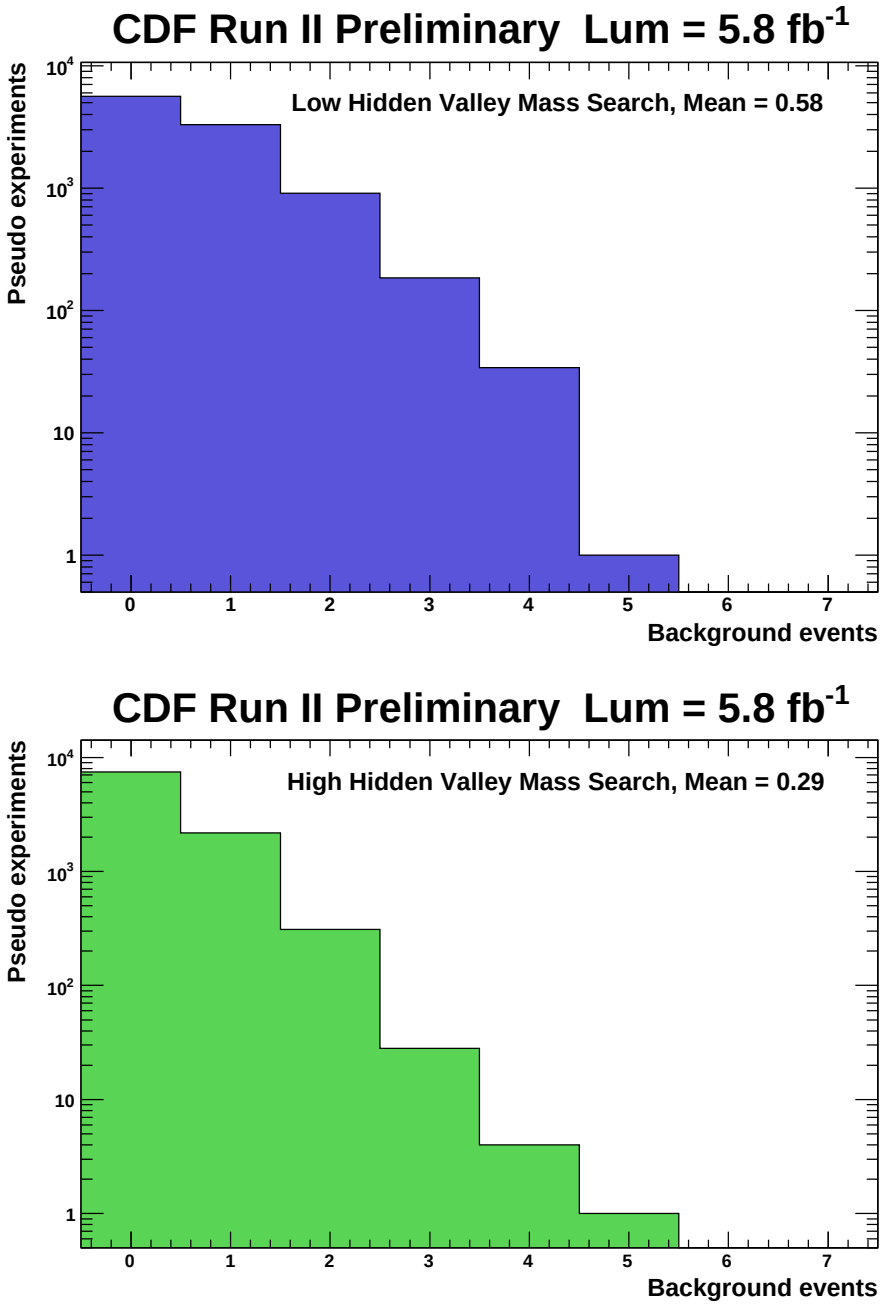

Figure 5.9: Background event distributions for low (top) and high (bottom) HV mass searches. The mean of these distributions are the background estimates.

to match the signal MC events to the ZBB trigger data. These weights were calculated separately for periods A and B. In each case, the N_{privtx} distribution of data (with signal

region cuts) was divided by the N_{privtx} distribution of the signal MC (also with signal region cuts). Then each event in the signal MC sample is weighted by this ratio.

The trigger efficiency for the ZBB trigger when applied to the signal MC sample is split into two general time periods, which are labeled Period A and B. This is shown in Fig. 5.10, where the trigger efficiency is shown as a function of run number (time). Two periods are defined separated at run 200,900. Before this run number, the efficiency is about 5%. Afterwards the efficiency drops to 1.5%. The signal MC was produced for a run range much smaller, period 0 through 9, than that of the ZBB trigger data, which encompasses data from period 0 through period 25. Because the data continues for many more runs, the percentage of events in the signal MC samples is about 37% before and 63% after run 200,900. In the ZBB trigger data, the integrated luminosity, with prescales, is 15% before and 85% after.

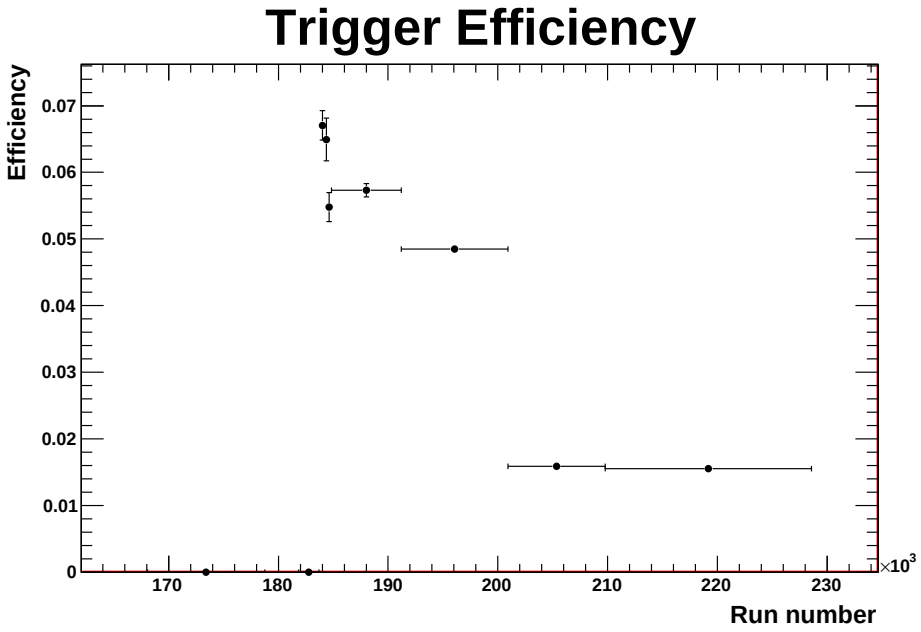

Figure 5.10: Signal MC trigger efficiency for $M_{h_0} = 130$ GeV, $M_{HV} = 20$ GeV, $c\tau_{HV} = 1.0$ cm. Period A and Period B are separated at run 200,900.

We reweight the signal MC using the following equation:

$$N_{signalMC} = Y_A \frac{\sigma L_A}{N_A} + Y_B \frac{\sigma L_B}{N_B}. \tag{5.1}$$

The variables are: Y_i-the yield or the number of signal MC events that pass all cuts in periods A and B; L_i-the luminosity of the ZBB trigger, in periods A and B; N_i-the number of signal MC generated in periods A and B; and σ-the cross section of $gg \to h_0$ production.

Finally, two scale factors have been applied to the number of signal MC events. A B-Tagging Scale Factor for the TStnSVF algorithm with $|d_0|_{max} < 1.0$ cm has been applied twice ($SF_{b-tagging} = 0.9 \times 0.9 = 0.81$), because we have two b-tagged jets. A second scale factor takes into account differences that arise in the ZBB trigger simulation used on the signal MC vs. the real ZBB trigger. Previously, a measurement of the $Z \to b\bar{b}$ cross section measured a scale factor for these differences [51]. This scale factor is $SF_{trigger} = 1.12$.

Higgs Mass (GeV)	$\sigma_{gg \to h_0}$ **(fb)**
130	858
170	349

Table 5.4: Cross section of Higgs production through gluon-gluon fusion.

Table 5.5 shows the results of our search. The number of expected signal MC events is calculated from each signal MC sample. The statistic error on this quantity is very small and not included in the table. The number of background events is calculated in from the 10,000 pseudo experiments. In both cases, the systematic uncertainties discussed next dominate the statistical uncertainties.

The number of observed events is the number of real ZBB trigger events that pass the analysis cuts. There is one event observed in the low HV mass search and one in the high HV mass search. However, we are not yet ready to make a statistically valid statement on

whether or not we observe an excess of events, as we do not have an uncertainty on the estimated number of background events. The uncertainties on the background estimate are calculated and discussed in Section 5.2.

Higgs Mass (GeV)	**HV Mass (GeV)**	**HV life-time (cm)**	**Expected Signal MC**	**Background Estimate**	**Number Observed**
low HV mass search					
130	20	1.0	0.64	0.58	1
170	20	1.0	0.074	0.58	1
high HV mass search					
130	40	1.0	0.26	0.29	1
170	40	1.0	0.38	0.29	1
170	65	1.0	0.14	0.29	1
130	40	0.3	0.24	0.29	1
130	40	2.5	0.10	0.29	1
130	40	5.0	0.043	0.29	1

Table 5.5: Results of our search. The background estimate uncertainties are discussed below.

5.2 Systematic Uncertainties

5.2.1 PDF Uncertainties

In Part 5.1 we presented the background estimate without an uncertainty. Here we discuss the many sources of uncertainty on this background estimate. To clarify some definitions, since we are performing a counting experiment, independent sources of uncertainty can be combined together in the usual way, regardless whether they are statistical uncertainties or systematic uncertainties. That is, they will contribute in the same fashion to our final result regardless of how they are classified. The uncertainties that propagate through from the p.d.f.s can be considered both types, but for the purposes of this document, these uncertainties are systematics.

In order to account for the various uncertainties that arise from the p.d.f.s we use the Bootstrap technique. CDF note 9081 [67] and Ref. [68] explain the bootstrap technique in greater detail. The purpose of the bootstrap technique is to calculate the uncertainty on a statistical quantity, e.g., the mean, due to the statistical errors present in the data sample. In the simple case of a mean, there is a closed-form analytic solution to calculating the standard deviation. However, if the uncertainty on the quantity does not have an analytic form, such as a correlation factor, or if the quantity is more complicated such as the background estimate in this analysis, the bootstrap technique can be used to calculate the uncertainty. The application of the bootstrap technique to this analysis is shown in Fig. 5.11. Here pseudo events are constructed as before, but when sampling from the p.d.f.s, we instead sample from "pseudo p.d.f.s" or what is often termed "bootstrap p.d.f.s". (Bootstrap data is the general term; here we have applied it to our p.d.f.s.) The origin of these bootstrap p.d.f.s requires an explanation of how bootstrap data is constructed.

Given a finite dataset, we can create bootstrap data by sampling with replacement

from the original data. If our original dataset has eight entries $(x_1, x_2, \ldots, x_8)$, a bootstrap sample may contain data points: $(x_7, x_7, x_5, x_7, x_2, x_2, x_1, x_2)$. For our p.d.f.s, the bootstrap p.d.f.s are created by sampling from the three dimensional histogram many times (more on this later) building a new three dimensional histogram. This bootstrap histogram does not have the exact number of entries as the original histogram. Because the number of entries is itself a statistic, we vary it with a Poisson distribution with the original number of entries as the mean. This Poisson varied number is the number of entries in the new bootstrap histogram. This procedure has the same effect of statistically varying each bin on this histogram with a Poisson distribution where the central value is the number of entries in that bin.

This histogram is then converted into a p.d.f. (actually a c.d.f.) for sampling. This sampling occurs many times for each boot-strap p.d.f., i.e., as many pseudo experiments are performed with each bootstrap p.d.f.s as with the original p.d.f.s, 10,000. The width of the distribution of background estimates from the bootstrap p.d.f.s is the uncertainty on the background estimate calculated from the original p.d.f.s.

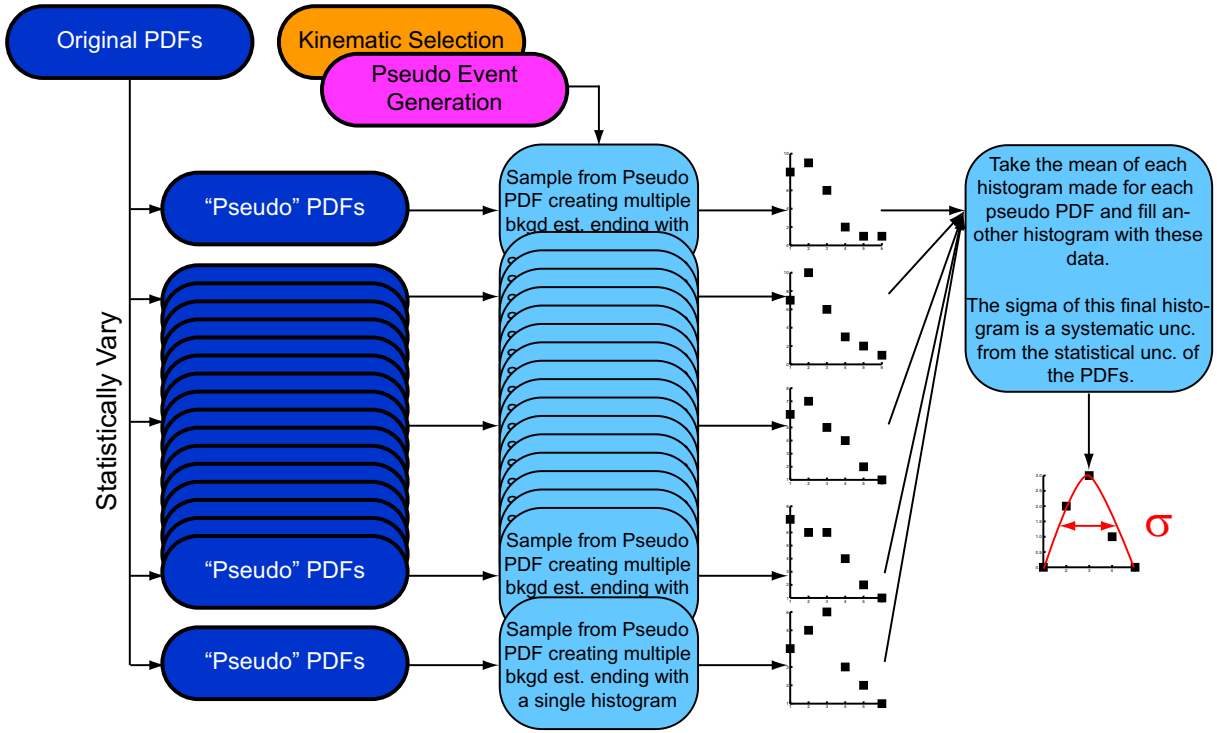

Figure 5.11: Flowchart showing the bootstrap technique used to calculate the uncertainties of the p.d.f.s.

"Many times" in this case is 200 times. 200 bootstrap p.d.f.s are constructed and thus 200 background estimates are calculated. The uncertainty on the standard deviation of a Gaussian quantity is $1/\sqrt{2N}$. With 200 bootstrap p.d.f.s the resulting uncertainty *on the uncertainty* is 5%.

The results of the bootstrap technique are shown in Fig. 5.12. The distribution shown is a distribution of background estimate, each one entry represents a different set of bootstrap p.d.f.s used to calculate that estimate. The distributions are Gaussian and the width returned by the fit is taken as the uncertainty on the background estimate. With this we take 0.023 and 0.013 as the uncertainties for the low and high HV mass search background estimates respectively.

5.2.2 Pseudo Event Uncertainties

The pseudo event generation algorithm previously described has two more effects which contribute systematic uncertainties to the background estimate. They deal with how the pseudo b tags and pseudo flavors are assigned to the pseudo dijet. The b-tag probability was derived from the number of (double) b-tagged dijets in the ZBB trigger sample. This number has a statistical uncertainty associated which we must take into account as a systematic. Since a Bayesian division algorithm was used to calculate the probability, there is an up and down uncertainty (also called error high and error low) on the central value. We regenerate two new sets of pseudo data, one with the probabilities increased by the upward uncertainty, and a second set with the probabilities decreased by the down uncertainty. The resulting number of pseudo dijets in the new samples are larger (smaller) for the up (down) uncertainty adjusted probabilities.

This differing number of pseudo dijets affects the final background estimate. After running through these new pseudo data with 10,000 pseudo experiments, we calculate an up and down b-tag probability background estimate. The percent difference between this

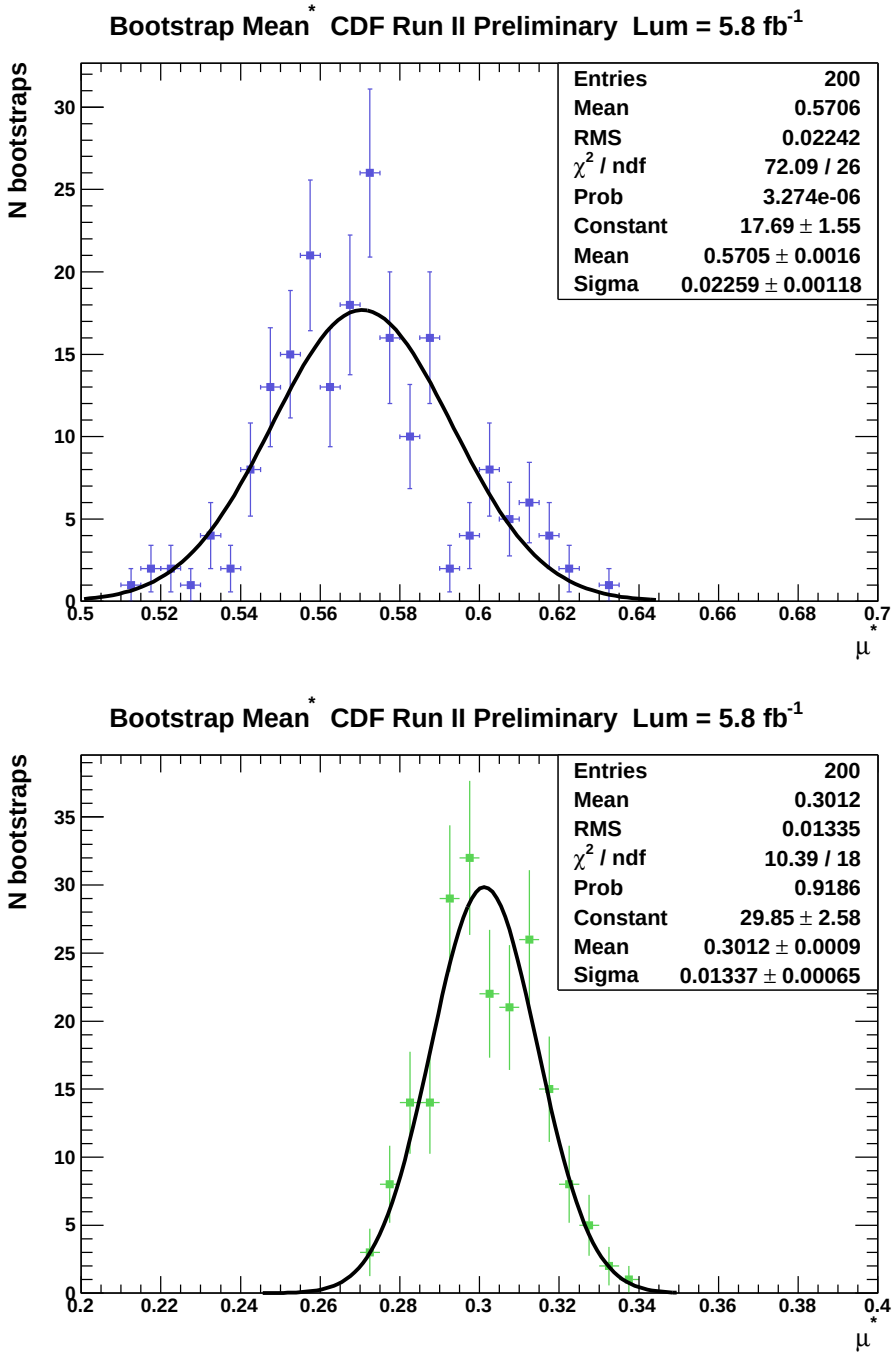

Figure 5.12: Results of the bootstrap. The distributions show the results of 200 bootstrap where each entry consists of running 10,000 pseudo experiments with a bootstrap p.d.f. sample. The widths of the distributions are the uncertainties on the background estimate.

and the original background estimate is the systematic uncertainty on the background estimate; see Table 5.6.

Search	**Background Estimate**	**b-tag Prob.**		**b-tag Prob.**	
		Down (%)	**Up (%)**	**Down (%)**	**Up (%)**
low HV mass	0.579	0.534	0.599	-7.741	3.421
high HV mass	0.291	0.303	0.313	3.92	

Table 5.6: Systematic uncertainties associated with the b-tag probability during pseudo event generation.

For the high HV mass search, the b-tag down probability result is greater than the background estimate central value. We take $\frac{1}{2}$ of the difference between the down results and the central value, and divide that by the central value, to obtain a percent difference.

The flavor composition used to assign the flavor of the dijets also results in another source of systematic uncertainties. First, there are uncertainties associated with the fit, which propagate through as systematics. As explained in Section 4.6.3 eight fractions were fit. These fractions are correlated to one another, thus in order to vary them by their statistical uncertainties, it is necessary to first decorrelate them. This is done by taking the resulting 8×8 covariance matrix from the fit and diagonalizing it. The resulting matrix of eigenvectors can be used to rotate these eight fractions into an orthonormal basis, where they are uncorrelated.

In this uncorrelated basis we adjust each fraction up and down by their respective statistical uncertainties. Then the eight fractions rotated back to their original frame where in they are converted into the nine double-flavor states that are used to assign dijets their pseudo flavor. With an up and down flavor composition calculated, we proceed to generate two sets of pseudo data, each with the same b-tagging probability as the original, but different flavor composition. We run 10,000 pseudo experiments using these pseudo data to calculate up and down flavor composition background estimates. The percent

difference between these values and the central value is the systematic uncertainty and are shown in Table 5.7.

Search	**Flavor Fit Down (%)**	**Flavor Fit Up(%)**	**MC track over-eff (%)**	**CC +10% (%)**
low HV mass	-0.34	0.017	2.75	0.43
high HV mass	0.069	0.55	8.91	0.72

Table 5.7: Systematic uncertainties associated with the flavor composition. The table shows the % differences from the central value.

Adjusting the flavor composition fits for statistical uncertainties result in a very small systematic uncertainty. We take a -0.5% systematic downward to account for the flavor composition fit in the down direction. The up direction however is overlapped by other systematics in the next paragraph.

We considered two additional systematics from the flavor composition. The MC has been shown to have an over-efficiency in reconstructing tracks. Since the tracks within a secondary vertex are used to calculate the vertex mass, which is in turn used as the MC templates for the flavor fit, the flavor composition results are affected. This tracking over-efficiency is not constant but varies with track p_T, etc. However, we take 3% as the maximal shift in the vertex mass in the MC [69] [70]. MC templates were regenerated with a -3% shift to account for this over-efficiency. The resulting MC templates have different shapes and thus the flavor composition fits have different results. The resulting fit is then used to generate another set of pseudo data to explore this systematic uncertainty. The same procedure as described before is used and the results are shown in Table 5.7. This uncertainty moves the background estimate up by a few percent, and overlaps the uncertainty due to the fit in the up direction.

Another effect with the flavor composition is that the fits in Section 4.6.3 rarely return any c-quark states, as shown in Fig. 4.30. We take a maximal variation of 10% as an

artificial charm contribution in the CC double-flavor state. Correspondingly, the BB fraction is decreased by 10%. The resulting flavor composition is used to generate a set of pseudo data, where the background estimate is calculated in the same manner as before. The percent difference is shown in Table 5.7. The artificial charm sample shows that the change to the background estimate due to an increase in c quarks is less than one percent, and is less than the MC tracking over-efficiency.

The flavor composition uncertainty is two-sided. We take the flavor composition down difference as the systematic uncertainty in the negative direction as described above. In the positive direction we use the MC tracking over-efficiency percent difference: 2.75% and 8.91% for the low and high HV mass searches respectively.

5.2.3 Signal MC Uncertainties

Systematic uncertainties on the signal MC are rate uncertainties that affect how many signal MC events pass the variable cuts. These include:

1. Jet Energy Scale
2. Trigger Simulation Systematics
3. B-tagging Scale Factor
4. Parton distribution function
5. Luminosity

The first systematic uncertainty is calculated separately for each signal MC sample, while the trigger simulation systematic, BTSF, and luminosity have the same value across all samples, and the parton distribution function is approximately the same value for all samples.

The JES uncertainty is calculated in a standard way. The scale factor on jets due to the JES is varied up (down) one sigma with respect to its central value. The result is that more (less) jets pass the $E_T > 20$ GeV cut. This effects the number of expected signal MC events for each sample; the percent differences due to the JES are shown in Table 5.8.

Higgs Mass (GeV)	**HV Mass (GeV)**	**HV life-time (cm)**	**JES Down (%)**	**JES Up (%)**
low HV mass search				
130	20	1.0	-12.97	14.32
170	20	1.0	-12.5	10.71
high HV mass search				
130	40	1.0	-15.58	16.08
170	40	1.0	-8.8	7.89
170	65	1.0	-6.33	4.0
130	40	0.3	-16.49	12.8
130	40	2.5	-14.27	21.27
130	40	5.0	-13.56	25.52

Table 5.8: JES systematic uncertainties calculated separately for different signal MC samples.

The trigger simulation systematic uncertainty is based on the trigger scale factor discussed in Section 5.1.3, and is measured at 8.9%.

The BTSF for the TStnSVF b tagger is calculated at the operating point $|d_0|_{max} < 1.0\ cm$. There is an uncertainty associated with this BTSF that propagates through as a systematic uncertainty. This is nominally 2.74% statistical and there is an additional systematic associated with BTSF. This systematic is taken from CDF Note 8640 [63]; the resulting BTSF systematic uncertainty on the expected number of signal MC is 10% because we have two b-tagged jets.

The parton distribution function uncertainty is taken from Ref. [66] which documents these uncertainties for multiple analyses, including ones that use $gg \rightarrow h_0$ production. The resulting uncertainty is 2.5%.

Finally, the luminosity contributes 6%, which derives from a 4.4% uncertainty on the detector acceptance and a 4% uncertainty on the $p\overline{p}$ inelastic cross-section [71].

5.2.4 Summary

The systematic uncertainties calculated are shown in Table 5.9. These systematic uncertainties are used in the calculation of the limits discussed in Chapter 6.

Uncertainty	**Down (%)**	**Up (%)**
Background estimate - low HV mass search		
Data statistics	±0.039	
B-tag prob. statistics	-7.74	3.42
Flavor composition	-0.5	2.75
Background estimate - high HV mass search		
Data statistics	±0.046	
B-tag prob. statistics	±3.92	
Flavor composition	-0.5	8.91
Signal MC		
Jet Energy Scale	varies; see Table 5.8	
Trigger Unc.	±8.9	
B-tagging scale factor	±10	
Parton distribution function	±2.5	
Luminosity	±6	

Table 5.9: Summary of systematic uncertainties for the background estimate and signal MC simulation. The JES is calculated separately for each signal MC sample.

CHAPTER 6

CONCLUSION

6.1 Limit Calculation

With all the uncertainties calculated, we form test hypotheses consisting of our background estimate along with our signal MC. A separate test hypothesis is constructed for each set of masses and lifetimes. We also create corresponding null hypotheses consisting only of the background estimate for each HV mass search. No statistically significant signal is seen in our search. Table 6.1 shows p-values for each set of masses, showing the probability that the null hypothesis has fluctuated to the data.

Higgs Mass (GeV)	**HV Mass (GeV)**	**HV lifetime (cm)**	**p-value**
low HV mass search			
130	20	1.0	0.44
170	20	1.0	0.43
high HV mass search			
130	40	1.0	0.27
170	40	1.0	0.26
170	65	1.0	0.26
130	40	0.3	0.27
130	40	2.5	0.27
130	40	5.0	0.27

Table 6.1: Null hypothesis p-values for this search.

Since we do not observe a statistically significant excess we proceed to set a limit on the production cross section times branching ratio of the Hidden Valley model for the particular masses and lifetimes we studied. A Bayesian limit calculator [72] is used for this calculation. Table 6.2 shows the resulting observed limit, median expected limit, along with the ± 1 and ± 2 sigma values on the expected limit, all at 95% confidence level.

Higgs Mass (GeV)	**HV Mass (GeV)**	**HV life-time (cm)**	**Obs. Limit (pb)**	**Expected Limit (pb)**				
				-2 σ	-1 σ	median	+1 σ	+2 σ
low HV mass search								
130	20	1.0	6.2	4.3	4.3	4.3	6.2	8.4
170	20	1.0	22.1	15.2	15.2	15.2	22.1	29.9
high HV mass search								
130	40	1.0	15.9	10.5	10.5	10.5	15.9	21.5
170	40	1.0	4.4	2.9	2.9	2.9	4.4	6.0
170	65	1.0	11.7	7.7	7.7	7.7	11.7	15.7
130	40	0.3	17.8	11.7	11.7	11.7	17.8	24.2
130	40	2.5	40.7	26.8	26.8	26.8	40.7	55.1
130	40	5.0	94.3	62.0	62.0	62.0	94.3	127.9

Table 6.2: Observed and Expected limits at 95% confidence level calculated for different signal MC samples.

The counting experiment was performed with a small discrete number of events, where the background estimate is less than one. Thus the expected limit can only fluctuate up (from zero). The result is that the negative sigma expected limits will be identical to the median limit.

Figures 6.1, 6.2, 6.3 and 6.4 show the results of the limit calculation. In Fig. 6.1, 6.2 and 6.3 the x-axis is the mass of the Higgs boson. Figure 6.1 is for a M_{HV} of 20 GeV corresponding to the low HV mass search. Figure 6.2 is for a M_{HV} of 40 GeV, corresponding to the high HV mass search. Figure 6.3 shows the results of the high HV mass search for a M_{HV} of 65 GeV. Figure 6.4 shows the limits for M_{h_0} of 130 GeV and M_{HV} of 40 GeV with the HV lifetime on the x-axis.

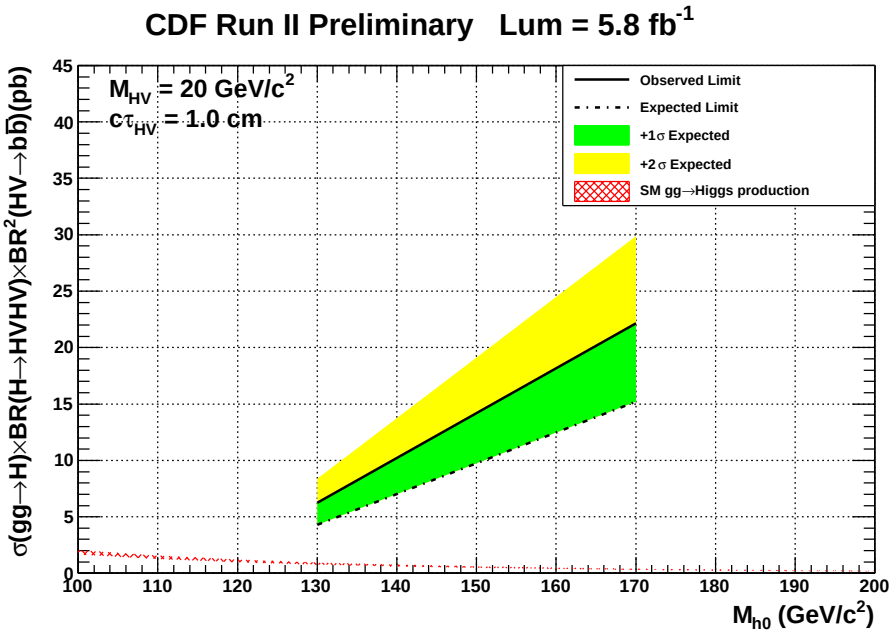

Figure 6.1: Observed and Expected limit with +1 & +2 σ bands for signal MC with HV mass 20 GeV.

We have searched for heavy metastable particles that decay into a jet pair at a displaced vertex at CDF. No statistically significant excess is observed, and limits are set on the production cross section times branching ratio for the Hidden Valley phenomenology we

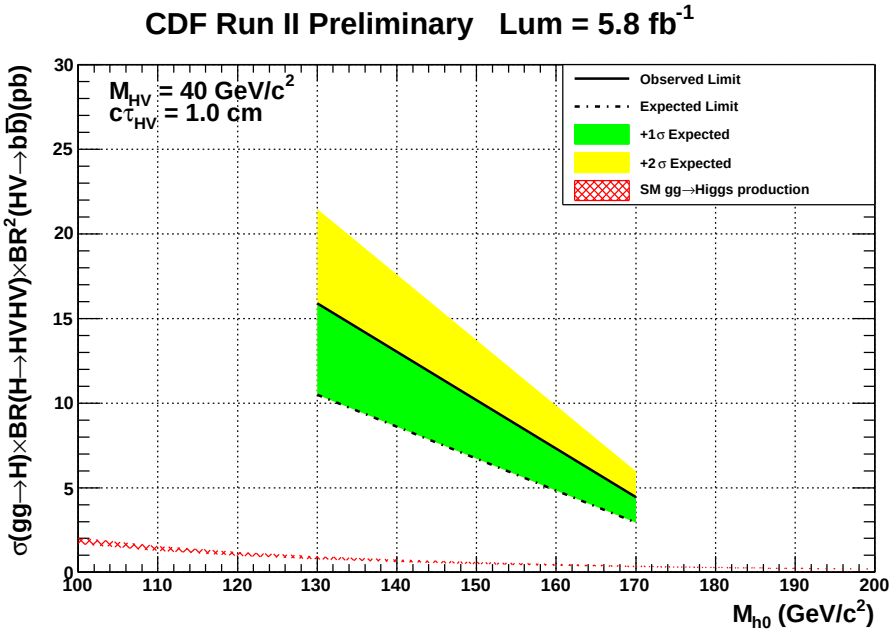

Figure 6.2: Observed and Expected limit with +1 & +2 σ bands for signal MC with HV masses 40 GeV.

have used as a benchmark. The results shown for this phenomenology can be used to constrain other models by considering the differences of the cross section, branching ratio, and the kinematics of the final state.

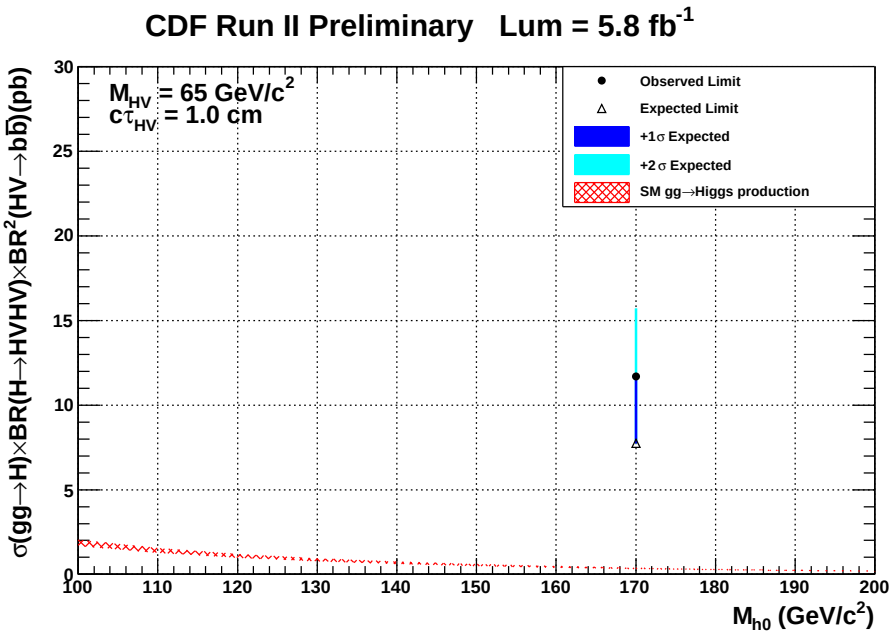

Figure 6.3: Observed and Expected limit with +1 & +2 σ bands for signal MC with HV masses 65 GeV.

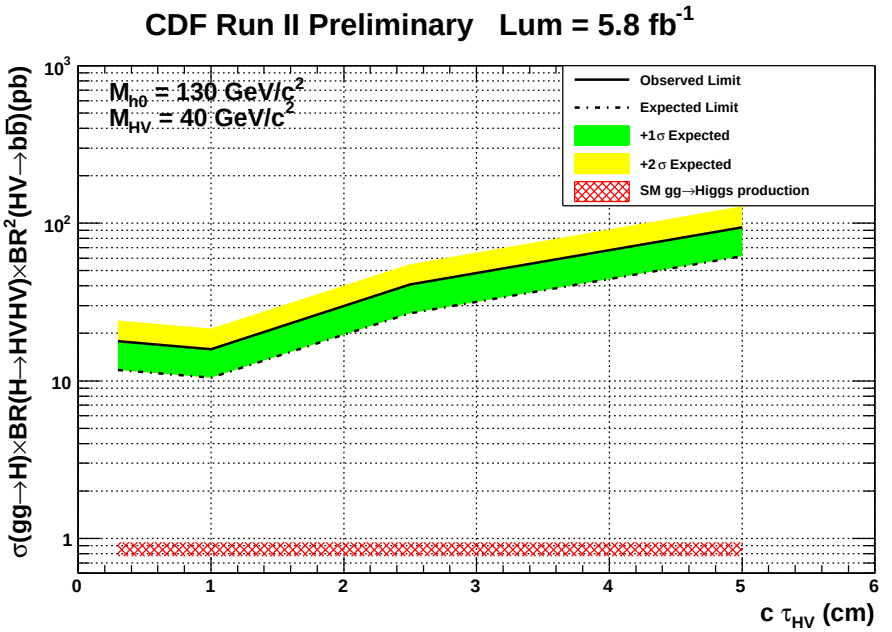

Figure 6.4: Observed and Expected limit with +1 & 2 σ bands for signal MC for differing HV particle lifetimes.

APPENDIX A

DERIVATIONS

A.1 Derivation of p.d.f. variables

Given the primary vertex $\vec{pv}$, a secondary vertex $\vec{sv}$, and a jet momentum vector $\vec{p_j}$ all in the x-y plane, we can define the vector $\vec{L_{xy}}$ and θ as follows

$$\vec{L_{xy}} = \vec{sv} - \vec{pv} \tag{A.1}$$

$$\theta = \Delta\phi(\vec{L_{xy}}, \vec{p_j}). \tag{A.2}$$

Then the definitions of u and v are

$$u = |\vec{L_{xy}}|cos(\theta) \tag{A.3}$$

$$v = |\vec{L_{xy}}|sin(\theta). \tag{A.4}$$

α is defined given the secondary vertex's momentum vector $\vec{p_{sv}}$.

$$\alpha = \Delta\phi(\vec{p_{sv}}, \vec{p_j}). \tag{A.5}$$

A.2 Derivation of ψ and ζ

A.2.1 ψ

ψ is defined as the distance of closest approach of the primary vertex to the two-dimensional line [73] defined by the secondary vertex $\vec{sv}$ and its momentum $\vec{p_{sv}}$. First

define variables $\vec{c}$ as

$$\vec{c} = p\vec{v} - s\vec{v}. \tag{A.6}$$

The vector representing the distance of closest approach is then

$$\vec{\psi} = \vec{c} - (p\hat{_{sv}}(\vec{c} \cdot p\hat{_{sv}})). \tag{A.7}$$

And the magnitude of this vector is ψ.

A.2.2 ζ

ζ is defined as the distance from the primary vertex to the intersection of the two lines [73] formed by two secondary vertices, $s\vec{v}_1$ and $s\vec{v}_2$, and their corresponding momenta, $p_{s\vec{v}1}$ and $p_{s\vec{v}2}$. First we must define the wedge ($\wedge$) operator. Given two two-dimensional vectors $\vec{u} = (u_x, u_y)$ and $\vec{v} = (v_x, v_y)$, $u \wedge v$ is

$$u \wedge v = u_x v_y - u_y v_x. \tag{A.8}$$

First define D as

$$D = p_{s\vec{v}1} \wedge p_{s\vec{v}2}. \tag{A.9}$$

If D is not zero then the lines are not parallel or coincident and we continue. Define $\vec{c}$ as

$$\vec{c} = s\vec{v}_1 - s\vec{v}_2. \tag{A.10}$$

Now the intersection ($\vec{int}$) of these two lines is calculated as follows,

$$S_I = \frac{\vec{p_{sv2}} \wedge \vec{c}}{D} \tag{A.11}$$

$$\vec{int} = \vec{sv}_1 + S_I(\vec{p_{sv1}}), \tag{A.12}$$

and ζ is simply

$$\zeta = |\vec{int} - \vec{pv}|. \tag{A.13}$$

Finally, to sign ζ, sum the momenta of the two jets where the two secondary vertices are present.Take the dot product of this sum with $\vec{\zeta}$. If the dot product is greater than one, ζ is positive, otherwise it is negative.

REFERENCES

[1] J. Dalton. "On the Absorption of Gases by Water and Other Liquids". *Memoirs of the Literary and Philosophical Society of Manchester, Second Series*, 1:271–287, 1805.

[2] R. Cahn and G. Goldhaber. *"The Experimental Foundations of Particle Physics "*. Cambrige: Cambridge University Press, 1989.

[3] J. J. Thomson. "Cathode Rays". *Philosophical Magazine*, 44:293, 1897.

[4] E. Rutherford. "The Scattering of α and β Particles by Matter and the Structure of the Atom". *Philosphical Magazine*, 21:669, 1911.

[5] N. Bohr. "On the constitution of atoms and molecules". *Philosophical Magazine*, 26:476, 1913.

[6] C. Anderson. "The Positive Electron". *Phys. Rev.*, 43(6):491–494, Mar 1933.

[7] S. Neddermeyer and C. Anderson. "Note on the Nature of Cosmic-Ray Particles". *Phys. Rev.*, 51(10):884–886, May 1937.

[8] J. Street. and E. Stevenson. "New Evidence for the Existence of a Particle of Mass Intermediate Between the Proton and Electron". *Phys. Rev.*, 52(9):1003–1004, Nov 1937.

[9] R. Shankar. *"Principles of Quantum Machnaics"*. New York : Kluwer Academic/Plenum Publishers, 1994.

[10] Y. Ashie, et al. "Measurement of atmospheric neutrino oscillation parameters by Super-Kamiokande I". *Phys. Rev. D*, 71(11):112005, Jun 2005.

[11] B. Aharmim, et al. "Electron energy spectra, fluxes, and day-night asymmetries of ^{8}B solar neutrinos from measurements with NaCl dissolved in the heavy-water detector at the Sudbury Neutrino Observatory". *Phys. Rev. C*, 72(5):055502, Nov 2005.

[12] K. Nakamura et al. "2010 Review of Particle Physics". *J. Phys.*, G37:075021, 2010.

[13] M. Peskin and D. Schroeder. *"An Introduction to Quantum Field Theory"*. Westview Press, 1995.

[14] S. Tomonaga. "On a Relativistically Invariant Formulation of the Quantum Theory of Wave Fields". *Progress of Theoretical Physics*, 1(2):27–42, 1946.

[15] J. Schwinger. "On Quantum-Electrodynamics and the Magnetic Moment of the Electron". *Phys. Rev.*, 73(4):416–417, Feb 1948.

[16] J. Schwinger. "Quantum Electrodynamics. I. A Covariant Formulation". *Phys. Rev.*, 74(10):1439–1461, Nov 1948.

[17] R. P. Feynman. "Space-Time Approach to Quantum Electrodynamics". *Phys. Rev.*, 76(6):769–789, Sep 1949.

[18] R. P. Feynman. "The Theory of Positrons". *Phys. Rev.*, 76(6):749–759, Sep 1949.

[19] R. P. Feynman. "Mathematical Formulation of the Quantum Theory of Electromagnetic Interaction". *Phys. Rev.*, 80(3):440–457, Nov 1950.

[20] S. Glashow and J. Iliopoulos, and L. Maiani. Weak Interactions with Lepton-Hadron Symmetry. *Phys. Rev. D*, 2(7):1285–1292, Oct 1970.

[21] S. Weinberg. "A Model of Leptons". *Phys. Rev. Lett.*, 19(21):1264–1266, Nov 1967.

[22] G. Arnison et. al. "Experimental observation of isolated large transverse energy electrons with associated missing energy at $\sqrt{s} = 540\ GeV$". *Physics Letters B*, 122(1):103–116, 1983.

[23] G. Arnison et. al. "Experimental observation of lepton pairs of invariant mass around 95 GeV/c2 at the CERN SPS collider". *Physics Letters B*, 126(5):398–410, 1983.

[24] P. Higgs. "Broken symmetries, massless particlees and gauge fields". *Physics Letters*, 12(2):132–133, 1964.

[25] R. K. Ellis, W. J. Stirling, and B. R. Webber. *QCD and Collider Physics*. Cambrigde: Cambrigde University Press, 1996.

[26] M. Strassler and K. Zurek. "Echoes of a hidden valley at hadron colliders". *Physics Letters B*, 651(5-6):374–379, 2007.

[27] M. Strassler and K. Zurek. "Discovering the Higgs through highly-displaced vertices". *Physics Letters B*, 661(4):263–267, 2008.

[28] M. Strassler. "Hidden Valley Benchmarks". http://www.phys.washington.edu/users/strasslr/hv/bench.

[29] D. E. Kaplan, M. A. Luty, and K. M. Zurek. "Asymmetric dark matter". *Phys. Rev. D*, 79(11):115016, Jun 2009.

[30] V. M. Abazov, et al. "Search for Resonant Pair Production of Neutral Long-Lived Particles Decaying to $b\bar{b}$ in $p\bar{p}$ Collisions at $\sqrt{s} = 1.96\ TeV$". *Phys. Rev. Lett.*, 103(7):071801, Aug 2009.

[31] R. Moore. "Accelerator 101". http://www-cdf.fnal.gov/internal/WebTalks/Archive/1005/100506_cdf_aces_%in_cloud_chamber_at_330/02_100506_cdf_aces_in_cloud_chamber_at_330_Ron_Moore_1%_ronmoore_Ace_Training_050610.ppt, May 2010.

[32] "Tevatron Run II Handbook". http://www-bd.fnal.gov/lug/runII_handbook/RunII_index.html.

[33] D. Acosta, et al. "Measurement of the J/ψ meson and b-hadron production cross sections in $p\bar{p}$ collisions at $\sqrt{s} = 1960\ GeV$". *Phys. Rev. D*, 71(3):032001, Feb 2005.

[34] D. Acosta, et al. "Measurement of the $t\bar{t}$ production cross section in $p\bar{p}$ collisions at $\sqrt{s} = 1.96\ TeV$ using lepton + jets events with secondary vertex b -tagging". *Phys. Rev. D*, 71(5):052003, Mar 2005.

[35] C. Hill, et al. "Operational experience and performance of the CDFII silicon detector". *Nucl. Instrum. Meth.*, A530:1–6, 2004.

[36] A. Sill, et al. "CDF Run II silicon tracking projects". *Nucl. Instrum. Meth.*, A447:1–8, 2000.

[37] A. Affolder, et al. "Intermediate silicon layers detector for the CDF experiment". *Nucl. Instrum. Meth.*, A453:84–88, 2000.

[38] A. Affolder, et al. "CDF central outer tracker". *Nucl. Instrum. Meth.*, A526:249–299, 2004.

[39] L. Balka, et al. "The CDF Central Electromagnetic Calorimeter". *Nucl. Instrum. Meth.*, A267:272, 1988.

[40] S. Bertolucci, et al. "The CDF Central and Endwall Hadron Calorimeter". *Nucl. Instrum. Meth.*, A267:301, 1988.

[41] M. Albrow, et al. "The CDF plug upgrade electromagnetic calorimeter: Test beam results". *Nucl. Instrum. Meth.*, A480:524–546, 2002.

[42] G. Apollinari, et al. "Shower maximum detector for the CDF plug upgrade calorimeter". *Nucl. Instrum. Meth.*, A412:515–526, 1998.

[43] G. Ascoli, et al. "CDF Central Muon Detector". *Nucl. Instrum. Meth.*, A268:33, 1988.

[44] Dorigo, T. "The muon system upgrade for the CDF II experiment". *Nucl. Instrum. Meth.*, A461:560–562, 2001.

[45] A. Artikov et al. "Design and construction of new central and forward muon counters for CDF II". *Nucl. Instrum. Meth.*, A538:358–371, 2005.

[46] D. Acosta, et al. "The performance of the CDF luminosity monitor". *Nucl. Instrum. Meth.*, A494:57–62, 2002.

[47] G. Gomez-Ceballos, et al. "Event builder and Level 3 at the CDF experiment". *Nucl. Instrum. Meth.*, A518:522–524, 2004.

[48] B. Ashmanskas, et al. "The CDF silicon vertex trigger". *Nucl. Instrum. Meth.*, A518:532–536, 2004.

[49] J. Adelman, et al. "The Silicon Vertex Trigger upgrade at CDF". *Nucl. Instrum. Meth.*, A572:361–364, 2007.

[50] J. Donini, et al. "Energy Calibration of b^- Quark Jets with $Z \to b\bar{b}$ Decays at the Tevatron Collider". *Nucl. Instrum. Meth.*, A596:354–367, 2008.

[51] J. Donini, T. Dorigo, C. Neu, M. Shochet. "Modifications to the $Z \to b\bar{b}$ Level-2 Trigger for High Luminosity Running". CDF/ANAL/TRIGGER/CDFR/7394.

[52] H. Wenzel. Tracking in the SVX. CDF/DOC/SEC_VTX/PUBLIC/1790.

[53] P. Avery. Applied Fitting Theory IV Forumlas for Track Fitting. http://www.phys.ufl.edu/~avery/fitting/fitting4.pdf.

[54] F. Abe, et al. "Topology of three-jet events in $p\bar{p}$ collisions at $\sqrt{s} = 1.8\ TeV$". *Phys. Rev. D*, 45(5):1448–1458, Mar 1992.

[55] J. P. Berge. "CTVMFT Revisited". CDF/DOC/TRACKING/PUBLIC/7537.

[56] A. Bhatti, et al. "Determination of the jet energy scale at the collider detector at Fermilab". *Nucl. Instrum. Meth.*, A566:375–412, 2006.

[57] T. Sjostrand, S. Mrenna, P. Skands. "PYTHIA 6.4 Physics and Manual". *JHEP*, 05:026, 2006.

[58] S. Kwang and M. Shochet. "TStnSVF - A Secondary Vertex Finder for Stntuple". CDF/DOC/SEC_VTX/CDFR/9689.

[59] Y. Weiming, et al. "SVX B-tag Algorithm 'Seed Vertexing' for top Search". CDF/ANAL/TOP/CDFR/2716.

[60] C. Neu, H. H. Williams, E. Thomson. "Ultratight SECVTX Tagging: Efficiency Studies". CDF/DOC/SEC_VTX/CDFR/7932.

[61] S. Budd, T. Junk, T. Liss, C. Neu. "Tight, Loose and Ultratight SECVTX Tag Rate Matrix with 1.2fb-1". CDF/DOC/SEC_VTX/GROUP/8519.

[62] J. Freeman, S. Grinstein, T. Junk, E. Palencia. "SECVTX Scale Factors and Mistag Matrices for 2.2 fb-1 of Data up to P13". CDF/DOC/SEC_VTX/CDFR/9280.

[63] F. Garberson, J. Incandela, C. Neu. "SECVTX b-Tag Efficiency Measurement Using Muon Transverse Momentum for 1.2/fb Analyses". CDF/DOC/SEC_VTX/CDFR/8640.

[64] S. Grinstein, J. Guimaraes da Costa, D. Sherman. "SECVTX Mistag Asymmetry for Winter 2007". CDF/DOC/SEC_VTX/CDFR/8626.

[65] J. Freeman, S. Grinstein. "SECVTX Mistag Asymmetry Study through Period 13". CDF/DOC/SEC_VTX/CDFR/9277.

[66] CDF and D0 Collaborations. "Combined CDF and D0 Upper Limits on Standard Model Higgs-Boson Production with up to 6.7 fb^{-1} of Data". *Preliminary Results prepared for the ICHEP 2010 Conference*, 2010.

[67] J. Adelman, E. Brubaker. "The Bootstrap Technique and its Application to Analyses in the Top Mass Group". CDF/ANAL/TOP/GROUP/9081.

[68] B. Efron and R. J. Tibshirani. *"An introduction to the bootstrap"*. New York : Chapman & Hall, 1993.

[69] S. Grinstein, D. Sherman. "SecVtx Scale Factors and Mistag Matrices for the 2007 Summer Conferences". CDF/DOC/SEC_VTX/CDFR/8910.

[70] Simon Sabik, Pierre Savard. "Track reconstruction efficiency in jets". CDF/ANAL/JET/CDFR/6894.

[71] D Acosta, et al. "First Measurements of Inclusive W and Z Cross Sections from Run II of the Fermilab Tevatron Collider". *Phys. Rev. Lett.*, 94(9):091803, Mar 2005.

[72] T. Junk. "Sensitivity, Exclusion and Discovery with Small Signals, Large Backgrounds, and Large Systematics". http://www-cdf.fnal.gov/~trj/mclimit/production/mclimit.html. CDF/DOC/STATISTICS/PUBLIC/8128.

[73] Dan Sunday. "Geometry Algorithms". http://softsurfer.com/algorithms.htm.